THÈSE

En vue de l'obtention du

DOCTORAT DE L'UNIVERSITÉ DE TOULOUSE

Délivré par : *l'Institut National Polytechnique de Toulouse (INP Toulouse)*

Présentée et soutenue le *07/12/2020* **par :**

Oumaima EL MANSOURI

Fusion of Magnetic Resonance and Ultrasound Images for Endometriosis Detection

---

JURY

Jean-Philippe Thiran	Professeur des universités	Examinateur
Mireille Garreau	Professeur des universités	Rapporteure
Philippe Ciuciu	Directeur de recherche	Rapporteur
Mario Figueiredo	Professeur des universités	Examinateur
Xavier Pennec	Directeur de recherche	Examinateur
Adrian Basarab	Maître de conférences	Directeur de thèse
Jean-Yves Tourneret	Professeur des universités	Co-directeur de thèse
Denis Kouamé	Professeur des universités	Co-directeur de thèse

---

École doctorale et spécialité :
MITT : Image, Information, Hypermédia
Unité de Recherche :
Institut de Recherche en Informatique de Toulouse (UMR 5277)
Directeur(s) de Thèse :
Adrian Basarab, *Jean-Yves Tourneret* et *Denis Kouamé*
Rapporteurs :
Mireille Garreau et *Philippe Ciuciu*

Acknowledgements

I would like firstly to express my sincere gratitude to my supervisors Professors Adrian Basarab, Denis Kouamé, and Jean-Yves Tourneret, they convincingly guided and encouraged me to be professional and do the right thing even when the road got tough. I am very grateful to all of them for their scientific advice, the insightful discussions that we had. I would like to thank you for encouraging my research and for allowing me to grow as a research scientist. I would like to thank the surgeon gynecologist Fabien Vidal from CHU Toulouse, you have been there to support this Ph.D. in many ways: your phantom enable us to validate our fusion method and your comments help us to improve the quality of the proposed method, thank you.

I also have to thank the members of my Ph.D. committee, Professors Jean-Philippe Thiran, Mireille Garreau, Philippe Ciuciu, Mario Figueiredo, and Xavier Pennec for serving as my committee members. I also want to thank you for letting my defense be an enjoyable moment, and for your brilliant comments and suggestions, thanks to you.

I thank all the former and present members of the IRIT lab especially my great office mate who has been supportive in every way (thank you Mohamad Hourani and good luck). I would like also to thank my second family in the TéSA lab. I shared unforgettable moments with you. I will cherish these memories for the rest of my life. A special thanks to Corinne Mailhes. You are the nicest person I've ever met.

A special thanks to my family. Words can not express how thankful I am to my mother, father, and brothers (Hamid, Soufyan, Oussama El Manssouri, and Saida Ech-charyfy). My parents have sacrificed their lives for me and provided unconditional care and love. I truly love them so much,

and I would not have made it this far without them. I would also like to thank my beloved husband Yacine Khoya for his support, he was by my side in bad and good moments. I love you my darling. I am also grateful to my family in law (Hammadi, Mariam, Mohamed, Ilias, Asmaa, Inasse, Wissam, and Marwa Khoya). They are my new family who supported and encouraged me during this PhD. I would also like to thank my best friends and sisters (Salma, Nadia, Sabrina [and Adem], Aicha, Maki, and Hanene). You have been great supporters during my bad and good moments.

These past three years have not been an easy ride, both personally and academically. I truly thank you all for staying by my side, even when I was irritable.

الحمد لله رب العالمين

Résumé

L'endométriose est un trouble gynécologique qui touche généralement les femmes en âge de procréer et qui est associé à des douleurs pelviennes chroniques et à l'infertilité. L'endométriose est un exemple typique de pathologie qui nécessite l'utilisation de l'imagerie à résonance magnétique (IRM) et l'imagerie ultrasonore (US) (appelée aussi échographie) pour le diagnostic préopératoire et la chirurgie guidée. Ces modalités sont utilisées conjointement car elles contiennent des informations complémentaires. Cependant, le fait qu'elles aient des résolutions, des champs de vue et des contrastes différents et qu'elles soient corrompues par des bruits de differentes natures rend la collecte d'informations à partir de ces modalités difficile pour les radiologues. Ainsi, la fusion des images IRM et l'échographie peut faciliter la tâche des experts médicaux et améliorer le diagnostic préopératoire et le plan de l'intervention chirurgicale.

L'objet de cette thèse de doctorat est de proposer une nouvelle méthode de fusion automatique des images IRM et US. Tout d'abord, nous supposons que les images IRM et US à fusionner sont alignées, c'est-à-dire qu'il n'y a pas de déformation géométrique entre elles. Nous proposons alors dans ce contexte idéal des méthodes de fusion pour ces deux images, qui visent à combiner les avantages de chaque modalité, c'est-à-dire un bon contraste et un bon rapport signal/bruit pour l'IRM et une bonne résolution spatiale pour l'échographie. L'algorithme proposé est basé sur un problème inverse, réalisant une super-résolution de l'image IRM et un débruitage de l'image US. Des fonctions polynomiales sont introduites pour modéliser les relations entre les niveaux de gris des images IRM et US. Cependant, la méthode de fusion proposée est très sensible aux erreurs de recalage. C'est pourquoi, dans un deuxième temps, nous proposons une méthode conjointe de fusion et de recalage pour ces deux modalités. La fusion d'images IRM/US proposée permet d'obtenir conjointement une super-résolution de l'image IRM et un débruitage de l'image US, et peut automatiquement prendre en compte les erreurs de recalage. Une fonction polynomiale est utilisée pour relier les images ultrasonores et IRM dans le processus de fusion, tandis qu'une mesure de similarité appropriée est introduite pour traiter le problème de recalage. Le recalage proposé est basé sur une transformation non rigide contenant un modèle élastique local de *B-spline* et une transformation affine globale. Les opérations de fusion et de recalage sont effectuées alternativement, ce qui simplifie le problème d'optimisation sous-jacent. L'intérêt de la fusion et du recalage conjoints est analysé à l'aide des images synthétiques et expérimentales.

Abstract

Endometriosis is a gynecologic disorder that typically affects women in their reproductive age and is associated with chronic pelvic pain and infertility. In the context of pre-operative diagnosis and guided surgery, endometriosis is a typical example of pathology that requires the use of both magnetic resonance (MR) and ultrasound (US) modalities. These modalities are used side by side because they contain complementary information. However, MRI and US images have different spatial resolutions, fields of view and contrasts and are corrupted by different kinds of noise, which results in important challenges related to their analysis by radiologists. The fusion of MR and US images is a way of facilitating the task of medical experts and improve the pre-operative diagnosis and the surgery mapping.

The object of this PhD thesis is to propose a new automatic fusion method for MRI and US images. First, we assume that the MR and US images to be fused are aligned, i.e., there is no geometric distortion between these images. We propose a fusion method for MR and US images, which aims at combining the advantages of each modality, i.e., good contrast and signal to noise ratio for the MR image and good spatial resolution for the US image. The proposed algorithm is based on an inverse problem, performing a super-resolution of the MR image and a denoising of the US image. A polynomial function is introduced to model the relationships between the gray levels of the MR and US images. However, the proposed fusion method is very sensitive to registration errors. Thus, in a second step, we introduce a joint fusion and registration method for MR and US images. Registration is a complicated task in practical applications. The proposed MR/US image fusion performs jointly super-resolution of the MR image and despeckling of the US image, and is able to automatically account for registration errors. A polynomial function is used to link ultrasound and MR images in the fusion process while an appropriate similarity measure is introduced to handle the registration problem. The proposed registration is based on a non-rigid transformation containing a local elastic B-spline model and a global affine transformation. The fusion and registration operations are performed alternatively simplifying the underlying optimization problem. The interest of the joint fusion and registration is analyzed using synthetic and experimental phantom images.

Acronyms

ADMM	Alternating Direction Method of Multipliers
ANN	Artificial Neural Networks
BCCB	Block Circulant matrix of Circulant Blocks
CC	Cross-Correlation
CNR	Contrast-to-Noise Ratio
CT	Computed Tomography
CVT	Curvelet Transform
DICOM	Digital Imaging and Communication in Medicine
DSC	Dice Similarity Coefficient
DWT	Discrete Wavelet Transform
EM	Expectation-maximization
EN	Entropy
FF	Fusion Factor
FSIM	Feature similarity index metric
GGD	Generalized Gaussian Distribution
HR	High Resolution

ICP	Iterative Closest Point
INPT	Institut national polytechnique de Toulouse
IRIT	Institut de Recherche en Informatique de Toulouse
ISNR	Improvement in Signal-to-Noise Ratio
i.i.d	independent and identically distributed
LC	Local Correlation
LC^2	Linear Correlation of Linear Combination
LPT	Laplacian Pyramid Transform
LR	Low Resolution
NMR	Nuclear Magnetic Resonance
MI	Mutual Information
MMSE	Minimum Mean Square Error
MRI	Magnetic Resonance Imaging
MSSIM	Mean Structural Similarity Index Measure
NMI	Normalized Mutual Information
NMSE	Normalized Mean Square Error
NRMSE	Normalized Root Mean Square Error
PALM	Proximal Alternating Linearized Minimization
PCA	Principal Component Analysis
PET	Positron Emission Tomography
PSNR	Peak Signal-to-Noise Ratio
PVA	Polyvinyl Acid
RBF	Radial Basis Functions
RF	radio-frequency

RMSE	Root Mean Square Error
SNR	Signal-to-Noise Ratio
RF	Radio-Frequency
RMSE	Root Mean Square Error
SNR	Signal-to-Noise Ratio
SPECT	Single-Photon Emission Computed Tomography
SR	Super Resolution
SSD	Sum of Squared intensity Differences
SSIM	Structural Similarity Index Measure
STD	Standard Deviation
TPS	Thin-Plate Splines
TRE	Target Registration Error
TRF	Tissue Reflectivity Function
TV	Total Variation
TRUS	Transrectal Ultrasound
TVUS	Transvaginal Ultrasound
UIQI	Universal Image Quality Indexing
US	Ultrasound

Contents

Acknowledgements **iii**

Résumé **v**

Abstract **vii**

Acronyms **ix**

Chapter 1 Introduction **1**

1.1 Medical image processing . . . 1
  1.1.1 Image formation . . . 2
  1.1.2 Image enhancement . . . 3
  1.1.3 Image analysis . . . 4
  1.1.4 Image visualization . . . 4
  1.1.5 Image management . . . 5
1.2 Endometriosis . . . 5
1.3 Endometriosis diagnosis and treatment . . . 7
  1.3.1 Laparoscopy . . . 8
  1.3.2 Imaging modalities . . . 9
1.4 Endometriosis treatment . . . 11
  1.4.1 Pain medication and hormone therapy . . . 11
  1.4.2 Conservative surgery . . . 12

1.5 Motivation and objectives 13
1.6 Organization of the manuscript 14

List of publications **17**

Chapter 2 MRI and Ultrasound imaging **19**
2.1 MR image formation 19
2.1.1 Nuclear spin and magnets 20
2.1.2 Relaxation 21
2.1.3 Spatial encoding in MR images 23
2.2 MR super-resolution 24
2.3 US image formation 25
2.3.1 US propagation 26
2.3.2 US transducer 29
2.3.3 US data 29
2.4 Speckle reduction for US imaging 31
2.4.1 Other medical imaging modalities 33
2.5 Conclusion 34

Chapter 3 Fusion and Registration in Medical Imaging **37**
3.1 Introduction 37
3.2 Medical image fusion 39
3.2.1 Multi-modal image fusion methods 41
3.2.2 Conclusion 56
3.3 Medical image registration 57
3.3.1 Image similarity measure 59
3.3.2 Transformation models 63
3.3.3 Regularization in deformable registration 67
3.3.4 Optimization 69

3.3.5 Image registration metrics . . . 70
3.4 MR and US registration: state of art . . . 71
3.4.1 Intensity-based methods . . . 72
3.4.2 Feature-based methods . . . 74
3.4.3 Other approach . . . 75
3.4.4 Conclusion . . . 75
3.5 Global Conclusions . . . 75

Chapter 4 Fusion of MRI and US images 77
4.1 Introduction . . . 77
4.2 MR/US fusion using a global polynomial function . . . 78
4.2.1 A statistical model for the fusion of MRI and US images . . . 78
4.2.2 Algorithm for MR/US fusion . . . 83
4.2.3 Simulation results . . . 89
4.3 MR/US images fusion using a patch-wise polynomial . . . 109
4.3.1 Estimation of the polynomial functions f_p . . . 109
4.3.2 Experimental results using a patch-wise polynomial function . . . 110
4.4 Conclusion . . . 114

Chapter 5 Joint registration and fusion of MRI and ultrasound images 115
5.1 Introduction . . . 115
5.2 MR/US image fusion and registration . . . 116
5.2.1 Observation models . . . 116
5.2.2 US/MR dependence model . . . 117
5.2.3 Proposed inverse problem . . . 119
5.3 Proposed registration . . . 120
5.3.1 Similarity measure . . . 120
5.3.2 Spatial transformation . . . 121
5.3.3 Regularization . . . 123

5.4 Optimization algorithm for joint fusion and registration . . . 123
  5.4.1 Estimation of the fused image for known (T_c) . . . 124
  5.4.2 Estimation of the spatial transformation . . . 126
  5.4.3 Estimation of the polynomial function . . . 127
  5.4.4 Proposed algorithm . . . 127
  5.4.5 Performance measures . . . 127
  5.4.6 Simulation results on synthetic data . . . 129
  5.4.7 Experimental results on phantom data . . . 131
  5.4.8 Hyperparameters . . . 137
5.5 Conclusions . . . 137

Chapter 6 Conclusions and perspectives 141

Conclusions and perspectives 141
6.1 Conclusions . . . 141
6.2 Future work . . . 142
  6.2.1 Short-term perspectives . . . 142
  6.2.2 Long-term perspectives . . . 143

Appendices 145
Appendix A Design of a pelvic phantom for MR/US fusion . . . 147
A.1 Phantom design . . . 147
A.2 Imaging techniques . . . 148
A.3 Imaging results . . . 149

Bibliography 187

Chapter 1

Introduction

Contents

1.1 Medical image processing . . . 1
  1.1.1 Image formation . . . 2
  1.1.2 Image enhancement . . . 3
  1.1.3 Image analysis . . . 4
  1.1.4 Image visualization . . . 4
  1.1.5 Image management . . . 5
1.2 Endometriosis . . . 5
1.3 Endometriosis diagnosis and treatment . . . 7
  1.3.1 Laparoscopy . . . 8
  1.3.2 Imaging modalities . . . 9
1.4 Endometriosis treatment . . . 11
  1.4.1 Pain medication and hormone therapy . . . 11
  1.4.2 Conservative surgery . . . 12
1.5 Motivation and objectives . . . 13
1.6 Organization of the manuscript . . . 14

1.1 Medical image processing

Medical imaging consists in producing accurate images of interior tissues for scientific and medical treatment. It includes functional and radiological modalities based on magnetic, sonography, thermal and electromagnetic imaging [Sue17]. Since 1895 and after the discovery of X-rays, medical imaging has become very crucial in the health care domain. With the increasing use of digital imaging systems for medical diagnosis, computer science, in particular medical image processing and analysis become more and more important in this domain. The idea is to support radiologists and surgeons in the interpretation of these images and to help diagnosis or therapy. Studies related to medical image processing reveal that these methods can not only improve the accuracy of the radiologist diagnosis but also help to overcome the increasing data volume that challenges radiologist time. Also, the decisions of radiologists can be affected by many factors like fatigue, distraction and experience which is not the case of machines. There are several areas in which image processing techniques are used to identify abnormalities or tumors in brain, heart, chest, lung, breast, prostate, colon, skeletal, liver or vascular system [Ban08].

In the early 1980s, large-scale research on computer-aided diagnosis (CAD) started to take place in the health care field [Doi07]. In 1982, M. Ishida [IKDF82] investigated the development of a new digital radiographic image processing system. In 1985, M. L. Giger [GD85] examined the basic imaging properties in digital radiography such as the effect of pixel size on signal to noise ratio (SNR) and threshold contrast. In 1986, K. R.Hoffmann [HDC+86] proposed an automated tracking of the vascular tree in digital subtraction angiography images using a double-square-box region-of-search algorithm. In addition to these pioneer works, several studies have been conducted in order to help radiologist in various clinical applications [IFDL83, IDLL84, GD84, LDM85, FDG85, GDF86]. The concept of CAD was established in the 1960s [LHS+63, MNJB+64] but it was not effective until the 1980s due to the fact that computers were not sufficiently powerful.

Generally, medical image processing obtained from different imaging systems involves five principle areas [Des09] (Fig. 1.2), depicted in the next subsections.

1.1.1 Image formation

The first step in the image formation is the acquisition, which consists in capturing physical details about internal aspects of the body. There are different principles of acquisition for multiple physical quantities: the photon energy for PET (positron emission tomography), the acoustic echoes in the US images, the radio-frequency signal emitted by excited atoms for MR image (magnetic resonance imaging) and the energy of incident photons for CT (computed tomography). All these modalities require subsequent steps for image formation like the conversion into an electrical signal, the preconditioning of this signal and finally its digitization.

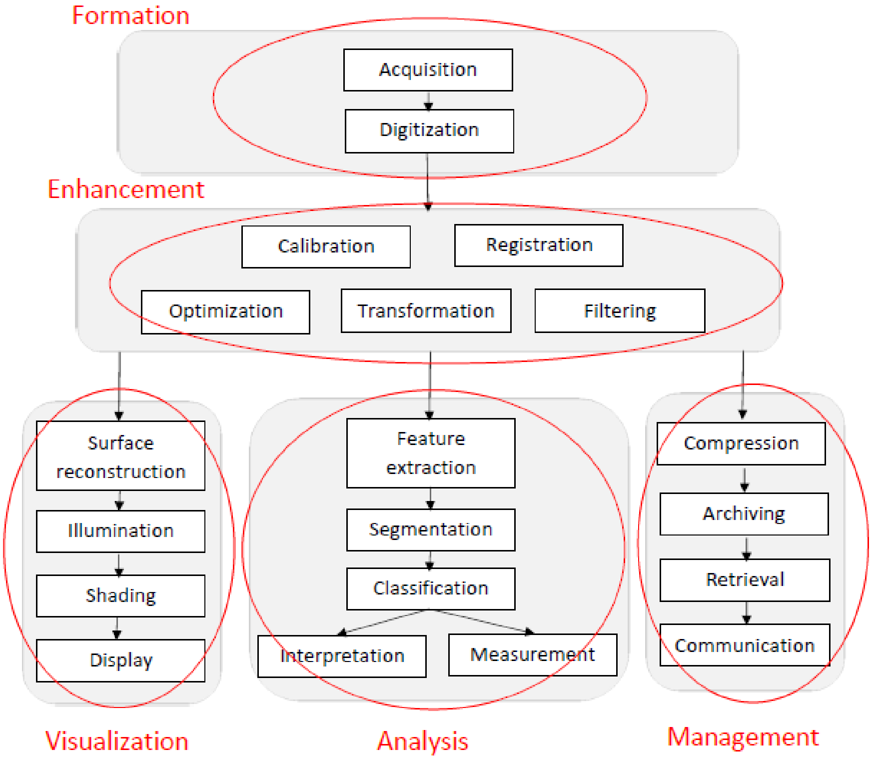

Figure 1.1: Medical image processing. Globally, image processing involves five major steps: image formation, image enhancement, visualization, image analysis and management [Des09].

1.1.2 Image enhancement

The aim of medical image enhancement is to improve the interpretability of the information contained in the image by applying an appropriate transformation to the image. Classical transformations are defined in the spatial or frequency domains [MA10].

In the spatial domain, transforms are applied directly on image pixels, which is often used for contrast optimization [KK16]. These methods generally rely on histogram [ATL14], logarithmic [HAY10] and power law transforms [SS10]. In the frequency domain, standard methods capture the spectral information contained in the image [YSS10], through filters [MM08], which can be used to smooth or sharpen the images. These techniques allow for noise, artifacts and blur reduction, enhancement of edges, contrast optimization and improvement of other fundamental properties that are important for an accurate interpretation.

1.1.3 Image analysis

Image analysis is an important step in image processing [DA00], it has several objectives such as: image segmentation, image registration and image fusion.

Image segmentation is considered as an important step in CAD since it helps radiologists to extract regions of interest (ROI) based on automatic or semi-automatic methods. It is the process of dividing an image into homogeneous parts using specific attributes. Generally, the purpose of segmentation is border detection, tumor detection and mass detection [PXP00].

Image fusion refers to assembling all the important information from multiple images and including them in fewer images, e.g., in a single image. The purpose of image fusion is to reduce the number of images and to build an enhanced image that is informative [JD14a], comprehensible and accurate for the operator. The fusion of medical images is used for several studies of pathologies and generally grants better medical decisions in clinical studies. Medical images that can be fused efficiently include MR and single-photon emission computed tomography (SPECT) images [PHS+96], MR and computed tomography (CT) [WB08], or positron emission tomography (PET) and CT [VOB+04].

Image registration creates a common geometric reference frame across two or more image datasets [OT14a]. It is a required task for the fusion and the comparison between images obtained at different times or using different imaging modalities.

1.1.4 Image visualization

Image visualization refers to all types of matrix manipulations, resulting in an optimized output of the image. Many applications require visualization and analysis of three-dimensional (3D) objects. The aim of image visualization is to gain insight into the collected data through the process of transforming, mapping, and view the collected data as images with high quality. This technology provides crucial devices for diagnosis, research and instruction where the human body is interactively explored. In order to visualize volumes, it is important not only to collect different viewpoints but also to respect subtle variations in density and opacity while displaying them. Extensive researches are done in this field especially in 3D reconstruction [NTCO12].

1.1.5 Image management

Image management deals with all the tools that provide practiced storage (servers, clouds), communication, sharing, archiving, backup, and access to image data [RP04]. Medical images use DICOM (Digital Imaging and Communication in Medicine) for storage, which may require several megabytes of storage capacity, and compression techniques. Also, techniques used in telemedicine/telehealth are part of image management [TKO96, MLM+01].

1.2 Endometriosis

Endometriosis is a disorder in which cells similar to those that form the lining of the endometrium, the layer of tissue that normally covers the inside of the uterus, grows in sites different from the uterine cavity [Giu10]. Most often, this misplaced tissue often attaches itself to the ovaries, fallopian tubes, and tissues around the uterus and ovaries. Thus, in rare cases, it can spread to other internal organs as well (Fig. 1.2 shows the most common location of the endometriosis). Endometriosis is a very common pathology since one woman out of ten gets affected by endometriosis during its reproductive years (ages between 15 and 49 years), which means that more than 176 million women in the world have been subject to endometriosis [VSB+20].

There are various symptoms of endometriosis: pelvic pain and infertility are the most common symptoms. More than half of women with endometriosis have chronic pelvic pain, especially during menstruation (dysmenorrhea) [Ton02]. These pains are usually accompanied by lower back and abdominal pain. Pain during and following sexual intercourse (dyspareunia) is also common [DM07]. Regarding infertility, one third of women with infertility problems have endometriosis and among women with endometriosis 40% are infertile [BCBB10]. There are other less common symptoms like urinary or bowel symptoms, ovary cancer, diarrhea, chronic fatigue etc [FBF+11]. About 25% of women have no symptom and 85% of women with infertility have no pain. Therefore, the severity

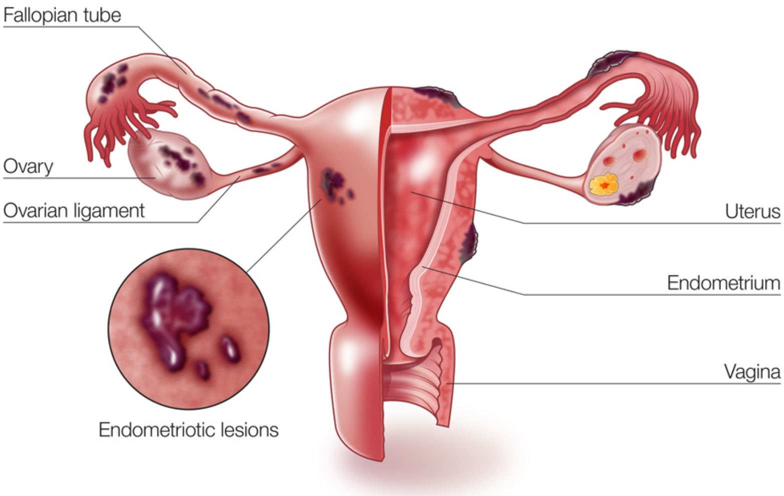

Figure 1.2: The important location of the endometrial tissue.

of the pain does not indicate the stage of the disease. Minimal, mild, moderate, and severe are the four stages of the endometriosis. Several factors such as location, size, and depth of organ infiltration help to determine the stage of the disorder [PFF+95]. Endometriosis can also affect these women psychologically or socially: it may cause depression, anxiety, hopelessness since living and struggling with agonizing pain without knowing the reason can be more stressful than a chronic known medical condition. 73% of women with endometriosis have had their relationships affected by endometriosis and 82% of women are unable to carry out day-to-day activities due to endometriosis [SdA09].

Each month during the menstrual cycle, endometrial tissue located outside the uterus named implants, grow and bleed in response to hormones as for the tissue lining inside the uterus, resulting in internal bleeding and inflammation. The body responds to inflammation and injuries by forming scar tissue and adhesions as a part of the healing process. Adhesions (see Fig. 1.3) can cause tough complications: it can attach for example the ovaries or cutting off the blood supply. These adhesions explain the higher risk of infertility because it makes it difficult for an egg to travel to or to implant the uterus [KOM+08].

The exact cause of endometriosis is not clear. There are many theories that have never been

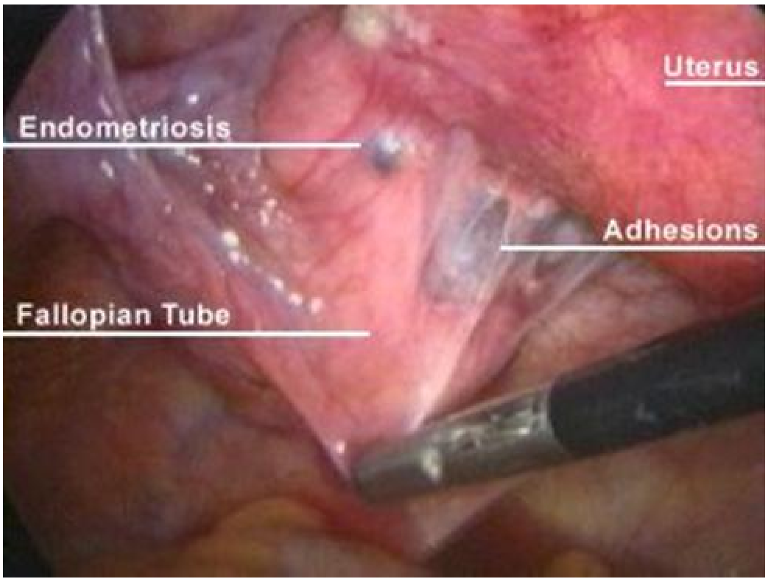

Figure 1.3: An example of the endometriosis adhesions that attach the fallopian tube to the uterus [Anu20].

scientifically proved [VOCD01]: in 1924, Sampson proposed that endometriosis is due to retrograde menstruation where the menstrual blood that normally exits the body through the vagina circulates to the pelvic by the fallopian tube [Fal56]. Another hypothesis is that hormones alter the cells outside the uterus and transform them into endometrial tissues. All experts seem to agree that there are some common risk factors like having a family history of the condition [MM93], menstrual cycle disorder like very short periods or very long cycles or menstruation starting at an early age [DVB$^+$93]. Also, women who have no children have a higher risk of developing the disease.

1.3 Endometriosis diagnosis and treatment

Unfortunately, the diagnosis of endometriosis is still a difficult task. In the UK, statistics show that there is an average of 7.5 years between the woman first sees a doctor for symptoms and endometriosis diagnosis [APABP03], which gives the endometrium tissue time to spread, impact several organs and worsen the patient health.

Typically, the health history and the presence of many symptoms can lead the gynecologist to suspect endometriosis. Doctors generally start with a pelvic physical examination by feeling and palpating the pelvis for abnormalities like cysts [BLR+09]. However, this technique is unable to detect small areas with endometriosis and implants that are note located in the cervix, the vagina, and the vulva.

Visual examination using laparoscopy [JRH+13] and different medical image modalities such as transvaginal ultrasound (TVUS) [SBHU91] and magnetic resonance imaging (MRI) [ZDFZB03] are the standard for the diagnosis of endometriosis. There is no consensus on the use of CT scanning images due to a lack of contrast resolution [WJLS98].

Since there is no effective treatment, hormonal medication is used to decrease the pain in periods and intercourse. However, depending on the disease stage, laparoscopic surgery reveals to be the unique effective pain-relief [JDB+10]. TVUS and magnetic resonance (MR) images, besides being used for diagnosis, are used to identify endometriosis and its depth of infiltration in organs before performing surgery.

1.3.1 Laparoscopy

Laparoscopy (minimally invasive surgery) is an operation procedure performed in the pelvis and the abdomen using tiny cuts (0.5cm-1cm) and a camera to look inside the abdominal cavity. Laparoscopy is the most common way to officially diagnose endometriosis. A careful investigation of the pelvic during laparoscopy permits lesion visualization. Sometimes a biopsy can be taken to confirm the diagnosis. During a laparoscopy, various procedures can be performed in order to destroy or remove the endometriosis cysts (Fig. 1.4), and release scar tissue. However, in the case of deep infiltrating endometriosis [DAC+14], the accuracy of laparoscopy is limited. Indeed, laparoscopy does not allow surgeons to detect the implants under complex adhesions or inside the organs. Thus, important information for surgery as deep of infiltration, lesion contours, and the exact location of endometriosis is not detected using laparoscopy only. Therefore, imaging techniques such as MR and TVUS images are crucial for the assessment of endometriosis and for creating a preoperative map for surgery.

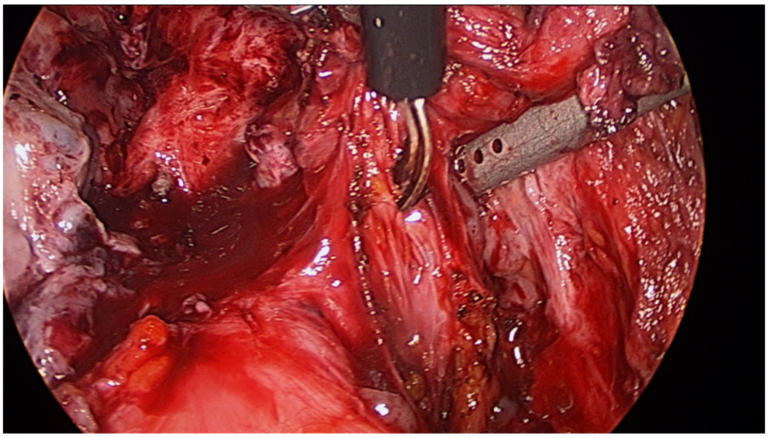

Figure 1.4: Inspecting the pelvic cavity for severe endometriosis location and excision [Gyn15].

1.3.2 Imaging modalities

Diagnosing endometriosis requires a reliable diagnostic imaging exam. Additionally, preoperative images such as MR and TVUS images are crucial for identifying the different locations of deep endometriosis because in certain sites, such as the intestine or bladder, the surgery is particularly difficult and carries greater risk.

1.3.2.1 Transvaginal ultrasound (TVUS)

Transvaginal ultrasound or endovaginal ultrasound, is an internal examination of the reproductive female organs as the uterus, fallopian tubes, ovaries and cervix by introducing gently a high-frequency transducer probe (10MHz) into the vagina, and exploring the pelvic cavity.

Vaginal ultrasound has clinical value in the diagnosis of the endometrioma (endometriosis cysts) and before operating for deep endometriosis. This concerns the identification of the spread of disease in women with well-established clinical suspicion of endometriosis. Vaginal ultrasound is inexpensive, easily accessible, has no counter-argument, and requires no preparation. Experts conducting ultrasound examinations need to be experienced. The sonographer can evaluate and look for deep infiltrating endometriosis adhesions (Fig. 1.5) and implants noting the size, location, and if applicable, the distance from the anus [HET+11]. TVUS images have also some limitations which are the huge amount of speckle reducing the signal to noise ratio, and also their limited field of view and low contrast. An improvement in sonographic detection of deep infiltrating endometriosis would not only reduce the number of diagnostic laparoscopies, but it will also guide management and enhance the quality of life.

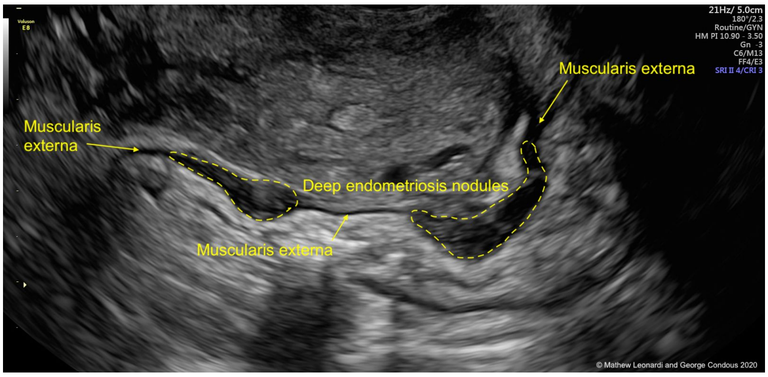

Figure 1.5: Example of 2D TVUS image that illustrates a deep infiltrating endometriosis [LC20].

1.3.2.2 Magnetic resonance imaging (MRI)

MR imaging is a non-invasive imaging technology that produces three-dimensional detailed anatomical images. It has an excellent tissue identification through several parameter sequences and contrary to TVUS, it is not operator dependent. The broad field of view allows MR imaging to exhibit the whole pelvis, which can facilitate the evaluation and the detection of lesions. MR images provide a high contrast resolution helping to assess a precise map of endometrial implants. However, MR image is not widely used due to its cost, limited availability, and low spatial resolution especially at the millimetric scale. Thus, small lesions are often not visible by MR image because they are tiny and flat, and therefore undetectable [KFBC06]. More precisely, only the lesions exceeding 5mm or appearing as hemorrhagic cysts, showing high signal intensity on T1 and low signal intensity on T2-weigthed images, can be detected (as shown in Fig. 1.6).

To conclude, MR and ultrasound images are highly useful in many diagnoses and guided surgery, both helping to assess the condition of organs. However, these two distinct imaging modalities differ by the technologies behind them and offer several advantages and limitations. In order to combine

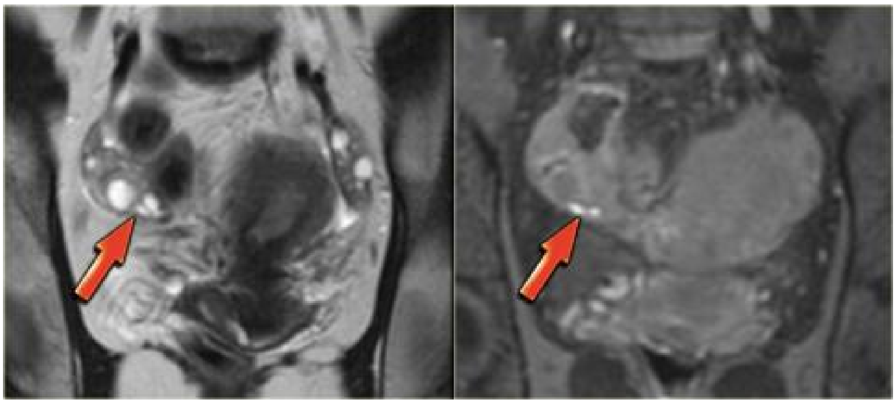

Figure 1.6: Coronal T2 and T1-Fatsat images: superficial serosal implants of endometriosis [vWHB11].

their complementary properties, MR and US images are classically used side by side for endometriosis analysis and medical intervention [CGM+04].

1.4 Endometriosis treatment

While there is no effective cure for endometriosis, there are two types of intervention to manage the symptoms related to endometriosis especially infertility and menstrual pain. The treatment depends on how severe the symptoms are and whether the patient hopes to get pregnant. Doctors generally recommend conservative treatment such as pain medication or hormone therapy and opt for surgery if the initial approach fails [VS03].

1.4.1 Pain medication and hormone therapy

There are many medications that doctors recommend to their patients as an over-the-counter pain reliever. These medications include nonsteroidal anti-inflammatory drugs [AHPG09] or endorphins to provide appropriate menstrual pain control. Endometriosis becomes inactive and gradually disappears during menopause. Thus, producing the same conditions using hormone therapy can be accurate for women who do not want to get pregnant [AKHAFH09]. The rise and the fall of hormones during the menstrual cycle cause the bleeding and the thickness of the endometrial implants.

Stabilizing hormones may stop or slow its growth and prevent new adhesions. Combined estrogen-progestogen birth control (hormonal contraception) is a gold standard hormone therapy [VPDG+05] because it can be used during long periods, is inexpensive, and easy to use. Other hormonal medications can be used as danazol [HCM+88] and gestrinone [DNPCR90] but their use is limited because of their side effect: excessive hair growth, voice changes and masculinization, etc. Generally, hormone therapy is combined with pain medication for a conservative treatment. However, these approaches are not a permanent fix or a cure for endometriosis since patients can experience pain recurrence after stopping treatment and they are not adapted for women who want to get pregnant.

1.4.2 Conservative surgery

After an accurate diagnosis that indicates the existence of endometriosis, the exact location of implants, their size, and their depth of infiltration, a surgical plan is defined to remove or incise this endometrial tissue. This procedure is usually done using laparoscopy surgery because it is considered as minimally invasive [DAC+14, NCG86]: the surgeon inserts a laparoscope with an attached camera (a viewing instrument) through a small incision and inserts through another incisions surgical instruments for the ablation or the excision of the implants, the adhesions, the endometriomas in order to restore the pelvic anatomy as normal as possible. The precision of this surgery depends on the accuracy of the diagnosis which is difficult using the current imaging techniques. Thus, 21.5% of patients at 2 years and $40-50\%$ at 5 years experience endometriosis recurrence [Guo09], which is due to part of implants that have not been removed during surgery because of their deep infiltration or defective surgical planning. Laparoscopy helps to preserve ovaries and the uterus (which is important for women who want to get pregnant) and reduces the probability of developing adhesions. However, laparoscopy increases the risk of recurrence.

In many cases, hysterectomy (removal of the uterus) is considered as a cure of endometriosis for women who do not want to conceive. However, it must be accompanied by endometriosis excision or the pain will persist if the endometriosis is located in other sites [NHG+95].

1.5 Motivation and objectives

As explained previously, endometriosis is a typical example of pathology that requires the use of MR and US modalities in conventional clinical practice. Endometriotic lesions can be either superficial or deeply infiltrating. Surgery is a cornerstone for endometriosis since disease removal positively impacts quality of life and fertility [RCLB+18]. First line radiological assessment uses MR and pelvic US imaging. MR image displays a higher sensitivity for endometriosis diagnosis compared to pelvic US (0.94 versus 0.79) [NBF+16]. In contrast, pelvic US with transvaginal or transrectal route provides a better specificity (0.94 versus 0.77) and is more accurate in the evaluation of infiltration depth when compared to MR images. Considering the benignant nature of the disease and its high recurrence rate, conservative management treatment involving limited invasive measurements is preferable to surgery whenever feasible [DR17]. In the setting of deep infiltrating endometriosis, fusing the two imaging techniques thus appears particularly promising. Indeed, the presence of information coming from both US and MR modalities in a single image is expected to improve preoperative disease mapping and subsequent definition of surgical modalities.

The fusion of MR and ultrasound (US) images is a challenging task because the two imaging modalities have different resolutions and contrasts and are corrupted by different kinds of noise. To the best of our knowledge, the fusion of MR and US images for endometriosis diagnosis has rarely been considered in the literature. The primary goal of this work is to propose a fusion method that considers MR and US image limitations and enhances image quality while gathering the information from both of them. The US image can also show some deformations under certain conditions. Introducing the transvaginal probe inside the vagina, full bladder, bowel, or gas inside the rectum can deform the pelvic organs. Moreover, since the fusion method is very sensitive to the misalignment between these two images, a joint registration and fusion method for MR and US images is interesting, which is the second objective of this PhD thesis.

1.6 Organization of the manuscript

The remaining of this thesis consists of 4 chapters and 2 appendices that are described below.

- **Chapter 2:** This chapter reminds the basic principles related to MR and US image formation. Moreover, MR and US advantages and limitations are reported and some post-processing techniques are introduced with a brief state-of-art on MR super-resolution and US despeckling techniques.

- **Chapter 3:** Since there is no existing method to fuse MR and US images, this chapter gives a general review of medical image fusion, summarizing the most known and used medical image fusion methods, which are classified into pixel-level image fusion and transform-based image fusion. This chapter also introduces some metrics for performance evaluation that will be used to evaluate the quality of image fusion. The chapter continues by introducing the image registration framework and its components with a general survey in medical image registration. The chapter is concluded by a state-of-the-art on the registration of MR and US images.

Main Contributions

The main contributions of this thesis are as follows.

- **Chapter 4:** This chapter introduces a new fusion method for magnetic resonance (MR) and ultrasound (US) images [MBV$^+$19, EMVB$^+$20], which aims at combining the advantages of each modality, i.e., good contrast and signal to noise ratio for the MR image and good spatial resolution for the US image. The proposed algorithm is based on an inverse problem, performing a super-resolution of the MR image and a denoising of the US image. A polynomial function is introduced to model the relationships between the gray levels of the MR and US images. The resulting inverse problem is solved using a proximal alternating linearized minimization algorithm. The accuracy and the interest of the fusion algorithm are shown quantitatively and qualitatively via evaluations on synthetic and experimental phantom data.

- **Chapter 5:** This chapter introduces a joint fusion and registration method for magnetic resonance images (MR) and ultrasound (US) images. Fusion allows complementary information from these two modalities to be captured, i.e., the good spatial resolution of US images and the good signal to noise ratio of MR images. However, a good image fusion method requires images to be registered, which is generally a complicated task in practical applications. The proposed approach is based on two inverse problems, performing a super-resolution of the MR image and a despeckling of the US image, and accounting for registration errors. A polynomial function is used to link US and MR images in the fusion process while an appropriate similarity measure is introduced to handle the registration problem. This measure is based on a non-rigid transformation containing a local term based on B-splines and a global term based on an affine transformation. The fusion and registration operations are performed alternatively simplifying the underlying optimization problem. The interest of the joint fusion and registration is analyzed quantitatively and qualitatively via synthetic and experimental phantom data.

Appendices

- **Appendix A:** This appendix presents an unexpensive and easy to make multi-modality phantom for MR/US image fusion validated by Dr. Vidal. This phantom shows very similar characteristics to an uterus infiltrated by endometrial tissue.

List of publications

International Journal papers

1. O. El Mansouri, F. Vidal, A. Basarab, P. Payoux, D. Kouame and J.-Y. Tourneret, **Fusion of Magnetic Resonance and Ultrasound Images for Endometriosis Detection**, *IEEE Trans. Image Process.*, 5324-5335, 2020, vol. 29, p. 5324-5335.

Conference papers with proceedings

1. O. El Mansouri, A. Basarab, M. A. T. Figueiredo, D. Kouame and J.-Y. Tourneret, **Ultrasound and magnetic resonance image fusion using a patch-wise polynomial model**, in *Proc. IEEE Int. Conf. Image Processing (ICIP)*, Abu Dhabi, United Arab Emirates, Oct. 2020.

2. O. El Mansouri, F. Vidal, A. Basarab, D. Kouame and J.-Y. Tourneret, **Magnetic Resonance and Ultrasound Image Fusion Using a PALM Algorithm**, in Proc. *Workshop on signal processing with Adaptative Sparse Structured Representations (SPARS)*, Toulouse, France, jul. 2019.

3. O. El Mansouri, F. Vidal, A. Basarab, D. Kouame and J.-Y. Tourneret, **Fusion of Magnetic Resonance and Ultrasound Images: A preliminary study towards endometriosis detection**, in *Proc. IEEE Int. Conf. Symposium on Biomedical Imaging: From Nano to Macro (ISBI)*, Venice, Italy, Apr. 2018.

Conference papers without proceedings

1. O. El Mansouri, F. Vidal, A. Basarab, D. Kouame and J.-Y. Tourneret, **Joint Fusion and Registration of Magnetic Resonance and Ultrasound Images**, *IEEE Int. Ultrason. Symp.*, Las Vegas, USA, jul. 2019.
2. O. El Mansouri, F. Vidal, A. Basarab, D. Kouame and J.-Y. Tourneret, **Fusion of Magnetic Resonance and Ultrasound Images for Endometriosis Detection**, *IEEE Int. Ultrason. Symp.*, Glasgow, Scotland, UK, sept. 2019.

Chapter 2

MRI and Ultrasound imaging

Contents

2.1 MR image formation . . . 19
- 2.1.1 Nuclear spin and magnets . . . 20
- 2.1.2 Relaxation . . . 21
- 2.1.3 Spatial encoding in MR images . . . 23

2.2 MR super-resolution . . . 24

2.3 US image formation . . . 25
- 2.3.1 US propagation . . . 26
- 2.3.2 US transducer . . . 29
- 2.3.3 US data . . . 29

2.4 Speckle reduction for US imaging . . . 31
- 2.4.1 Other medical imaging modalities . . . 33

2.5 Conclusion . . . 34

2.1 MR image formation

MR image is a medical imaging technique used in diagnosis of several pathologies related to blood vessels, heart, brain or spinal cord. The principle of MR is based on the nuclear magnetic resonance (NMR) phenomenon, i.e., the coupling between the magnetic moment of the nucleus of atoms (protons) and the external magnetic field [MS18], described by Felix Bloch and Edward Mills Purcell in 1946,which made them obtain the Nobel prize in 1952. At the beginning of the 1970s, numerous developments in NMR, particularly in spectroscopy, suggested new applications for this technique. In this context, Raymond Vahan Damadian proposed in 1969 to use NMR for medical purposes and supported his proposal with the demonstration that NMR spectroscopy allows the detection of tumors [KD15].

Figure 2.1: MR machine.

NMR is based on the spin magnetic moment caused by the nuclei of atomic isotopes such as hydrogen (H); Hydrogen is found in large quantities in the human body via the water (H_2O) contained by the tissues and the organic molecules.

2.1.1 Nuclear spin and magnets

All nucleons (neutrons and protons) have the quantum property of spin quantified by the spin angular momentum $\vec{\boldsymbol{S}}$. The spin depends on the number of neutrons and protons in the atom (in the case of hydrogen, there is only one proton, thus the spin of this proton is the spin of the atom). A non-null spin $\vec{\boldsymbol{S}}$ is associated with a magnetic moment $\vec{\boldsymbol{\mu}}$ via the relation

$$\vec{\boldsymbol{\mu}} = \gamma \vec{\boldsymbol{S}} \tag{2.1}$$

where γ is the gyromagnetic ratio.

The hydrogen has two independent spin states: spin-up and spin-down. In the absence of magnetic field, the numbers of nucleons in these two states are the same since these states are degenerated. In this case, no magnetic moment can be detected. For the construction of MRI images, the atoms are placed in a large constant magnetic field (0.5 - 4.5T) created by a superconducting magnet (see Fig. 2.1) and denoted as B_0. The interaction between the nuclear magnetic dipole moment and the external magnetic field results in Larmor precession, a rotation of the nucleons on themselves around their axis with a rapid precession movement around the axis of the magnetic field. The angular frequency of this rotation can be writing as follows:

$$\omega_0 = \gamma B_0. \tag{2.2}$$

When exposed to magnetic fields, the magnetic dipole moments of protons can either align with the direction of the external magnetic field B_0 (the low energy state) or align with the opposite direction of B_0 (high-energy state). The magnetic field M_0 produced by the entire volume is non-null and represents a longitudinal magnetization aligned with the external magnetization because the slight majority of protons align in the same direction as B_0 (this mechanism is described in Fig. 2.2) as predicted by Boltzmann theory. Note that the Larmor precession of a proton creates a magnetic moment that has a non-zero component in the z direction and in the xy plane but considering the volume, no magnetization is detected in the xy plane as the protons precess out of phase.

The M_0 magnetization created by protons cannot form the MR image as B_0 masks it. Indeed, it is impossible to detect the magnetization M_0 and produce the MR image as B_0 is very large and masks easily M_0. The solution is to flip the magnetization M_0 from the z-axis to the xy-plane, which can be done by a precise excitation with radio-frequency pulses via an external coil. Note that this excitation brings also protons into phase [MS18].

2.1.2 Relaxation

The following description occurs in a the classical xyz coordinates. After an excitation via RF pulses, the longitudinal moment M_0 flips to a certain angle and thus leads to both a moment M_z in the z -axis and a a transverse moment M_{xy} in the xy-plane. When the RF pulse is turned down, the protons relax and begin to lose their energy and return to their states M_0 before excitation (z-direction). This phenomena is called relaxation. The main mechanisms of relaxation are T1 recovery and T2 decay [WMB+11]:

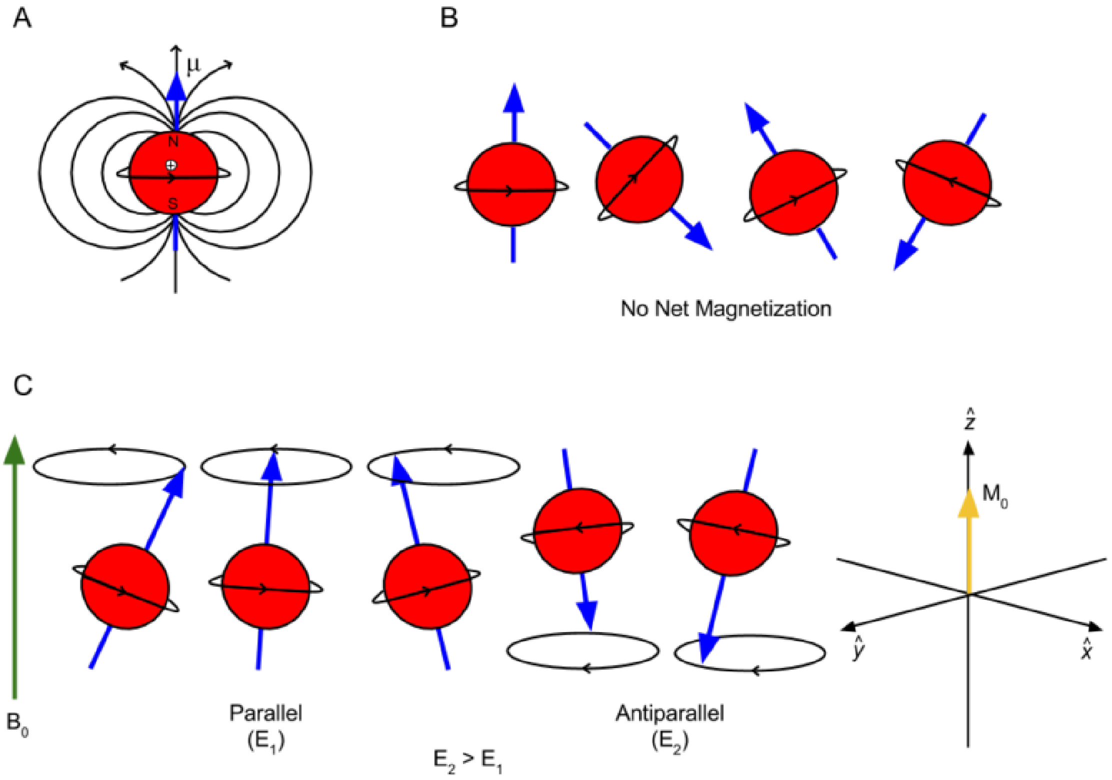

Figure 2.2: (A) the spin moment of a proton $\vec{\mu}$, (B) The spin moments of protons $\vec{\mu}$ are randomly oriented, thus, the global moment is null, (C) when placed in external magnetic field, protons align their spin in the direction or in the opposite of B_0 and then, produced a global longitudinal moment align with B_0 [BB11].

Longitudinal relaxation T1: also called spin-lattice relaxation, occurs when the protons dissipate their energy to return to their equilibrium. The longer the duration the higher M_z is. This phenomenon therefore follows an exponential dynamic [BB11] defined as

$$M_z(t) = M_0(1 - e^{-\frac{t}{T1}}). \tag{2.3}$$

$T1$ recovery is the recovery of the longitudinal moment along z. The value of T_1 ranges from $200 - 3000$ms and M_z recovers 63% of its maximal value M_0 after time T1.

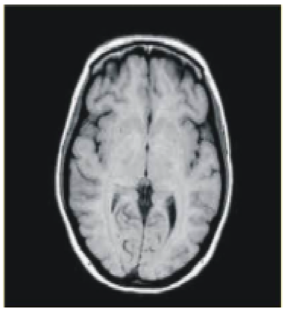

Transverse Relaxation T2: also called spin-spin relaxation is due to the agitation of molecules which causes the decay of the transverse magnetization in the xy-plane. T2 is the necessary time to reduce the transverse moment by 37%. T2 relaxation also follows an exponential dynamic defined as [BB11]:

$$M_{xy} = M_0 e^{-\frac{t}{T2}}. \tag{2.4}$$

A tissue in the body can be categorized by different times T1 and T2, which depend on the hydrogen concentration in this tissue. Thus, multiple images can be produced based on these relaxation delays such as T1 and T2-weighted MR images.

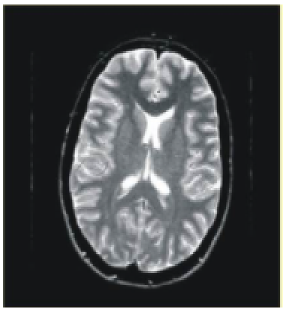

Proton density PD: weighted image produces contrast due to a long repetition time TR and a short echo time TE. It is the tissue with higher density of protons who produces the strongest signal and appear the brightest on the image.

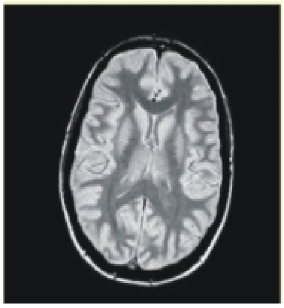

2.1.3 Spatial encoding in MR images

For imaging, it is important to allocate a position to the received signals. In the case of MR images, the majority of images are created using the two-dimensional Fourier transform (2DFT) method with slice selection [Pip95]. The MR imaging is based on a formalism named k-space. It is a matrix where MR signals are stored during the acquisition.

Slice selection is the first step of MR spatial encoding. The desired slice is selected by applying a perpendicular gradient magnetic field (slice selection gradient GSS). GSS modified the precession frequency of the protons such that an RF wave with the same frequency will cause them to shift, therefore, create an RF signal received from the desired slice. Phase encoding is the second step in the MR spatial encoding. It consists on applying phase encoding gradients to dephase the RF signal in the vertical direction. The final step is frequency encoding which consists on applying frequency encoding gradient to modify the Larmor frequencies in the horizontal direction. All these signals are recorded in k-space then processed to form an image of the slice plane.

2.2 MR super-resolution

Nowadays, MR images can provide sub-centimeter resolution. Sometimes, especially for early diagnosis, lesions can be very tiny and require a millimetric scale resolution. Thus, they are subtle or undetected in MR images. Therefore, improving imaging resolution can improve the accuracy of diagnosis.

Several methods can be used to enhance the MR spatial resolution. For example, hardware solutions consisting in increasing the external magnetic field B_0, or the number of coil receivers have been largely explored in the literature [VRTTP12]. However, this approach can be rapidly expensive. Another approach is a basic interpolation based on zero-padding which is used in most MR machines to increase the size of MR images, or in other words to decrease the pixel size. This method yields better visual results but also generates artifacts and blur to the images without introducing new information [VRTTP12]. Thus, SR algorithms for MR images are widely used in many studies.

The first application of SR to MR images has been introduced in [TH80], which has been followed by numerous studies in this domain. The purpose of image super-resolution is to estimate a high-resolution HR image from a low-resolution LR image. There are three principal approaches dedicated to SR [Zha16]:

1. Interpolation-based approaches: they are generally intuitive and consider SR as a nonuniform interpolation problem [ZYL12]. Many algorithms are used in this context such as nearest neighbor interpolation [MK14] or adaptive interpolation [DEDV19]. These methods have the advantage of being simple and easy to implement but they generally smooth high frequency details in MR images.

2. Learning-based approaches [CFK+18, CXZ+18]: they learn the relation between LR and HR images using trained databases. The results of these methods can be very accurate if the model

is well-trained.

3. Reconstruction-based approaches [Zha16, GEW10, GPOK02]: they use a data fidelity term and a prior knowledge to model a relationship between the HR and LR images. The observed LR image denoted as $\boldsymbol{y}_{\text{mr}}$ can be modeled as a decimated and blurred version of the HR image $\boldsymbol{x}_{\text{mr}}$ contaminated by an additive Gaussian noise $\boldsymbol{n}_{\text{mr}}$:

$$\boldsymbol{y}_{\text{mr}} = \boldsymbol{S}\boldsymbol{C}\boldsymbol{x}_{\text{mr}} + \boldsymbol{n}_{\text{mr}}. \tag{2.5}$$

Recovering the high-resolution MR image from its low-resolution counterpart is an ill-posed problem. In order to obtain a realistic solution, many regularization ϕ can be added (i.e., gradient [Zha16] and self-similarity [MCB$^+$10a] to name a few). The inverse problem considered for these approaches can be defined as

$$\min_{\boldsymbol{x}_{\text{mr}}} \frac{1}{2}\|\boldsymbol{y}_{\text{mr}} - \boldsymbol{S}\boldsymbol{C}\boldsymbol{x}_{\text{mr}}\|_2^2 + \tau_1 \phi(\boldsymbol{x}_{\text{mr}}) \tag{2.6}$$

where ϕ is the regularization function.

There are many algorithms that have been proposed to optimize this kind of functions, for example: gradient-based methods, soft thresholding algorithms, alternating direction method of multipliers (ADMM) and the split Bregman (SB) methods.

This thesis will consider a reconstruction-based approach applied to a single image to enhance the MR image during the fusion because of its adaptability with the proposed fusion model.

2.3 US image formation

A sound wave is a vibration that propagates by longitudinal motion as an acoustic wave. Its propagation is caused by the variation of pressure (repeating oscillation between high and low pressure) in a medium such as liquids or gas. The wavelength λ can be described as the distance over which the wave shape repeats, i.e.,

$$\lambda = \frac{c}{f} \tag{2.7}$$

where f is the wave frequency and c is the speed of sound. Note that c depends on the medium through which the sound wave propagates and can be defined as

$$c = \frac{1}{\sqrt{\rho\kappa}} \tag{2.8}$$

where ρ and κ are the density and the compressibility of the medium. Thus, the speed of sound is higher in materials where the density and the compressibility is lower. Here are some examples of propagation velocities: air (330 m/s), fat (1450 m/s), water (1480 m/s), liver (1550 m/s), kidney (1560 m/s), blood (1570 m/s), muscle (1580 m/s) and bone (4080 m/s). An average value in human tissues is $c = 1540$ m/s. Another more precise way to characterize the medium through which the US wave propagates is to study the acoustic impedance Z defined as

$$Z = \rho c. \tag{2.9}$$

US imaging is a high-frequency sound wave-based modality. The used frequencies are higher than the audible sound > 20000 Hz and range, in standard applications, from 0 to 50 MHz for most of medical applications. US imaging helps radiologists to see through the body by detecting the reflected echos of the emitted pulses using a US probe (as shown in Fig. 2.3).

US images are used in different fields: some examples of clinical applications that involve US images include cardiology, obstetrics, emergency medicine, colorectal surgery and pelvic surgery.

2.3.1 US propagation

The US image is formed by transmitting pulses into the body and detecting the reflected echoes. Other phenomena can occur during the US propagation such as scattering, refraction or attenuation (shown by Fig. 2.4), which can contaminate the image by heavy speckle noise and artifacts. The information that US images contain is due to the reflection and scattering of the emitted waves.

- **Reflection**: when the US wave passes between two mediums with different acoustic impedances Z, a fraction of the wave is reflected which helps the image formation and highlights the organ boundaries. The amplitude of the reflected wave depends on the difference between the acoustic

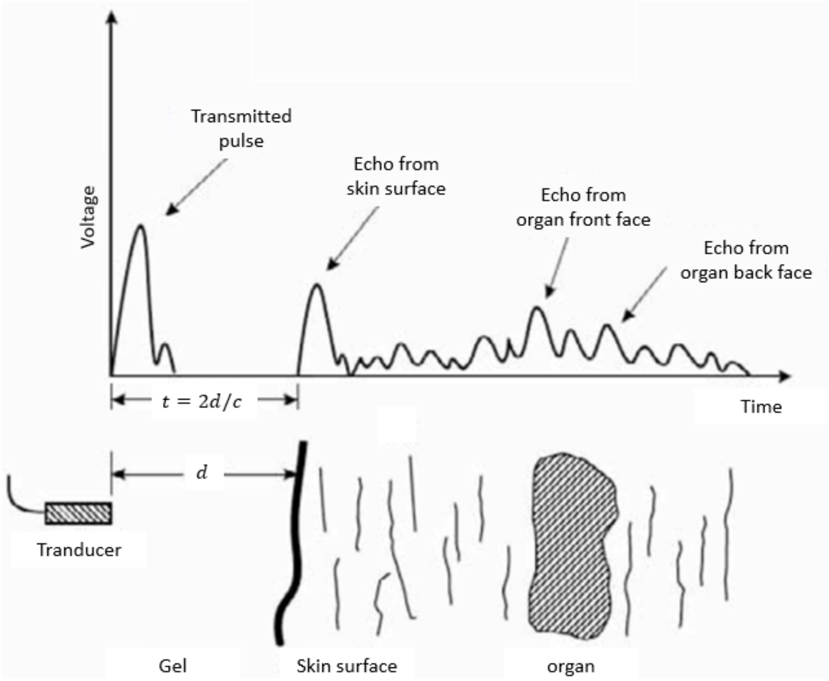

Figure 2.3: Scheme of US wave propagation for US image formation [PL06].

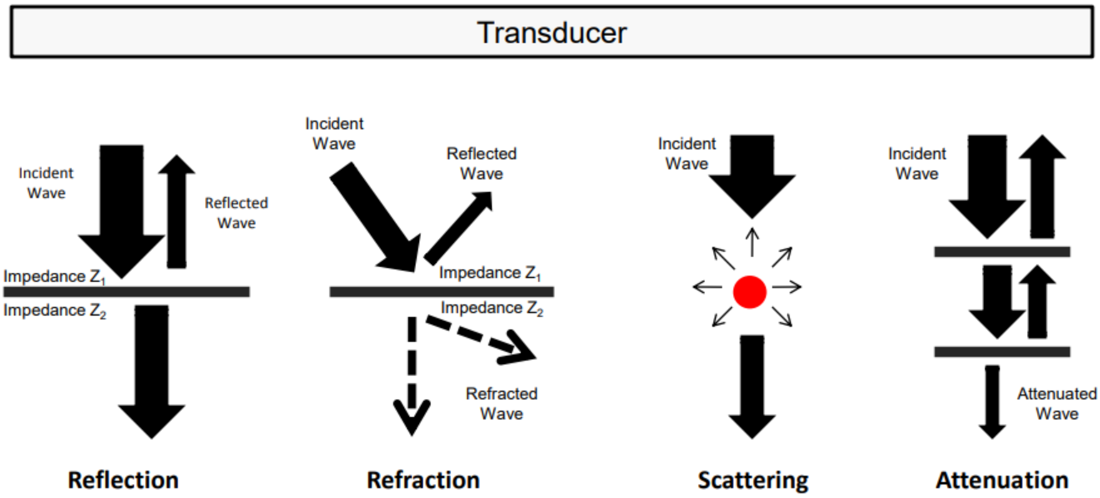

Figure 2.4: Different physical phenomena that occur during US propagation [PL06].

impedance between the two mediums. More precisely, the amplitude reflection R can be written as follows:

$$R = \frac{Z_2 \cos\theta_i - Z_1 cos\theta_r}{Z_2 \cos\theta_i + Z_1 cos\theta_r} \tag{2.10}$$

where Z_1 and Z_2 are the acoustic impedances of the two mediums. The amplitude transmission coefficient T is given by

$$T = \frac{2Z_1 cos\theta_t}{Z_2 \cos\theta_i + Z_1 cos\theta_t} \tag{2.11}$$

where θ_i, θ_r and θ_t are illustrated in Fig. 2.5.

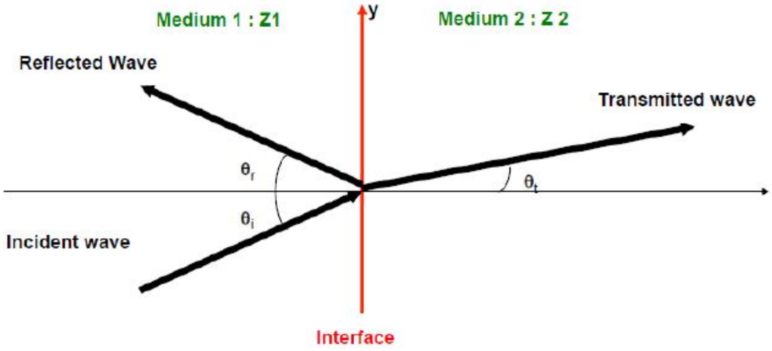

Figure 2.5: Illustration of Descartes law for the optical geometry [Che16].

- **Scattering** is a special case of case of reflection which occurs when the size of the target (to be imaged) is by far smaller than the incident wavelength. In this case, the incident wave is 'reflected' (not in a single direction as in the case of reflection but) in all the directions of the space. These targets are known as the scatterers such as red blood cells or the elementary cells inside the tissues or organs. The scattered waves can also interact with each other causing constructive and destructive interferences. This phenomenon is the principal cause of the speckle noise in US images. The power of the scattered wave I_s satisfies the following relation

$$I_s \propto \frac{d^6 c^4}{\lambda^4} I_i \tag{2.12}$$

where I_i is the incident wave power, d is the dimension of the diffuse reflector and λ is the wavelength of the emitted pulse.

- **Attenuation** is the lost of energy of the wave during propagation which is caused by two main factors: the US wave frequency and the medium crossed by the wave. For a fixed propagation distance, this phenomenon affects to a greater degree high frequencies compared to lower frequencies. Thus, for deeper areas of interest, lower frequency $3 - 5$MHz transducers are used at the expense of spatial resolution.

2.3.2 US transducer

US transducers or probes generate and sense the ultrasound energy through conversion between electrical and mechanical energies. The ultrasound probe is composed of several quartz crystals (piezoelectric crystals). These crystals vibrate when an electric current is applied and create sound waves that travel through the tissues. Conversely, they emit an electrical signal when sound waves hit them.

2.3.3 US data

2.3.3.1 Beamforming

Beamforming refers to the multiple techniques used to combine the signals received from elements of an US array. The main objective is to obtain the most intense beam with the lowest sidelobes and to be able to explore the medium in depth without important loss of information. In the transmission phase, the elements of the transducer (actually the ultrasound sensor) are acted together with previously delayed waves in order to get a summed beam at a focalization point. In the reception phase, the reflected echos are delayed and averaged to create the radio-frequency (RF) signal. The reader can refer to, for instance, [Dia13] for more information about beamforming techniques in US imaging.

2.3.3.2 RF and IQ signals

The RF signal contains information on the tissues which reflected or backscattered the ultrasound wave and is directly obtained after beamforming. Generally, an IQ-demodulation is applied on the RF signals in order to reduce the amount of data without losing information. IQ demodulation consists of 3 main steps: downmixing, low-pass filtering and decimation. Finally, the IQ signal denoted as r_{IQ} (phase and quadrature signal) can be computed as follows [Zha16]:

$$r_{\mathrm{IQ}} = (r_{\mathrm{RF}} - i\mathcal{H}(r_{\mathrm{RF}}))e^{-i\omega_0 t}, \tag{2.13}$$

where r_{RF} is the RF signal, $\mathcal{H}$ is the Hilbert transform and ω_0 is the central frequency of the US probe and $i^2 = -1$.

2.3.3.3 US image modes

There are 4 modes that are classically used in US imaging:

A-mode: it is the simplest and the oldest mode providing one-dimensional lines with echoes depending on the depth, as illustrated in the right figure. It is obtained by simply computing the envelop of the RF signal r_{RF}.

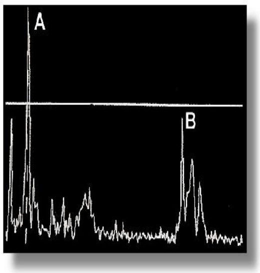

B-mode: it is a two dimensional image that displays the envelopes of the received RF signals after a logarithmic compression operation defined as

$$\boldsymbol{y}_{\mathrm{us}} = b\log(\boldsymbol{r}_{\mathrm{IQ}}) + g, \tag{2.14}$$

where b and g are linear gain constants and $\boldsymbol{y}_{\mathrm{us}}$ is the B-mode US image. Note that the rest of this work will concentrate on the B-mode US image, which will be referred to as US image.

M-mode: it is the motion mode defined as a rapid sequence of B-mode scans associated with the movement of structures versus time.

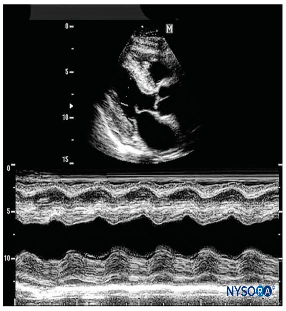

Doppler mode: it uses the Doppler effect for measuring and visualizing whether structures are moving away or towards from the probe.

There are many images that can be formed using the US waves. For more details about US formation and data, one can refer to the book [Sza04].

2.4 Speckle reduction for US imaging

US imaging is characterized by its granular texture called speckle, which indirectly carries information but which greatly affects the contrast and delineation of objects of interest such as organs or cysts. Speckle occurs in areas of high concentration of very small scatterers. The received signal at the transducer level is a combination of constructive and destructive interferences, which is the origin of this mottled texture made of bright and dark areas.

The spatial distribution of the speckle in US images is directly related to the position of the scatterers and the characteristics of the probe and can be used for motion estimation or tissue characterization [Mor13]. In general, speckle makes visual observation difficult and corrupts the diagnosis ability of the US image [Wag83]. In 1978, Burckhardt in [Bur78] described how speckle can limit the contrast resolution in US images making the low-contrast lesions disappear. Since then, many studies have considered speckle as a noise to be eliminated or attenuated using post-processing techniques without affecting the image quality. The speckle is thus a random process. Due to high number of scatterers in the acquisition volume, the Rf signal from the scatterers is assumed to have a Gaussian distribution (Law of large numbers). Thus, the pdf of the envelop (image en mode B), is assumed to have a Rayeigh pdf or a Rice pdf , if there exists a coherence component (deterministic). US despeckling can be classified into four approaches:

1. Single scale filters: they are widely used in US despeckling and can be divided into spatial filters (i.e., Gaussian averaging, Lee filter, diffusion filter and median filters [JS18]) and frequency filters (low-pass and Butterworth filters [TGAH10]). However, these methods suffer generally from loss of important information and can over-smooth the image.

2. Multi-scale enhancement [ABT01]: these methods use transforms based on wavelets [KKJ+10], shearlets [AL19] or on the Laplacian pyramid [ZYKK07] to obtain a multi resolution hierarchical representation of the image and then apply a threshold for denoising.

3. Soft computing methods like artificial neural networks (ANN) [KS20] and fuzzy logic [BS16].

4. Bayesian estimation methods: they consist in introducing a statistical model for speckle the speckle and optimizing a cost function related to the posterior distribution of the image. The cost function is generally a compromise between a data fidelity term that relates the noisy US image to the noiseless image and a regularization term related to an appropriate prior distribution for the image. The problem can be formulated using the envelop of RF signals [GSA16, MT06],

   $$\boldsymbol{r}_{\text{IQ}} = \boldsymbol{a}_{\text{us}} \boldsymbol{s}_{\text{us}} \tag{2.15}$$

   where $\boldsymbol{r}_{\text{IQ}}$ is the vectorized RF envelop, $\boldsymbol{s}_{\text{us}}$ is the noiseless envelop and $\boldsymbol{a}_{\text{us}}$ is the Rayleigh multiplicative noise. B-mode images can be obtained by log-compressing the envelop (as seen in Section 2.3), where b and g are linear gain constants. The resulting observation model can be written as:

   $$\boldsymbol{y}_{\text{us}} = \boldsymbol{x}_{\text{us}} + \boldsymbol{n}_{\text{us}} \tag{2.16}$$

where $\boldsymbol{y}_{\text{us}}$ is the observed B-mode image, $\boldsymbol{x}_{\text{us}}$ is the noiseless B-mode image and $\boldsymbol{n}_{\text{us}}$ is an additive noise, generally assumed to be independent from $\boldsymbol{x}_{\text{us}}$ and distributed according to a log-Rayleigh distribution.

2.4.1 Other medical imaging modalities

There are several types of medical images that are available for diagnosis and surgery treatment and that are generally fused. Some examples include magnetic resonance imaging (MR), computerized tomography (CT), positron emission tomography (PET), single-photon emission computed tomography (SPECT) and US (US) imaging.

CT scan: it is an X-ray imaging technique used for the diagnosis of several pathologies. CT is usually used for broken bones, tumors, heart diagnosis, blood vessels, and blood clots. CT scan give salient information about structures based on their ability to absorb the X-ray beam. However, the radiation used in CT can damage the body and cause cancer which explains why it is not used for the whole body contrary to MR images [QLD+90].

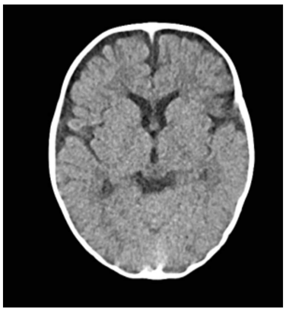

PET scan: it is a type of medical imaging that uses radioactive substances to measure and visualize metabolic processes in different parts of the body. It provides salient information when it is used to detect or measure changes in physiological activities like blood flow, regional chemical composition, metabolism, and absorption. PET helps doctors to see how well the treatment is working after diagnosis. However, it does involve exposure to ionizing radiation, and has an important operating cost [LMW+07].

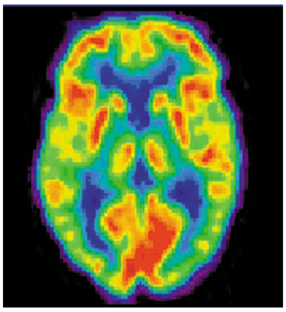

SPECT scan: it is a nuclear medicine tomographic imaging technique using gamma rays. SPECT can be used for several applications such as tumor imaging, infection imaging (leukocyte), bone scintigraphy, or thyroid imaging. SPECT allows an accurate 3D localization. Thus , it can be used to provide information about the localized function in internal organs, such as functional cardiac or brain imaging. SPECT is cheaper than high-resolution PET scan. SPECT and CT scans are usually used side by side because of their complementary information [Sch05].

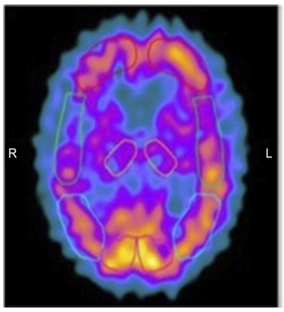

2.5 Conclusion

This chapter introduced some background on MR and US imaging, including the physics behind the formation of MR and US images. One can note that both modalities have limitations such as the bad spatial resolution (at a millimetric scale) of MR images and the low-contrast caused by speckle for US images (Table 2.1 presents a detailed comparison between MR and US images). Therefore, MR and US images are two different modalities that have different advantages and limitations. Fusing these two kinds of images can ease the task of radiologists and provide a more comprehensive visualization.

	MR	US
Expense	Very expensive	Cheap
Scan time	Long	Short
Availability	Available in specialized unit	Widely available
Contrast agents	Gadolinium chelates (safe)	None used
Contrast resolution	Good	Poor
Field of view	Large	Small
Contraindications	Can't be used with implanted metal	No contraindications

Table 2.1: Detailed comparison between MR and US images [Sza04].

Some post-processing techniques used for these images are also discussed. These techniques include super-resolution for MR images and US despeckling. At this point, it is interesting to note that the aim of image fusion is not only to gather information from the MR and US imaging modalities but also to enhance them during the same process.

Generally, the diagnosis and the plan of surgery of endometriosis during the clinical routine are based on:

- The B-mode transvaginal ultrasound image (TVUS): it is a pelvic scan that is performed by a sonographer who records the static images and video clips. The information on the type of machine used varies greatly and the only criteria to adopt the image is the "satisfactory" quality stated by the radiologist and the gynecologist.
- MRI image: the state-of-art MR imaging protocol includes T2 and fat suppressed T1-weighted sequences. The T2-weighted sequences without fat-suppression are assumed to be the best sequences for detecting pelvic endometriosis [BBH+17]. Note that a detailed MRI protocol for endometriosis detection was presented in [FFP+18].

Chapter 3

Fusion and Registration in Medical Imaging

Contents

3.1 Introduction 37

3.2 Medical image fusion 39

  3.2.1 Multi-modal image fusion methods 41

  3.2.2 Conclusion 56

3.3 Medical image registration 57

  3.3.1 Image similarity measure 59

  3.3.2 Transformation models 63

  3.3.3 Regularization in deformable registration 67

  3.3.4 Optimization 69

  3.3.5 Image registration metrics 70

3.4 MR and US registration: state of art 71

  3.4.1 Intensity-based methods 72

  3.4.2 Feature-based methods 74

  3.4.3 Other approach 75

  3.4.4 Conclusion 75

3.5 Global Conclusions 75

3.1 Introduction

Image fusion has received much attention in the literature, in particular for medical imaging applications. These applications include diagnosis and imaging-guided surgery for which the efficiency of experts can be improved for producing an unbiased and objective decision in a short time. However, given the diversity of medical images, it is difficult to find a fusion method adapted to all medical modalities.

An important and fundamental step before medical image fusion is image registration. Indeed, the spatial deformation between medical images cannot be always handled by a fusion method. Fig. 3.1 summarizes the two steps involved in image fusion: (1) image registration and (2) fusion of registered images.

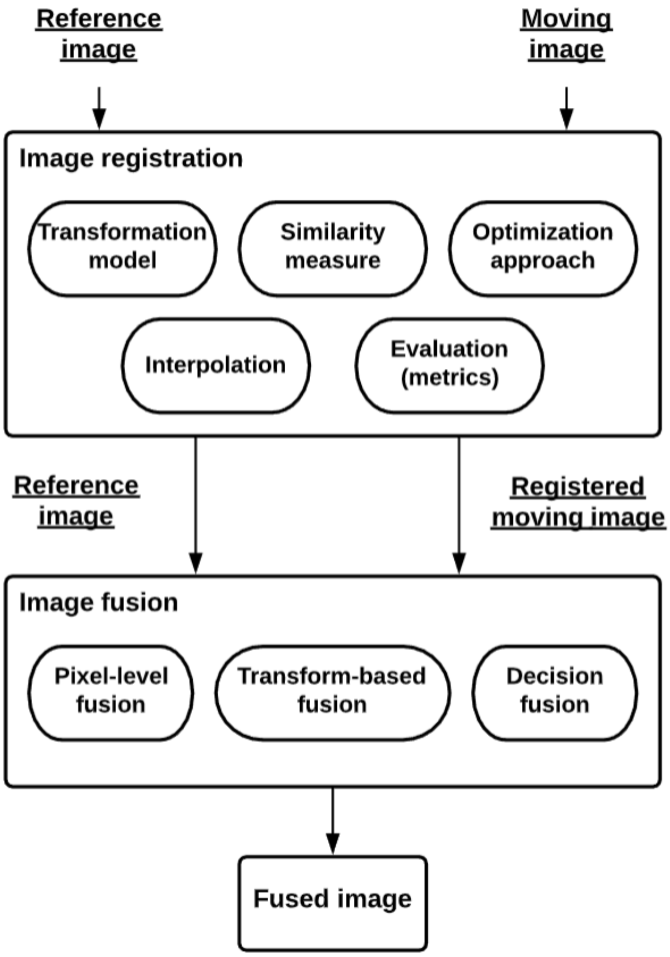

Figure 3.1: A chart summarizing the different steps involved in image fusion.

Since there is, to our knowledge, no state-of-the-art method for the fusion of MR and US images, this chapter primarily provides an overview about medical image fusion/registration including recent attempts to register MR and US images.

3.2 Medical image fusion

Image fusion can be defined as gathering all the important information from multiple images and including them into a fewer number of images, e.g., into one single image. This single image is usually more informative than the images before fusion and contains all the necessary information for the application of interest [ANA18]. Thus, the purpose of image fusion is to build an enhanced image that is informative, comprehensible and accurate for the human. The fusion of medical images is becoming very common for the study of a given pathology and generally allows for better medical decisions in clinical studies. This problem requires solving several technical challenges because of the limitations imposed by specific imaging modalities. A large and growing body of literature has investigated techniques addressing these challenges [JD14b, LBCA10].

Medical image fusion can be mainly classified into three categories: pixel-level fusion, feature level fusion, and decision level fusion. Pixel-level fusion has the advantage of preserving most of the pertinent information in the fused image. Feature-level fusion extracts features from images, such as edges, textures and builds a fusion method using these features. Decision-level fusion refers to methods first segmenting the images of interest into homogeneous regions and use this segmentation to define the fusion method. Medical fusion methods have their own advantages and limitations that are summarized in Table 3.1. The aim of this section is to provide a global view of image fusion in the medical field.

Considering the nature of input images to be fused, medical image fusion can be classified into three main categories: multi-view fusion, multi-temporal fusion and multi-modal fusion (see Table 3.2). Note that multi-modal fusion is very complex and challenging compared to the other categories because it deals with completely different images which makes it difficult to find a relation between the image of interest and the observed images, especially when considering pixel-level fusion.

Advantages	Disadvantages
• Extraction of information from the different images and including this information into a single image facilitating image analysis for the medical experts. • Facilitate identification and image recognition • Reduce the data storage requirement and facilitate its transmission	• Loss of information • Noise sensitivity and creation of artefacts • Absence of a generic technique applicable to all modalities • Expensive

Table 3.1: Main advantages and disadvantages of medical image fusion.

Fusion category	Image 1	Image 2	Fused image
Multi-view fusion refers to the fusion of images having the same modality and being acquired from different views or using different conditions, e.g. see [RGN+11] for the fusion of multi-view US images.	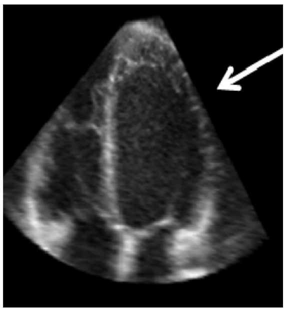		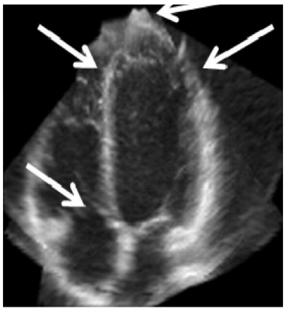
Multi-temporal fusion refers to the fusion of images having the same modality acquired at different times, e.g., see [PAJ16] for the fusion of multi-temporal CT scans.			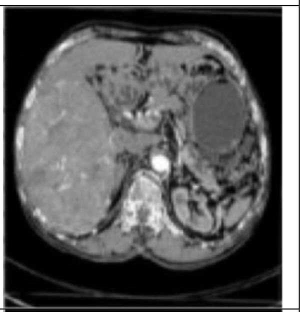
Multi-modal fusion refers to the fusion of input images having different modalities such as MR and CT images [BKGD17]	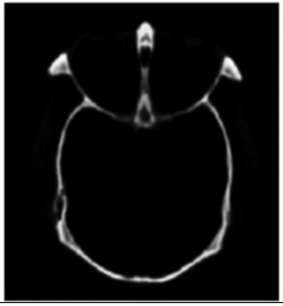	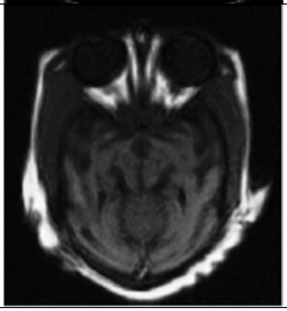	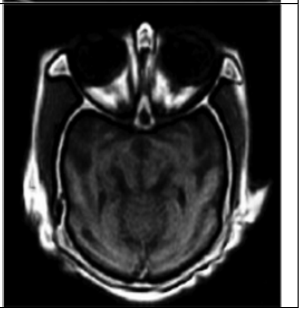

Table 3.2: Examples of image fusion considering the main categories of medical image fusion: multi-view fusion, multi-temporal fusion and multi-modal fusion.

3.2.1 Multi-modal image fusion methods

The image fusion models generally assume that the input images (to be fused) are aligned and that there is no geometric distortion between them, which can be obtained after an accurate registration (see Section 3.3). In this section, we summarize the most known and used medical image fusion methods. Generally, multi-modal image fusion follows three major steps:

1. Input images are decomposed into sub-images or features using image decomposition algorithms.
2. Fusion rules are used to combine information from these sub-images into fused sub-images.
3. The fused image is reconstructed from the fused sub-images using image reconstruction algorithms.

Finally, quality measures are used to evaluate the quality of fused images. Fig. 3.2 summarizes the stages of multimodal image fusion and illustrates each stage with examples of algorithms and methods.

3.2.1.1 Image decomposition and reconstruction

Multi-resolution analysis has been extensively considered for the fusion of medical images. Several decomposition and reconstruction algorithms have been introduced in the literature. In this section, we introduce three different key methodologies that are widely used in medical image fusion: 1) discrete wavelet transform, 2) Laplacian pyramid transform and 3) sparse representation.

Discrete Wavelet Transform (DWT)

The discrete wavelet transform is the most common transform used in image fusion. The image $\boldsymbol{X}$ goes through two filters (with lowpass and highpass impulse responses) in both horizontal and vertical directions whose outputs are decimated by 2 (dyadic decomposition). This process is repeated depending on the desired decomposition level (as illustrated in Fig. 3.3). Generally, the level of decomposition should depend on the input image resolution: images with high resolution require higher level of decomposition than low resolution images. The filtering operation can be defined as the convolution of the vectorized image and the impulse response $\boldsymbol{l}$:

$$\boldsymbol{Y}[n] = (\boldsymbol{X} * \boldsymbol{l})[n] = \sum_{k=-\infty}^{\infty} \boldsymbol{X}[k]\boldsymbol{l}[n-k]. \tag{3.1}$$

where $\boldsymbol{l} \in \{\boldsymbol{h}, \boldsymbol{g}\}$, $\boldsymbol{h}$ and $\boldsymbol{g}$ are the low and the high pass filters.

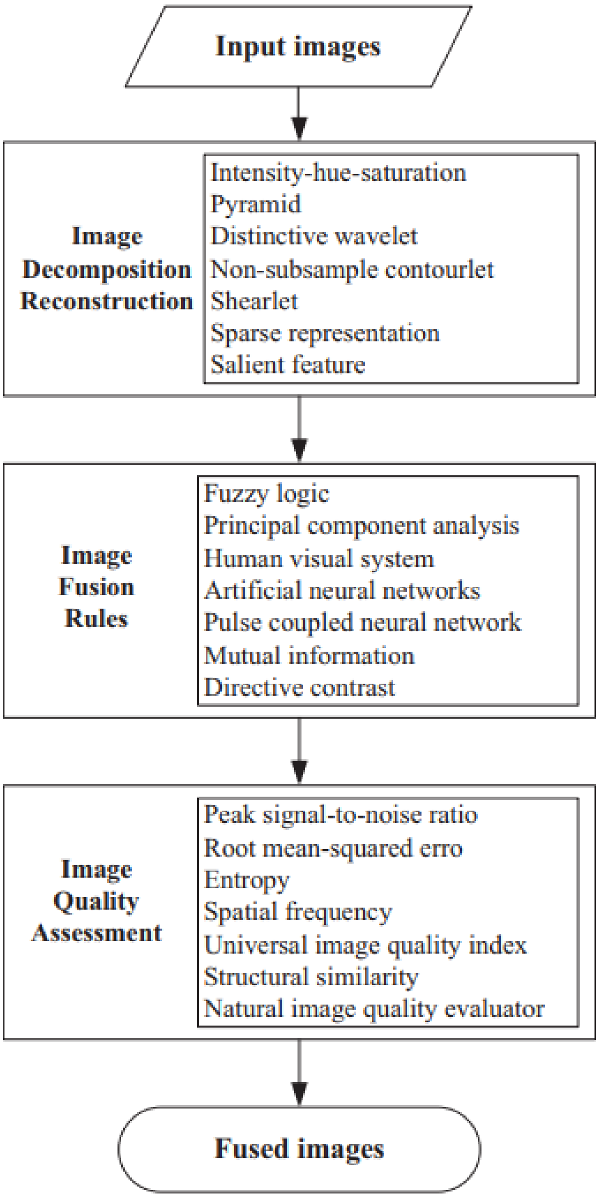

Figure 3.2: Stages of multimodal image fusion [DLLX16].

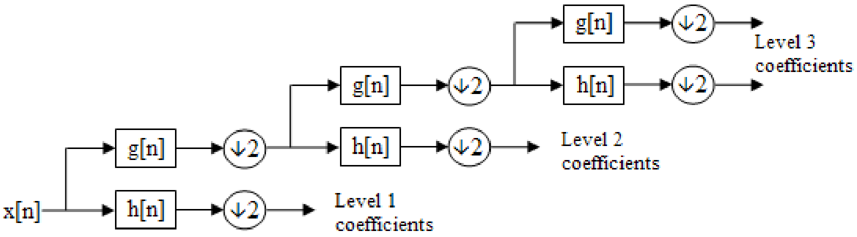

Figure 3.3: Block diagram for the discrete wavelet transform where g is a low pass filter and h is a high pass filter [CZW09].

Fig. 3.4 summarizes the framework of wavelet-based fusion methods. Fusion rules that are usually used with wavelet transforms are introduced in Section 3.2.1.2.

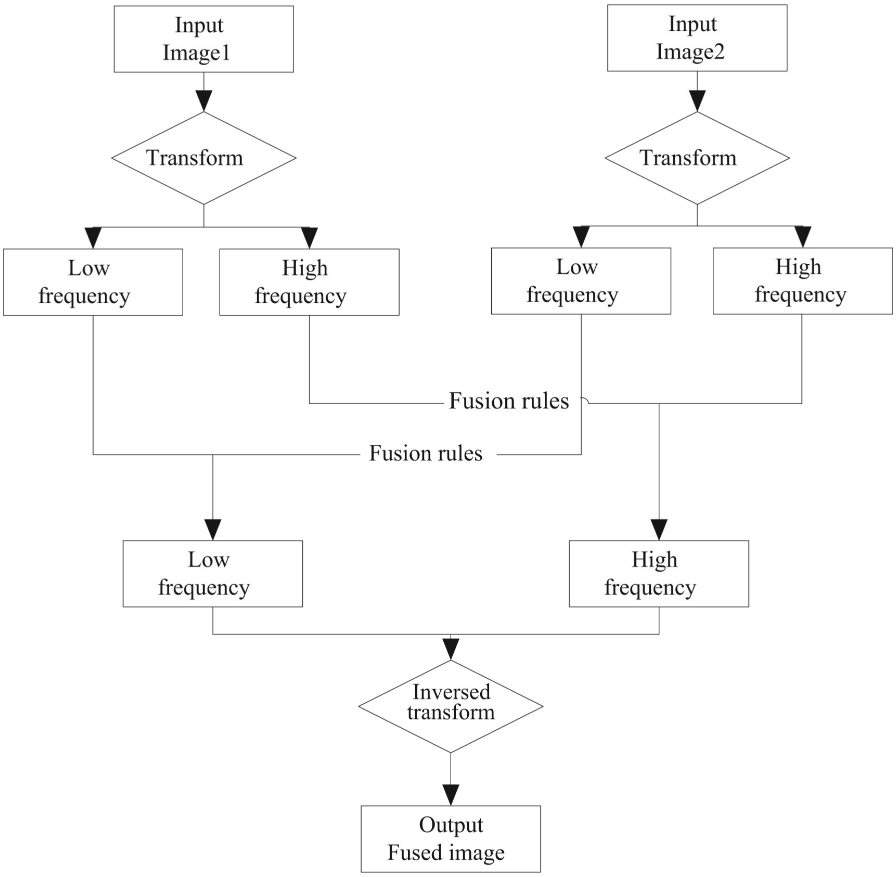

Figure 3.4: Block diagram of wavelet-based fusion methods.

This technique originates at 1995 where Hui Li introduced in [LMM95] a multisensor image fusion using the wavelet transform with an area-based maximum selection rule which consists in selecting the largest wavelet coefficient to build the fused image. In 2001, Guihong Qu [QZY01] applied the same technique with the same fusion rule to fuse MR and CT scans. In [GKMT06], a region-based image fusion technique was introduced to fuse MR T1 and T2 images. Note that the discrete wavelet transform was also used in other image processing applications. These applications include image enhancement (denoising, super-resolution, etc) [ZTL$^+$04], image segmentation [GKMT06] and image visualization (color visualization, pseudo coloring, etc) [Cia10, KHN96].

The DWT is known to suffer from a shift dependency. To overcome this limitation, Rockinger [Roc97] studied an image sequence fusion method using a shift-invariant wavelet transform. This approach improves the temporal stability and consistency of the fused image. Zhang [ZG09] investigated an undecimated, shift-invariant contourlet transform for image fusion. An alternative based on the directional curvelet transform (CVT) was proposed in [TLPP07] for image decomposition while preserving the sparsity of the coefficient set. Wavelets were also combined to other transforms with other approaches such as the contourlet transform [DV05], which combines the Laplacian pyramid with a directional filter bank. Wavelets can also be used to fuse features constructed as the output of a neural networks, as suggested in [LZG07, ZTL$^+$04].

The Pyramid Transform

The pyramid transform is defined by a blurring and downsampling operators applied to the image several times (defining several levels of downsampling). There are multiple kernels that can be used to generate pyramids. Laplacian pyramid decomposition has been demonstrated to be accurate in the fusion context. It uses a Gaussian filter as blur operator and uses the difference between images at adjacent levels in the pyramid to enable the reconstruction of the high resolution image. Fig. 3.5 shows a three level Laplacian pyramid transform applied to a brain MR image. The base images are b1, c1 and d1 and the difference images are b2, c2 and d2.

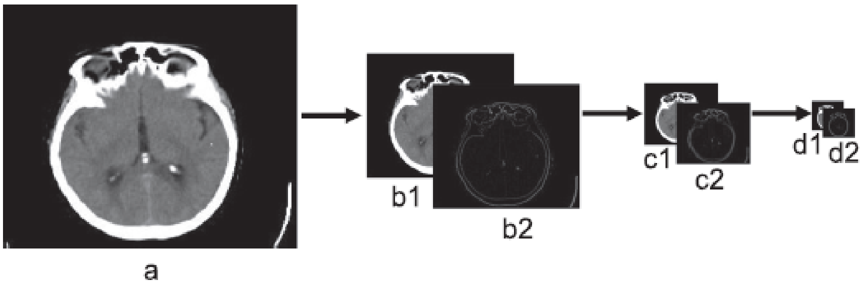

Figure 3.5: An example of a three level Laplacian pyramid transform applied to a brain MR image [DLXN16].

An image $\boldsymbol{I}$ can be decomposed into a base image $\boldsymbol{B}_i$ and a difference image $\boldsymbol{D}_i$ at the ith level using the following convolutions:

$$\begin{aligned} \boldsymbol{B}_i &= \boldsymbol{h} * \boldsymbol{L}_i \\ \boldsymbol{D}_i &= \boldsymbol{g} * \boldsymbol{L}_i \end{aligned} \tag{3.2}$$

where $\boldsymbol{h}$ and $\boldsymbol{g}$ are respectively low and high pass filters, and $\boldsymbol{L}_i$ can be written as

$$\boldsymbol{L}_i = \begin{cases} \boldsymbol{I} & \text{if } i = 0 \\ \boldsymbol{s} * \boldsymbol{L}_{i-1} & \text{otherwise} \end{cases} \tag{3.3}$$

where $\boldsymbol{s}$ is a smooth Gaussian kernel with a downsampling operator.

Laplacian pyramid fusion consists of three phases (displayed in Fig. 3.6): image decomposition, image fusion using accurate fusion rules and reconstruction of the fused image using inverse Laplacian pyramid transform. One of the most common fusion rules in Laplacian pyramid fusion is the average scheme for the base images and the maximum for the difference images as shown is Eq. (3.4)

$$\begin{aligned} \boldsymbol{B}_i^f &= \frac{\boldsymbol{B}_i^1 + \boldsymbol{B}_i^2}{2} \\ \boldsymbol{D}_i^f &= \max(\boldsymbol{D}_i^1, \boldsymbol{D}_i^2) \end{aligned} \tag{3.4}$$

where $.^f$ denotes the fused image, $.^1$ and $.^2$ are the images to fuse. Section 3.2.1.2 presents other fusion rules that are used with the pyramid methods. Finally, the reconstruction of the fused image is implemented using the inverse Laplacian pyramid transform.

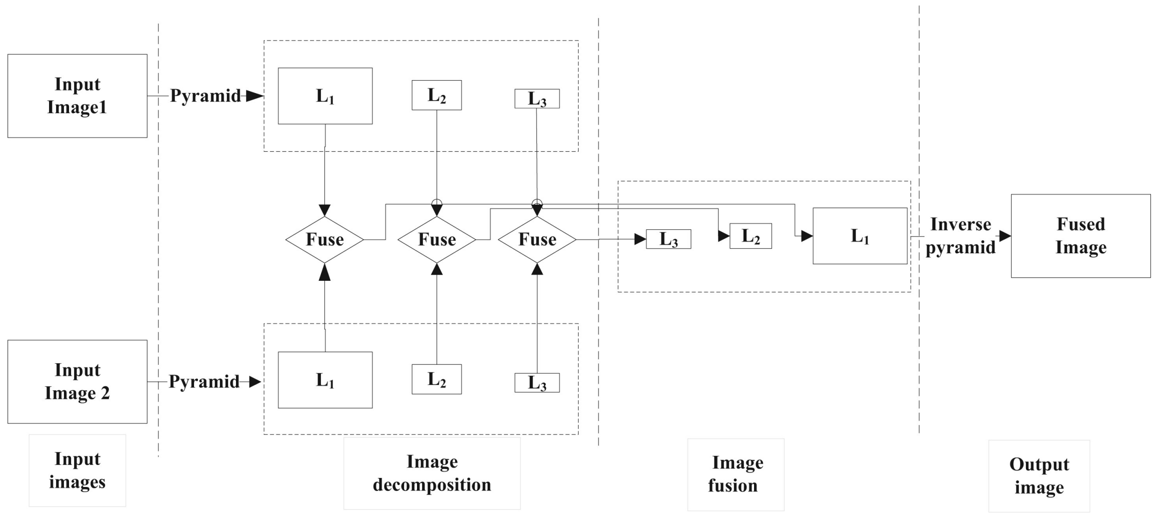

Figure 3.6: Block diagram of three level Laplacian pyramid based fusion method [DLXN16].

Multi-scale fusion methods based on the Laplacian pyramid transform became rapidly popular because of their simplicity and accuracy. This approach is used for the fusion of different imaging modalities such as MR and CT scans, MR and SPECT scans and MR and PET scans [DLXN16, SBK+14, IP11, LDZL18]. However, multi-scale fusion methods are known to be expensive in terms of time computation, data storage, and management, especially when it comes to processing large images since the level of the transform depends on the resolution of input images. To overcome these limitations, Ancuti proposed in [AAVB16] a single-scale fusion method where the subband images obtained by the multi-scale decomposition at several levels are reduced to a single level process. This approach provided insightful results for MR and CT fusion.

Sparse representation methods

Sparse representations (SRs) exploit the sparsity of signals, considering the physiological characteristics in the human visual system. SRs can be viewed as transform-based methods, which have been used in different image processing applications such as image enhancement [FTT14, FLM+13], image classification [XWCY15, NBK14], image denoising [LYF12, HLZ+17], image debluring [LLS+13], image recognition [MJ20] and multi-modal image fusion [ZQ17]. SRs were first considered in medical image fusion by Li [LYF12].

Different from the other transform-based fusion methods, SRs make the assumption that the high and the low frequency images share the same set of sparse coefficients [YLF13, DLLX16]. The procedure of SR fusion can be summarized as follows:

1. Vectorization of the input images $\boldsymbol{I}_1$ and $\boldsymbol{I}_2$.
2. Decomposition of the two images using an overcomplete dictionary $\boldsymbol{D}$. The K-SVD method is a classical dictionary learning method, which has been used intensively for image fusion [ZFLZ13]. The decompositions of the two images $\boldsymbol{I}_1$ and $\boldsymbol{I}_2$ are defined as

   $$\boldsymbol{I}_1 = \boldsymbol{D}\boldsymbol{S}_1$$
   $$\boldsymbol{I}_2 = \boldsymbol{D}\boldsymbol{S}_2,$$

   where $\boldsymbol{S}_1$ and $\boldsymbol{S}_2$ are the sparse representations of $\boldsymbol{I}_1$ and $\boldsymbol{I}_2$ and $\boldsymbol{D}$ is the common dictionary for the two images.
3. Combination of the sparse coefficients using an appropriate fusion rule

   $$\boldsymbol{S}_f = f(\boldsymbol{S}_1, \boldsymbol{S}_2),$$

   where $\boldsymbol{S}_f$ contains sparse coefficients (see Section 3.2.1.2 for examples of fusion rules).
4. Reconstruction of the fused image using the overcomplete dictionary $\boldsymbol{D}$:

   $$\boldsymbol{I}_f = \boldsymbol{D}\boldsymbol{S}_f.$$

However, the conventional sparse representations have two major limitations: 1) details, structures, and edges in the input images are often smoothed and 2) the fused image can suffer from an important loss of information if the dictionary has not been constructed properly. In the few past years, many studies considered a combination of multi-scale approaches and SR techniques to overcome their limitations and to robustify the fusion method [LSH$^+$18, Yin15, LLW15]. In particular Yu Liu studied in [LLW15] a fusion framework where the multi-scale transform is first applied on the pre-registered input images to obtain low-frequency and high-frequency images. In a second step, the base images, i.e., the low pass components of the multi-scale transform, are fused using a SR-based method, and the high-pass bands are merged using another fusion rule. Finally, the inverse multi-scale transform was applied to reconstruct the fused image. Various multi-scale transforms have been considered including the Laplacian pyramid and the discrete wavelet transform. Results on MR and CT scan fusion show that the joint SR and MST techniques outperform the individual SR and multi-scale transform (MST) methods (Fig. 3.7 summarizes the steps of this fusion method).

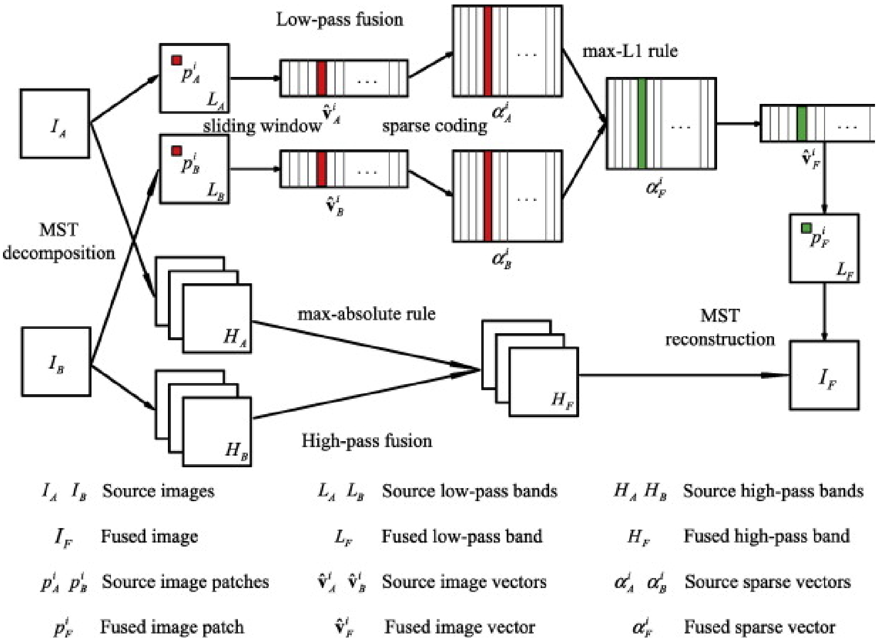

Figure 3.7: A diagram scheme of a joint SR and MST fusion method [LLW15].

3.2.1.2 Fusion Rules

Image fusion rules combine multiple images or sub-images into a single image/sub-image. Popular coefficient combinations include maximum rules (MR) which consist in selecting the largest coefficient to build the fused image, or average rules (AR) and weighted average rules (WAR) defined as

$$C_i^F = \frac{1}{2}(w_i^1 C_i^1 + w_i^2 C_i^2) \tag{3.5}$$

where C_i^F is the fused coefficient, C_i^1 and C_i^2 are the coefficients of the input images and w_i^1 and w_i^2 are appropriate weights.

In the following, image fusion rules that are widely combined with image decomposition methods (Section 3.2.1.1) are introduced. Note that these fusion rules can be applied directly on image pixels instead of the coefficients obtained after image decomposition as in [PM11, WMG10].

Principal Component Analysis

Principal component analysis (PCA) consists in transforming correlated variables into new decorrelated variables referred to as "principal components". PCA allows the number of variables to be reduced, which makes the information less redundant. The PCA fusion rule is a weighted average rule where the weights (w_1, w_2) are computed by the eigenvalues (v_1, v_2) of the covariance matrice $\text{cov}(\boldsymbol{C}_1, \boldsymbol{C}_2)$, where $\boldsymbol{C}_1$ and $\boldsymbol{C}_2$ denote the vectorized coefficients of input images, i.e.,

$$w_1 = \frac{v_1}{v_1 + v_2} \quad w_2 = \frac{v_2}{v_1 + v_2}.$$

Finally, the vectorized fused coefficients can be written as follows:

$$\boldsymbol{C}_F = w_1 \boldsymbol{C}_1 + w_2 \boldsymbol{C}_2.$$

Other fusion techniques based on PCA have been investigated in [WX09, AASAI09, HLLW10]. PCA can be used side by side with other techniques for medical image fusion such as wavelet transforms [CZW09]. Another fusion method is based on Hidden Markov Trees (HMT) [JLY, WLT14] which assumes that the coefficients resulting from an HMT model come from a mixture of two Gaussian distributions associated with the intra-coefficients and a quad-tree model for the inter-coefficients.

Visibility

The visibility is a human visual system that simulates the human process of image recognition to evaluate the quality of an image. It is used in several studies as a fusion rule [AA15]. Fusion methods based on the visibility provide better details that are conform to the human observer and reduce the blurriness of the fused image. The visibility of an image denoted as v_i can be expressed as:

$$v_i = \frac{1}{N} \sum_{j=1}^{N} \frac{|C_i(j) - \mu_i(j)|}{(\mu_i(j))^{\alpha+1}} \quad i \in 1, 2 \tag{3.6}$$

where $\boldsymbol{C}_1$ and $\boldsymbol{C}_2$ are the vectorized coefficients of the input images, N is the size of the vectors $\boldsymbol{C}_i$, μ_i is the mean vector of $\boldsymbol{C}_i$ and α is a constant that ranges from 0.6 to 0.7.

The fused coefficients can be written as:

$$\boldsymbol{C}_F = w_1\boldsymbol{C}_1 + w_2\boldsymbol{C}_2 \tag{3.7}$$

where

$$w_1 = \frac{v_1}{v_1 + v_2} \quad w_2 = \frac{v_2}{v_1 + v_2}$$

Artificial neural networks

Artificial neural networks (ANN) are inspired by the human brain, where neuron nodes are interconnected like a web. The human brain has hundreds of billions of cells called neurons, each neuron being responsible for information processing. Similar to the human brain, an ANN needs a set of learning rules called backward propagation of error for processing features and making global decisions. An ANN goes through a training step where it learns to recognize patterns in data, which can be oral, visual or textual. During this supervised step, the network compares its produced output with the ground truth (the desired output). The difference between these outcomes is corrected using backward propagation of errors. The basic ANN works backward, starting with the output unit and goes to the input units to adapt the connection weights between the units in order to reduce the difference between the output of the network and the desired output.

An example of ANN models that is usually used as a fusion rule is the pulse-coupled neural network (PCNN). It is a feedback network composed by several neurons. Each neuron is composed by branching trees, linking-field model and pulse generators. For more details, the reader can refer to the detailed review [WWZM16]. Authors introduced the basis of statistical analysis and some modified PCNN models.

An ANN is able to analyze, predict, and infer information from a given data without going through rigorous mathematical models, which is an important advantage especially for image fusion. This makes the neural network attractive for image fusion.

The ANN have been used successfully for several applications of medical imaging including breast cancer detection [LZW+11, WWN+06, WHMA04], medical image classification [HAA17, LF98], cancer diagnosis [SGD04, SKH+03] and micro-calcification diagnosis [SKH+03]. However, a fusion image technique based on neural networks is limited by the quality of the training data and the convergence rate of the algorithm. To overcome this limitation, ANN fusion can be combined with other strategies such as the wavelet transform [ZTL+04, LZG07], fuzzy logic [WDLL07, TWZW10, MM09], support vector machines, Gaussian mixtures [LZW+11] and the Laplacian pyramid transform [DK12].

3.2.1.3 Image fusion metrics

The assessment of image fusion quality is fundamental in multi-modal image fusion because it helps to design the best algorithm. Metrics from several image processing fields can be used for medical image fusion such as: root-mean square error (RMSE), mutual information (MI), structural similarity (SSIM), image entropy (EN), peak signal to noise ratio (PSNR) and standard deviation (STD). Some performance measures have also been specifically designed to assess the performance of image fusion method such as: the universal image quality indexing (UIQI), the fusion factor (FF), the feature similarity index metric (FSIM), Xydeas and Petrovic metrics. All these quality measures are regrouped in this section.

3.2.1.4 Root-mean square error (RMSE)

RMSE [CD14] are based on arithmetic theory and quantify the difference between the fused image and the reference image:

$$\mathrm{RMSE} = \sqrt{\left(\sum_{i=1}^{M}\sum_{j=1}^{N}[\boldsymbol{I}(i,j) - \boldsymbol{I}_f]^2\right)} \tag{3.8}$$

where $\boldsymbol{I} \in \mathbb{R}^{M\times N}$ and $\boldsymbol{I}_f \in \mathbb{R}^{M\times N}$ are the reference and fused images.

3.2.1.5 Peak signal to noise ratio (PSNR)

PSNR [KY12] is the ratio between the maximum possible power of a signal and the power of the corrupting noise. It can be used in image fusion as an objective quality measurement. PSNR can be computed as follows:

$$\mathrm{PSNR} = 20\log(\max(\boldsymbol{I}, \boldsymbol{I}_f)) - 10\log(\mathrm{RMSE}). \tag{3.9}$$

3.2.1.6 Mutual information (MI)

The mutual information (MI) [CCB06] measures the mutual dependence between two variables. In image fusion, MI quantifies the amount of information transferred from the input images to the fused image using the following definition:

$$\mathrm{MI}(\boldsymbol{I}, \boldsymbol{I}_f) = H(\boldsymbol{I}) + H(\boldsymbol{I}_f) - H(\boldsymbol{I}, \boldsymbol{I}_f) \tag{3.10}$$

where $H(\boldsymbol{I})$ and $H(\boldsymbol{I}_f)$ are the marginal entropies of $\boldsymbol{I}$ and $\boldsymbol{I}_f$ and $H(\boldsymbol{I}, \boldsymbol{I}_f)$ is the joint entropy of the pair $(\boldsymbol{I}, \boldsymbol{I}_f)$.

The normalized mutual information (NMI) [MVR+10] is also widely used to compare image fusion methods and is defined by

$$\mathrm{NMI} = 2\left(\frac{\mathrm{MI}(\boldsymbol{I}_1, \boldsymbol{I}_f)}{H(\boldsymbol{I}_1) + H(\boldsymbol{I}_f)} + \frac{\mathrm{MI}(\boldsymbol{I}_2, \boldsymbol{I}_f)}{H(\boldsymbol{I}_2) + H(\boldsymbol{I}_f)}\right) \tag{3.11}$$

where $\boldsymbol{I}_1$ and $\boldsymbol{I}_2$ are the two observed images.

3.2.1.7 Structural similarity index measure (SSIM)

SSIM [DY11] is another type of metric, which measures how well the salient information is transferred from the input image to the fused image. SSIM is based on three quantities based on: luminance, contrast and structure (denoted as l, c and s):

$$\mathrm{SSIM}(\boldsymbol{I}, \boldsymbol{I}_f) = \Big(l(\boldsymbol{I}, \boldsymbol{I}_f)\Big)^{\alpha}\Big(c(\boldsymbol{I}, \boldsymbol{I}_f)\Big)^{\beta}\Big(s(\boldsymbol{I}, \boldsymbol{I}_f)\Big)^{\gamma} \tag{3.12}$$

where α, β, γ are weights chosen with respect to the application.

An advanced form of SSIM has been used in image fusion and is referred to as mean structural similarity index measure (MSSIM) [KHC08]. MSSIM calculates the mean of the SSIM values over small patches extracted form the input images which helps to reduce the loss of information about the local structure that can caused while applying SSIM to the whole image. MSSIM is defined as:

$$\mathrm{MSSIM} = \frac{1}{M}\sum_{m=1}^{M} \mathrm{SSIM}(\boldsymbol{I}^m, \boldsymbol{I}_f^m) \tag{3.13}$$

where the index $.^m$ indicates a patch extracted from the corresponding images and M is the number of patches.

3.2.1.8 Image entropy (EN)

The Shannon entropy or information entropy for image processing [GP13] represents the average level of information contained in the image and is defined as:

$$\mathrm{EN}(\boldsymbol{I}) = -\sum_{x} p_x \ln p_x \tag{3.14}$$

where p_x is the number of pixels whose values are equal to x divided by the total number of pixels. In image fusion, some metrics based on image entropy are widely used such as the difference of entropy between images (DEN)

$$\mathrm{DEN} = |\mathrm{EN}(\boldsymbol{I}) - \mathrm{EN}(\boldsymbol{I}_f)|. \tag{3.15}$$

3.2.1.9 Universal image quality indexing (UIQI)

Universal image quality indexing (UIQI) [BLCL08] is based on the structural information in the image. It combines the loss of correlation, luminance distortion and contrast distortion between images. It can be mathematically writing as follows:

$$\mathrm{UIQI} = \frac{\sigma_{\boldsymbol{I}\boldsymbol{I}_f}}{\sigma_{\boldsymbol{I}}\sigma_{\boldsymbol{I}_f}} \times \frac{\mu_{\boldsymbol{I}\boldsymbol{I}_f}}{(\mu_{\boldsymbol{I}}\mu_{\boldsymbol{I}_f})^2} \times \frac{\sigma_{\boldsymbol{I}}\sigma_{\boldsymbol{I}_f}}{(\sigma_{\boldsymbol{I}})^2 + (\sigma_{\boldsymbol{I}_f})^2}. \tag{3.16}$$

where μ and σ denote the mean and the standard deviation of images.

3.2.1.10 Fusion factor (FF)

The fusion factor [CLBC] is an operator based on the mutual information defined as:

$$\mathrm{FF} = \mathrm{MI}(\boldsymbol{I}_1, \boldsymbol{I}_f) + \mathrm{MI}(\boldsymbol{I}_2, \boldsymbol{I}_f) \tag{3.17}$$

where $\boldsymbol{I}_1, \boldsymbol{I}_2$ and $\boldsymbol{I}_f$ are the input images and the fused image. Large value of FF means that the fused image contains a lot of amount of information from the input images.

Th fusion symmetry factor can also be calculated to indicates the degree of symmetry in the information content from input images

$$\mathrm{FS} = |\frac{\mathrm{MI}(\boldsymbol{I}_1, \boldsymbol{I}_f)}{\mathrm{MI}(\boldsymbol{I}_1, \boldsymbol{I}_f) + \mathrm{MI}(\boldsymbol{I}_2, \boldsymbol{I}_f)} - 0.5| \tag{3.18}$$

where $|.|$ is the absolute value. A low value of FS indicates a good symmetry in the fused image.

3.2.1.11 Feature similarity index metric (FSIM)

The feature similarity index metric (FSIM) [ZZMZ11] quantifies the feature similarity (e.g., for edges) between the fused and input images. It can be computed as follows:

$$\mathrm{FSIM} = \frac{\sum_{x\in\Omega} S_L(x) PC_m(x)}{\sum_{x\in\Omega} PC_m(x)} \tag{3.19}$$

where Ω is the image domain, S_l is the total similarity and PC_m is the congruency value [ZZMZ11].

3.2.1.12 Petrovic metric

The Petrovic metric [CP00] associates the visual information to the edge information in each pixel. Thus, a measure of fusion performance is obtained by evaluating the amount of edge information that is transferred from the reference image to the fused image:

$$Q_p^{I_1 I_2/I_f} = \frac{\sum_{n=1}^{N} \sum_{m=1}^{M} Q^{I_1 I_f}(n,m) w^{I_1}(n,m) + Q^{I_2 I_f}(n,m) w^{I_2}(n,m)}{\sum_{n=1}^{N} \sum_{m=1}^{M} w^{I_1}(n,m) + w^{I_2}(n,m)} \tag{3.20}$$

where $Q^{I_1 I_f}, Q^{I_2 I_f}$ are the edge preservation values weighted respectively by $w^{I_1}$and w^{I_1}.

3.2.2 Conclusion

The fusion of MR and US images is a complex problem considering the different image formation models, noises, resolutions, contrasts and also the nature of US images which can be seen as gradient images due to their sensitivity to acoustic impedance changes between neighbouring structures. Thus, transform-based methods are not specifically appropriate for the fusion of MR and US images. In

Chapter 4, we will consider a wavelet-based method with an average weighted rule as in [LBCA10] and a Laplacian-based method as in [AAVB16] for the fusion of MR and US images. Our results will show the sensitivity of these methods to the presence of speckle noise: for low SNR, the multi-scale fused image and the wavelet fused image contain distracting halos artefacts, especially in the regions containing strong transitions between organs.

Note that the ANN-based fusion methods are difficult to apply to our fusion problem since registered MR and US images are very hard to acquire which makes difficult the construction of a rich training database.

3.3 Medical image registration

This section provides an overview of image registration methods that have been studied in the literature. Medical image registration can be defined as the task of estimating the optimal spatial transformation in order to bring two medical images (reference image and moving image) into spatial alignment. Image registration is a crucial phase for multiple image analysis problems that combine information from different sources. The images to be registered may come from the same modality (same sensor), acquired at different times or from multiple modalities associated with different sensors. Medical image registration has been used in several applications. These applications include:

- Multi-temporal image analysis, where images of the same scene are captured at different times with different conditions. Registration of these images allows clinicians to follow disease progression.

- Multi-modal image fusion, where images acquired with different sensors are aligned to apply image fusion techniques and improve the clinical diagnosis.

- Construction of atlases: an atlas refers to a specific model for a population of images with parameters that are learned from a training dataset. This dataset generally requires to be registered.

- Dynamic image sequence analysis: it is used to capture and quantify motion of an anatomy such as the cardiac cycle of the heart or the motion of lungs.

Image registration methods can be classified into two main approaches: (1) intensity-based methods and (2) feature-based methods. Intensity-based methods compare the intensity of pixels/voxels, the intensity of gradients or statistical information related to the intensity of pixels/voxels. Conversely, feature-based methods compare structures extracted from images such as contours, edges, surfaces, set of points, graphs and volumes.

Any registration algorithm requires the following ingredients (see Fig. 3.8).

1. **Cost function**: it is defined as an image similarity measure that quantifies the degree of similarity between the two images to be registered and a regularization term to use in the optimization process. The regularization is necessary since the similarity measure term generally leads to an ill-posed problem according to Hadamard's definition[1]. If F is the cost function, F_s the similarity term and R_s the regularization term, the following relation is obtained

$$F(T, \boldsymbol{I}_r, \boldsymbol{I}_m) = F_s(T, \boldsymbol{I}_r, \boldsymbol{I}_m) + \tau R_s(T) \tag{3.21}$$

   where τ is a regularization parameter, $\boldsymbol{I}_m$ denotes the moving image, $\boldsymbol{I}_r$ is the reference image, $T : \Omega_r \to \Omega_m$ is the geometric transformation, Ω_r and Ω_m are the reference and the moving image domains.

2. A model for the **geometric transform** T, which can be linear (e.g., affine) or non-rigid (also called elastic) enabling images to be registered with local geometric differences.

3. An **optimization technique** that minimizes/maximizes the cost function (3.21) in order to estimate the optimum transformation that aligns the images to be registered.

4. **Interpolation**: applying a geometric transform in images requires to construct new data points within the range of a discrete set of known data points in the image.

---

[1] Hadamard believes that mathematical models of physical phenomena are well posed problems if :

- a solution exists,
- the solution is unique,
- and the solution behaviour changes continuously with the initial conditions.

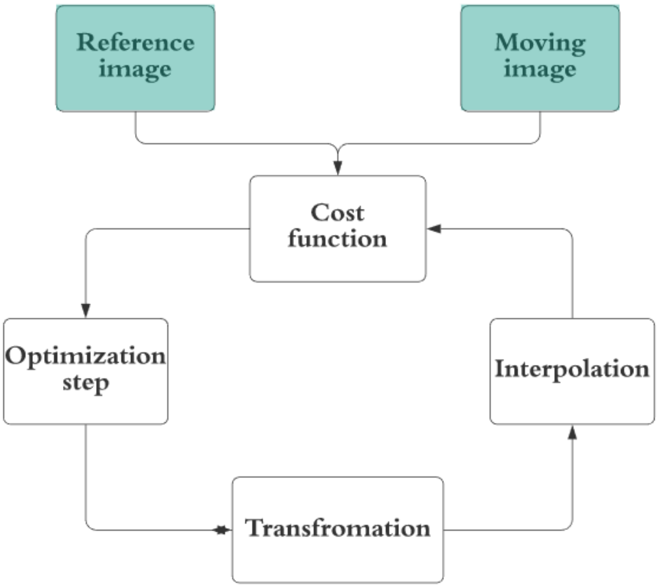

Figure 3.8: A general scheme of an image registration algorithm.

3.3.1 Image similarity measure

Generally, image registration methods are based on the distance between geometric primitives that are extracted manually or automatically from images or use directly the information carried by the gray levels of the images. Hybrid methods use both approaches to mitigate their limitations.

3.3.1.1 Feature-based methods

These approaches are based on the extraction of subsets of points or features and estimate a transformation that allows to points/features to be matched. Identifying the features to extract is a crucial step and must be guided by number of properties: easy and precise detection, distribution of the image, robustness to noise and artefacts. Three types of geometrical primitives can be distinguished: points, curves and surfaces.

The features can be markers attached to the patient anatomy or anatomical features. Extrinsic features are defined using some artificial markers attached to the patient. These markers can be non-invasive such as skin markers. However, it is not realistic since the human skin is elastic and can be deformed easily. The non invasive markers such as stereotactic frames allow a robust and accurate registration and are automatically detectable in images. However, they are uncomfortable for patients and are difficult to be attached. Intrinsic features refer to points, curves or surfaces extracted manually by experts or detected automatically using a feature detection algorithm. The accuracy of this approach depends on the precision of these features and the salient information that they carry. Alam and Rahman introduced two articles: the first one [AR16] is a detailed review about the existing techniques for intrinsic image registration in a comprehensive manner and the second one summarizes the extrinsic registration techniques existing in the literature for medical images [ARU+16].

Several criteria and distances have been proposed in the literature for matching these extracted features:

- To measure the distance between paired points, the standard Euclidean is classically used. Thanks to its analytical properties, in the case of rigid or affine registration, it leads to an analytical solution for the estimation of the transformed parameters:

  $$F_s(T, \boldsymbol{I}_r, \boldsymbol{I}_m) = \sum_i \|p_i - T(q_i)\|_2 \tag{3.22}$$

  where p and q are the two extracted sets of points.

- To measure the distance between two curves, two surfaces or two volumes, several approaches are possible. ICP (iterative closest point) is the most frequently used algorithm: for each point or a selection of points in the point cloud of the moving image, ICP matches the closest point in the point cloud of the reference image. Then, it estimates the least square rigid transformation relating these sets of points and continue until convergence to a local optimum. Generally, ICP is applicable when a relatively good starting point for the initialization of the algorithm is available. Otherwise, it will be trapped into the first local minimum and the solution will not be reliable. ICP was introduced for the fist time for image registration by Besl and McKay in [BM92]. Then, many studies have proposed variants of ICP such as EM-ICP [GP02], fuzzy ICP [KSK96] and GO-ICP [YLCJ15]. The ICP algorithm has been used for the registration of multiple modalities: MR/US images [FAS+12, MJF+12], MR/mammography images [KEBH13], MR/CT scans [SKHB18], CT/PET scans [MCS+07] and CT/SPECT scans [KDM+02].

The major disadvantage of these approaches is that they are very depending on the precision with which the features have been extracted. Another limit concerns the accuracy of the resulting registration, which is guaranteed only in the vicinity of the features. Finally, the main problem with these approaches is that the extraction of features is operator dependent. Note that many automatic and semi-automatic methods have been investigated in the literature [KZW+12, MOM+10].

3.3.1.2 Intensity-based methods

Contrary to feature-based approaches, the intensity-based approaches do not use a preliminary data reduction step. They use the dense information carried by all the pixels/voxels of the image, either by directly comparing the intensity levels or by associating to each pixel/voxel a value determined from gray levels and comparing these sets of values. It is possible to consider differences of pixel intensities such as gradients. Thus, registration can be achieved automatically. Similarity measures allow for the comparison of information carried by the gray level intensities of the image. Each criterion makes an assumption about the relationship that link these intensities. One of the basic alignment measures is the sum of squared intensity differences (SSD) between images defined as:

$$\mathrm{SSD} = \sum_{x} [\boldsymbol{I}_r(\boldsymbol{x}) - \boldsymbol{I}_m(T(\boldsymbol{x}))]^2 \tag{3.23}$$

where $\boldsymbol{x}$ is a pixel/voxel coordinate. SSD is typically used for mono-modal image registration [RA10] because it is very sensitive to the contrast difference that may exist between multi-modal images.

Another measure is the cross-correlation alignment [AEGG08], which assumes that there is an affine relationship between the intensities of the moving and the reference images:

$$\mathrm{CC} = \frac{1}{N\sigma_{\boldsymbol{I}_r}\sigma_{\boldsymbol{I}_m}} \sum_{x} \left(\boldsymbol{I}_r(x) - \mu_{\boldsymbol{I}_r}\right)\left(\boldsymbol{I}_m(T(x)) - \mu_{\boldsymbol{I}_m}\right) \tag{3.24}$$

where $\sigma_{\boldsymbol{I}_r}, \sigma_{\boldsymbol{I}_m}$ are the standard deviation of the reference and moving images and $\mu_{\boldsymbol{I}_r}, \mu_{\boldsymbol{I}_m}$ are the mean of the reference and moving images. CC $= 0$ means that the two images are realizations of uncorrelated random variables and therefore are impossible to register. In the other cases, registration can be obtained by maximizing CC. CC can be used for multi-modal registration such as MR and CT scan registration for brain diagnosis [VdEMPV95, Sam09]. One of the well-known variant form of cross-correlation is the local correlation (LC):

$$\mathrm{LC} = \sqrt{\frac{1}{N_s}\left(\sum_{s_j} \mathrm{CC}^2(s_j)\right)} \tag{3.25}$$

where s_j is the jth extracted patch from both images, CC^2 is the square cross-correlation, N_s is the number of extracted patchs. LC has been used successfully for rigid and non-rigid multimodal registration [ZF03, WRN+99].

A common assumption is to consider that there is a functional relationship between the reference and the moving images. Woods [WGH+98] has proposed an original criterion which proved itself to be efficient for matching PET with MR defined as:

$$\mathrm{Woods} = \sum_i p_i \frac{\sigma_{\boldsymbol{I}_r|j}}{\mu_{\boldsymbol{I}_r|j}} \tag{3.26}$$

where $\sigma_{\boldsymbol{I}_r|j}$ and $\mu_{\boldsymbol{I}_r|j}$ are respectively the standard variation and the mean of the intensities observed in the reference image $\boldsymbol{I}_r$ that corresponds to the pixels/voxels in the moving image $\boldsymbol{I}_m$ with intensities equal to j. Roche proposed in [RPMA01] another functional relationship between images for image registration: the bivariate correlation ratio, which assumes that an unknown polynomial function can link MR and US images.

A completely different approach is to consider a statistical dependency between images. The mutual information was first introduced in [VWI97, CMD+95] to measure the dependency between images. It has been widely used for image registration [MCV+97]. Based on Shannon definition, MI can be written as follows:

$$\mathrm{MI} = \sum_{i,j} p_{i,j} \log \frac{p_{i,j}}{p_i p_j} \tag{3.27}$$

where p_i, p_j are respectively the probability of a pixel/voxel in $\boldsymbol{I}_r$ to have an intensity equal to i and a pixel/voxel in $\boldsymbol{I}_m(T)$ to have an intensity equal to j and $p_{i,j}$ is the joint probability. Note also that the transformation parameter can be estimated by maximizing the mutual information. Note that a robust variant of the mutual information is the normalized mutual information (NMI) [XCT+08].

3.3.2 Transformation models

After defining a similarity measure, a transformation model can be constructed. It should transform the moving image to be superimposed to the reference image. The choice of a transformation model depends on the assumed geometric deformation introduced during the image acquisition, and on the required accuracy of registration. Transformation models can be divided into two main categories based on global models and deformable or local models.

3.3.2.1 Global models

Global models include rigid, affine, similarity, and perspective transformations [OT14b]. A rigid transformation can register objects that are related by a rotation (ϕ) and a translation (t_x, t_y):

$$\begin{aligned} u &= x \cos(\phi) - y \sin(\phi) + t_x \\ v &= x \sin(\phi) + y \cos(\phi) + t_y, \end{aligned} \tag{3.28}$$

where x, y are the coordinate of a pixel i in the moving image before registration and u, v are the coordinate of the same pixel after registration. A rigid transformation preserves distances between all the pixel pairs in the image. It is one of the simplest transforms, which has mainly be used in the context of medical imaging to register images of the same person acquired at different times or in different imaging modalities. The number of degrees of freedom equals 3 for 2D images and 6 for 3D images.

Similarity models are built using a translation (t_x, t_y), a rotation (ϕ), and a scaling (s), i.e.,

$$\begin{aligned} u &= s(x \cos(\phi) - y \sin(\phi)) + t_x \\ v &= s(x \sin(\phi) + y \cos(\phi)) + t_y, \end{aligned} \tag{3.29}$$

A similarity model is generally called shape-preserving because it preserves angles and curvatures. The number of degrees degree of freedom is 4 for 2D images and 7 for 3D images.

An affine transformation is a linear combination of translation, rotation, scaling, and shearing defined as:

$$\begin{aligned} u &= a_0 + a_1 x + a_2 y \\ v &= b_0 + b_1 x + b_2 y. \end{aligned} \tag{3.30}$$

An affine transformation preserves the parallelism of straight lines in the image. This model is generally used in the context of medical imaging for inter-individual registration. However, its low degree of freedom does not allow to accurately capture inter-individual anatomical variability. The number of degrees of freedom is 6 for 2D images and 12 for 3D images.

The perspective transformation can be written as

$$\begin{aligned} u &= \frac{a_0 + a_1 x + a_2 y}{1 + c_1 x + c_2 y} \\ v &= \frac{b_0 + b_1 x + b_2 y}{1 + c_1 x + c_2 y}. \end{aligned} \tag{3.31}$$

It does not keep the parallelism but imposes that the image of a straight line is a straight line. This type of transformation can be used in the context of medical imaging for the registration of radiological images (for this problem, the radiation from a point source interacts with the object to be imaged to form a projection image in a plane) or in virtual reality applications.

3.3.2.2 Non-linear models

Linear models allow only a small number of degrees of freedom and are therefore poorly adapted to capture inter-subject anatomical variability or the morphological variability of certain organs. In many applications, such as brain or abdominal organ registration, it is necessary to use transformations with a large number of degrees of freedom, capable of modifying the overall shape of structures. For this purpose, different non-linear models (called also non-rigid models) can be considered.

Polynomials

A polynomial representation can be used to model the deformation field between the two images. Polynomials of order 2 to 5 have been considered [RPMA01]. Beyond this order, significant oscillations appear, which reduces the interest of this model. A disadvantage of polynomial models is related to their field of application, which is global, making them unsuitable for taking into account local variations in shape. This limitation can be overcome by using polynomial models piecewisely.

Radial basis functions

A radial basis function (RBF) is a function $\psi : \mathbb{R}^n \to \mathbb{R}$ whose value depends on the input and m fixed points called the centers $\boldsymbol{c_i}$ (where $i \in [\![1, m]\!]$) that can be used as control points for registration. The centers must be all different from each other, in order for the interpolation matrix to be non-singular. In the n dimensional Euclidean space $\mathbb{R}^n$, one can define the RBF using the Euclidean norm $\|.\|$ as follows

$$\psi(\boldsymbol{x}) = \sum_{i=1}^{m} w_i \rho(\|\boldsymbol{x} - c_i\|) \tag{3.32}$$

where w_i are the weight of the RBF and $\rho : \mathbb{R}^+ \rightarrow \mathbb{R}$ is an appropriate kernel (see Table 3.3).

Table 3.3: Examples of RBF kernels.

Name of RBF	Kernel $\rho(r)$
Gaussian	$\exp(-\epsilon^2 r^2)$
Multiquadric	$\sqrt{1 + (\epsilon r)^2}$
Inverse quadratic	$\frac{1}{1+(\epsilon r)^2}$
Generalized multiquadratic	$(1 + (\epsilon r)^2)^\beta$
Linear	r
Cubic	r^3
Thin-Plate Spline	$r^2 \log(r)$

In particulat, thin-plate splines (TPS) have received much attention for image registration (see Tab. 3.3) [Roh01]. The TPS transformation between the two images to be registered can be modeled as

$$\begin{aligned} u &= a_0 + a_1 x + a_2 y + \sum_{i=1}^{m} w_i \|\boldsymbol{x} - c_i\|^2 \log\left(\|\boldsymbol{x} - c_i\|\right) \\ v &= b_0 + b_1 x + b_2 y + \sum_{i=1}^{m} w_i \|\boldsymbol{x} - c_i\|^2 \log\left(\|\boldsymbol{x} - c_i\|\right). \end{aligned} \tag{3.33}$$

TPS registration usually leads to very accurate results but is very time consuming, especially for large images. Many studies in the literature considered TPS variants in order to decrease the computation time while preserving its pertinence such as [BN92, PD92].

Cubic B-spline

Another function from the spline family that is used for image registration is the cubic B-spline. A spline can be defined as a piecewise polynomial function defined by knots (the points where the polynomials meet) k_i. The B-spline is a particular spline function that has minimal support with respect to a given degree, smoothness, and domain partition. Cubic B-splines are B-splines of degree 3, which provide good compromise between simplicity and accuracy.

Denote as $\Omega = \{(x, y) \mid 0 \leq x < N,\ 0 \leq y < M\}$ the domain of the image-plane and consider an $n_x \times n_y$ mesh of control points ϕ_{ij} with identical spacing δ, denoted as Φ. The cubic B-spline local transformation is defined as:

$$T_\phi(x, y) = \sum_{m=0}^{3} \sum_{n=0}^{3} B_m\Big(\frac{x}{n_x}\Big) B_l\Big(\frac{y}{n_y}\Big) \phi_{i_x+m, j_y+n}, \tag{3.34}$$

where $i_x = \lfloor\ x/n_x \rfloor - 1$, $j_y = \lfloor y/n_y \rfloor - 1$ and $\lfloor . \rfloor$ is used for the integer part. The cubic B-spline uniform functions are defined as:

$$\begin{aligned} B_0(u) &= \frac{(1-u)^3}{6} \\ B_1(u) &= \frac{3u^3 - 6u^2 + 4}{6} \\ B_2(u) &= \frac{-3u^3 + 3u^2 + 3u + 1}{6} \\ B_3(u) &= \frac{u^3}{6}. \end{aligned} \tag{3.35}$$

Once the grid of the B-spline has been constructed, it is used to deform the local neighborhood of every control point in the moving image. Once the moving image has been deformed, it is compared to the reference image using the similarity measure. The cubic B-spline model has been used for different applications in medical imaging such as registration of CT scan and MR image of heart [KSP07] and motion estimation applied to MR images of the brain [VHS+98].

Elastic body models

Another registration approach is a non-parametric deformation model. In this technique, the object being deformed is modeled as an elastic body. This idea has been introduced by Bajcsy in [BK89]. The image is considered as a rubber sheet where external and internal forces are applied to align images with minimum amount of bending and stretching. The spatial transformation T satisfies the partial differential equation (the Navier Cauchy PDE):

$$\mu\nabla^2 T + (\mu + \lambda)\nabla(\nabla T) = S(T) \tag{3.36}$$

with certain boundary conditions such as $T(z) = 0$ for z located on the image boundary. $S(T)$ is the body force that drives the registration (some examples of the body forces are given in [WS98]), ∇ is the gradient, β and α are the Lamé coefficients. Elastic body models are simple to implement but they are limited by their inability to model large and global deformation.

Viscous fluid Flow models

Viscous fluid Flow models are non-parametric models. The purpose of fluid registration is to imitate a flow of fluid. Fluid registration has been used successfully in medical applications such as brain image registration [DMVS03]. This kind of approach does not assume small deformations and thus is able to model large and smooth deformations while maintaining continuity. The motion of this transformation v is modeled by the Navier-Stokes equation and can be written as:

$$\mu\nabla^2 v + (\mu + \lambda)\nabla(\nabla v) = S(v) \tag{3.37}$$

where μ and λ are are the viscosity constants. The relationship between the transformation T and the velocity v is given by

$$\frac{\partial T(x,t)}{\partial t} = v(x,t) + \nabla T(x,t)v(x,t). \tag{3.38}$$

Even if this model is interesting, it cannot be used in images containing non-fluid objects.

Other examples of non parametric models used for image registration are diffusion models [HS81] and curvative models [FM04]. The diffusion models handle object contours and features, and estimate the smoothness of the deformation field rather than mimicking physical properties as fluid and elastic models.

3.3.3 Regularization in deformable registration

A regularization can be introduced to a transformation model in order to avoid discontinuities in the estimated transformation. For instance, the estimated transformation can be constrained based on prior knowledge about image acquisition, physical conditions, Cartesian coordinate changes, spatial distortion, etc. Two kinds of regularizations have been considered for image registration: (1) competitive regularization, (2) iterative filtering approaches.

3.3.3.1 Competitive regularization

Competitive approaches consist in considering a cost function composed of a data fidelity term based on the similarity measure (see section 3.3.1) F_s and a regularization term R_s that penalizes abrupt variations in the deformation field. The solution obtained by minimizing $F_s(T) + \tau R_s(T)$ satisfies a compromise between the data attachment and the regularity of the solution. The regularization parameter τ make it possible to satisfy this compromise. The regularization term prevents the appearance of small unrealistic deformations which would cause only a slight decrease in the similarity criterion. Different regularization energies have been proposed in the literature, many of them having an interpretation related to material or fluid mechanics. An example of regularization in 2D is

$$R_s(T) = \int_{\Omega} \Big[\frac{\partial^2 T}{\partial x^2} + \frac{\partial^2 T}{\partial y^2} + \frac{\partial^2 T}{\partial x \partial y}\Big] dxdy. \tag{3.39}$$

In practice, the integral (3.39) is approximated by standard numerical integration [RSH$^+$99].

3.3.3.2 Iterative filtering approaches

Iterative filtering approaches [PHF$^+$14] are based on two steps: the first step estimates the transformation T without regularization and the second step is smoothing the estimated deformation using filters. These two steps are repeated several times until convergence. Several filters have been proposed in order to smooth transformations such as Gaussian or adaptive filters. The main disadvantage of these methods is that they do not take into account the information carried by the image during the regularization step, which can lead to smoothing areas containing pertinent information. To overcome this limitation, the filtering can be constrained by a map of weights in order to consider the information in the image. These weights are generally computed using the norm of the gradient image.

3.3.4 Optimization

The aim of optimization is to estimate the optimal transformation that best aligns the reference and source images according to a cost function defined using a data fidelity term (similarity measure) and a regularization term. The choice of an optimization method can impact directly the quality of the estimated transformation. Two categories of optimization methods were considered in [SDP13] depending on the nature of the transformation T: (1) continuous methods and (2) discrete methods.

3.3.4.1 Continuous optimization

Continuous methods deal with variables that take real values and cost functions that are differentiable. Generally, these methods update the unknown parameters (to be estimated) using the following equation:

$$\boldsymbol{\theta}^{k+1} = \boldsymbol{\theta}^{k} + \alpha_k g_k(\boldsymbol{\theta}^{k}) \tag{3.40}$$

where θ contains the parameters of the transformation, k is the iteration number, α_k is the step size at iteration k and g_k is the corresponding search direction. The function g_k depends on the similarity measures and the regularization terms. The stepsize α_k can be constant or may change during the iterations via a line search that satisfies the Wolfe conditions or using the Barzilai–Borwein method. The search direction can use the first order information such as **the gradient descent method**, which is based on the negative gradient:

$$g_k(\boldsymbol{\theta}) = -\nabla E_s(\boldsymbol{\theta}) \tag{3.41}$$

where $E_s(\boldsymbol{\theta}) = F_s(T_{\boldsymbol{\theta}}) + \tau R_s(T_{\boldsymbol{\theta}})$. Gradient descent methods are widely used in image registration. They are used for different similarity measures and transformation models. Beg considered the gradient descent method to register brain images using a least square distance as similarity measure and the diffeomorphic model for the transformation [BMTY05], Klein used this method to register images using mutual information and B-spline transformation [KSP07] and Huang proposed a shape registration based on information theory and free form deformations [HPM06].

Conjugate gradient methods have better rates of convergence than the gradient descent. The search function conjugates the gradient to the previous direction using the following equation:

$$g_k(\boldsymbol{\theta}) = -\nabla E_s(\boldsymbol{\theta}) + \beta g_{k-1}(\boldsymbol{\theta}). \tag{3.42}$$

Some studies that use the conjugate gradient for image registration are [GVM04, PZF08, JSTL07].

Other continuous methods used in medical image registration are: Powell's conjugate direction method [PMV04], quasi-Newton methods [KSP07], Gauss-Newton methods [VPPA07], Levenberg-Marquardt [GTN03] and stochastic gradient descent methods [BGSW07]. All these methods solve unconstrained optimization problems. Constrained methods can be used when it is necessary such as the log-barrier method [HM07].

3.3.4.2 Discrete optimization

Discrete optimization methods are used when the variables to estimate take discrete values. They can be classified into three categories: (1) graph based methods [GPS89], (2) belief propagation methods [YWA10] and (3) linear programming approaches [GKT+08].

A very comprehensive and detailed survey, presented by Klein, is available in [KSP07]. It compares optimization techniques for image registration using mutual information as a similarity measure and a B-spline transformation as a regularization.

3.3.5 Image registration metrics

The evaluation and comparison of registration methods, especially non-rigid registration methods, are challenging problems due to the lack of ground truth. It is indeed difficult for experts to find a consensus on what should be the transformation allowing the best matching of two images. The notion of optimality of the registration seems to be closely linked to the application. The oldest method of registration accuracy is based on visual assessment and is still used at least as complement of some quantitative measures. Global linear registration methods can be evaluated using the mean square error (MSE) [CEA00];

$$\text{MSE} = \frac{1}{N}\sum_{i=1}^{N} \|T(\boldsymbol{p}_{m,i}) - \boldsymbol{p}_{r,i}\| \tag{3.43}$$

where $\boldsymbol{p}_m$ and $\boldsymbol{p}_r$ are points extracted from the moving and the reference image and N is the number of extracted points. The lower the MSE, the more accurate the registration.

The Dice Similarity Coefficient (DSC) is also a metric used for global registration. It was developed by Thorvald Sørensen and Lee Raymond Dice in 1948 [WCH+17]. It can be written as follows:

$$\mathrm{DSC} = \frac{2a}{2a+b+c}. \tag{3.44}$$

where a is the number of pixels shared by the moving and the reference images, b and c are the number of pixels unique to the reference and the moving images. A high value of DSC indicates a good overlap between images, thus, an accurate registration.

Concerning local image registration, a common quantitative metric is the target registration error (TRE) [KKM+09]. It uses two sets of landmarks identified by clinical experts[2] denoted as $\boldsymbol{p}_m = \{p_{m,1}, ..., p_{m,s}\}$ and $\boldsymbol{p}_r = \{p_{r,1}, ..., p_{r,s}\}$ leading to the following measure:

$$\mathrm{TRE} = \frac{1}{s}\sum_{i=1}^{s} \|T(\boldsymbol{p}_{m,i}) - \boldsymbol{p}_{r,i}\|. \tag{3.45}$$

A low TRE corresponds to a good local registration accuracy.

In some studies, the cross correlation CC and the median-absolute deviation metrics are used for a quantitative evaluation of local/global registration methods.

3.4 MR and US registration: state of art

Because of the diversity of images to be registered and the complex deformations affecting medical images, it is very difficult to design a general method that is adapted to all registration problems. In the previous sections, we exposed some fusion and registration methods that have been used for different medical imaging modalities. This section concentrates on the registration of MR and US images, which can be considered under two angles (1) intensity-based methods and (2) feature-based methods.

---

[2] These sets must not be used in estimating the deformation, which can be challenging

3.4.1 Intensity-based methods

The registration of MR and US images using the intensities of these images is a very challenging task. Indeed, US and MR images are very different modalities: a US image can be seen as an image of tissue boundaries contaminated by speckle noise with a small field of view and MR is a large field of view image that provides information on the tissue density (see Chapter 2). For these reasons, basic similarity measures such as the mutual information MI, the cross-correlation ratio (CCR) and the sum of squared distances cannot be used easily to align MR and US images [HHR+05]. Therefore, more complex similarity measures have been proposed for MR and US images; which are summarized in this section.

Roche et al. in [RPMA01] presented an automatic method to rigidly register US and MR images. The similarity measure, used in their work, is based on a bivariate version of the generalized correlation ratio [RMPA98]. In addition, the similarity measure relies on a polynomial function that correlates the US image to the MR and the gradient of MR images in order to model the intensity variations in tissue boundaries. Powell's optimization algorithm was used to implement the bivariate CCR. This approach outperforms the classical CCR and the mutual information. This technique has been designed for image-guided neurosurgery and applied to brain images, which explains the accuracy of a rigid transformation, since the brain is mostly rigid.

Arbel et al. in [AAM+04] proposed an automatic non-linear registration for the same application as Roche et al. (image guided neurosurgery). The technique first predicts the appearance of the US image based on a segmented MR image, providing a so-called pseudo US image. Once a pseudo-US has been generated, the system computes a nonrigid registration based on a piecewise linear deformation using the ANIMAL algorithm [CE97]. This method provided some insightful results for the recovery of deformations due to brain shift and operative manipulations.

Craene et al. in [DCdBdM+04] studied a non-rigid MR/US registration algorithm based on a finite element elastic deformation model to capture the deformation in the liver ablation and the prostate biopsy. The similarity measure used in this study was a mix between mutual information and linear elastic energy. The optimization was performed using a new method referred to as Perturbation Stochastic Approximation (PSA). The use of volumetric meshes applied to the surfaces of organs to build the deformation showed promising results.

Mitra et al. in [MMO$^+$12] proposed a 2D deformable registration that aligns a pre-biopsy MR image and a transrectal ultrasound image (TRUS). TRUS imaging is used to guide prostate biopsy. A combination with pre-biopsy MR may help to improve the detection of early stage malignancy. The method studied in [MMO$^+$12] involves B-spline free-form deformations and a similarity measure based on the normalized mutual information between the two images. Their main contribution was to compute the NMI from the texture images obtained from the amplitude responses of directional quadrature filters. The entropy between MR and TRUS intensity images is more than the entropy between texture images because of the variations of gray levels. Using the texture images helps NMI to better catch the (dis)similarities between MR and TRUS images. The optimization of the resulting cost function was performed with a quasi-Newton algorithm. The results clearly outperform a B-spline registration relying on NMI based on gray level intensities.

A different approach is based on the modality neighborhood descriptor (MIND) [HJB$^+$12] and its variant based on a self-similarity context (SSC) [HJP$^+$13, RKC14]. These methods do not rely on global intensity relations but use the difference of pre-defined neighborhood maps. [RKC14] proposes a self similarity α-MI (SeSaMI) metric as a similarity measure to deal with B-spline MR and US registration. This method showed robustness against signal nonstationarity and intensity distortions and yielded insightful results for image-guided neurosurgery.

Fuerst et al. proposed in [FWMN14] another similarity measure to deal with MR and US registration. A linear correlation of linear combination (LC^2) was first designed to register the US image and a CT scan [WBK$^+$08]. Fuerst et al. adapted this idea to MR-US registration. They assumed that the US intensity is either correlated with the MR intensity or with the gradient of MR which leads to a first order polynomial function that relates the US image to the MR image and its gradient. A free-form deformation based on cubic B-splines was used to build the transformation between the two images. This technique showed some accurate results for image guided neurosurgery using 14 clinical cases.

3.4.2 Feature-based methods

The registration of MR and US images using feature-based methods can be very accurate, easy to implement and not expensive. This kind of registration generally relies on data reduction performed by an expert and segmentation. However, if MR image can be automatically segmented and features can be easily extracted from these images, it is more difficult for US images because they are highly contaminated by speckle noise. Thus, generating an automatic feature-based registration of MR/US images is very difficult.

Singh et al. proposed in [SKX+08] a manual registration method for real-time transrectal ultrasonography (TRUS) and previously acquired MR image to guide prostate biopsies. The sequence of MR images was registered manually to the US using custom software for real-time navigation and feedback. However, this approach relies significantly on the pertinence of the choice of control points and their correspondence in both images. In order to decrease user interaction, automatic and semi-automatic methods were also presented in [KZW+12].

Kadoury et al. investigated in [KZW+12] an approach to rigidly register the preoperative MR and the intraoperative US to allow pertinent needle placement during the ablation of liver metastases. Their contribution consists of training a deformable model for unsupervised segmentation of the liver in the MR image and extracting automatically the liver boundaries from the US image. The registration was performed using a weighted ICP algorithm with internal energy as a penalization.

Yavariabdi et al. considered in [YSB+13] a variational approach to map endometrial implants from transvaginal ultrasound (TVUS) and MR images. Images were first segmented by experts. A novel variational one-step deformable ICP method was used to estimate the deformation. This variant of ICP was then used to compute the deformation field based on a curative transformation and also to establish point correspondences automatically. Thus, it allows one to decrease the expert error and the interaction time while selecting manually point correspondences.

Mitra et al. presented in [MOM+10] an automatic deformable method for MR and US registration for prostate biopsy. The deformation model was based on radial basis functions, more specificaly on a thin-plate spline TPS. One contribution was to estimate the spline knots using a triangulation technique with the axes of the segmented prostate in MR and TRUS images. The two images were segmented using the method of [GOM+10]. A Shepard interpolation was used to overcome interpolation artefacts caused by the inverse TPS transform.

3.4.3 Other approach

Atehortúa et al. presented in [AGS+20] a novel 3D multimodal registration strategy to fuse 3D real-time echocardiography images with cardiac cine MRI images. This alignment was performed in a saliency space, which was designed to maximize similarity between the two imaging modalities. This fusion improves the quality of the available information. The used method performs in two steps: temporal and spatial registrations. A temporal alignment was firstly achieved by non linearly matching pairs of correspondences between the two modalities using a dynamic time warping. A temporal registration was then carried out by applying nonrigid transformations in a common saliency space where normalized cross correlation between temporal pairs of salient volumes was maximized.

3.4.4 Conclusion

In our joint fusion and registration method presented in Chapter 5, we will consider a registration step in order to correct registration errors during the fusion process. We will adopt the intensity-based approach with a polynomial function f_c as a similarity measure. We choose this similarity measure because it is also used in the fusion process to match the pixel intensities from MR and US images. The adopted transformation model is composed of a global transformation based on an affine operator and a local transformation based on B-splines, since free form B-spline have been widely used for non-rigid MR/US registration.

3.5 Global Conclusions

Since there is, to our knowledge, no state-of-the-art method for the fusion of MR and US images, this chapter proposed basic survey of medical image fusion. We can note that medical image fusion is a hard task and the challenging part is to estimate the link relating medical images especially when using multiple modalities. Transforms or feature extraction may be used to overcome this challenge but they are limited and sensitive to the low SNR of input images.

The second part of this chapter presented the image registration framework and its components with a general survey on medical image registration . This chapter was concluded by a state-of-the-art on MR and US registration. Note that intensity-based and feature-based registration methods have their own limitations and challenges. Intensity-based methods require to find an appropriate similarity measure that links information in images whereas feature-based methods are operator-dependent and rely excessively on the pertinence of features extracted by medical experts . At this point, we would like to mention that the few automatic studies in MR/US feature-based registration cannot handle important deformation between the images to be registered.

CHAPTER 4

Fusion of MRI and US images

Part of this chapter has been adapted from the journal paper [EMVB$^+$20]

Contents

4.1 Introduction 77

4.2 MR/US fusion using a global polynomial function 78

4.2.1 A statistical model for the fusion of MRI and US images 78

4.2.2 Algorithm for MR/US fusion 83

4.2.3 Simulation results 89

4.3 MR/US images fusion using a patch-wise polynomial 109

4.3.1 Estimation of the polynomial functions f_p 109

4.3.2 Experimental results using a patch-wise polynomial function 110

4.4 Conclusion 114

4.1 Introduction

This chapter studies a new fusion method for MR and US images, based on two image formation models gathering the advantages and drawbacks of each modality. More precisely, the MR image formation model accounts for the low spatial resolution of the observed image using a standard linear model with blurring and downsampling operators. The US image formation model takes into consideration the high amount of speckle noise, which is assumed to be Rayleigh-distributed as in many works including [AB07a, GCS05a, GSP05]. Given the different physical phenomena involved in each imaging modality, we propose to model the correspondence between gray levels of MR and US images using a polynomial function. This polynomial model can be theoretically motivated by the Weierstrass approximation theorem, which states that any continuous function on a closed and bounded interval can be uniformly approximated on that interval by polynomials with any degree of accuracy [MS00]. A more practical reason for using this kind of relationship between MR and US images is its successfull application to MR and US image registration [RPMA01]. Another variant to link MRI and US images, based on a patch-wise polynomial model, is also presented. The non-linear cost function considered to solve the fusion problem is constructed using the observation models associated with the MR and US images and the polynomial transformation relating the two images. Its minimization is challenging and is handled by a proximal alternating linearized minimization (PALM) algorithm. The proposed image fusion method is evaluated on simulated data with available ground truth, and on experimental data acquired on a phantom with imaging characteristics close to endometriosis. Both qualitative and quantitative results show the interest of fusing MR and US images, compared to restoring independently the images with each modality.

The remainder of this chapter is organized as follows: Section 4.2 introduces the statistical models for MR and US image fusion including a non-linear relation between the two modalities. The different steps of the proposed MR/US image fusion algorithm are detailed. Results obtained on simulated data and on an experimental allow the performance of the proposed method to be evaluated. Section 4.3 proposes a patch-wise polynomial model to link MRI and ultrasound images and compares results with the global polynomial function of Section 4.2. Conclusions are reported in Section 4.4.

4.2 MR/US fusion using a global polynomial function

4.2.1 A statistical model for the fusion of MRI and US images

The image fusion model introduced in this section assumes that the MR and US images to be fused are aligned, i.e., there is no geometric distortion between them, which can be obtained after an appropriate pre-registration. Thus, the registration potentially required in practical applications (see Chapter 3, Section 3.4) is considered herein as a pre-processing step and the possible registration errors are ignored hereafter. Note that despite this hypothesis, the fusion task is challenging because the two imaging modalities have different resolutions and contrasts and are corrupted by different kinds of noise.

4.2.1.1 Observation models

As stated in Chapter 2, MRI has the advantage of acquiring images with a large field of view, at the expense of a relatively low spatial resolution. In contrast to MRI, depending on the choice of the central frequency of the probe, US imaging can offer well-resolved images. However, US images are contaminated by a high level of speckle noise and have a reduced field of view. Based on these observations, many existing works aimed at improving independently the quality of MR and US images. In the case of MRI, the loss of resolution is classically modelled by a downsampling operation and a low pass filter [SCW⁺15]. In US imaging, speckle noise is usually considered as additive when considering the log-compressed envelope mode (also called B-mode) with a log-Rayleigh distribution [KR05, TSP88a]. This study assumes that the US noise sequence is independent and identically distributed (i.i.d) as in [C⁺02, BNB03]. Note that modelling the spatial correlation of noise samples would increase the complexity of the fusion method and is left for future work. These observations lead to the following image formation models

$$\begin{aligned} \boldsymbol{y}_{\mathrm{m}} &= \boldsymbol{S}\boldsymbol{C}\boldsymbol{x}_{\mathrm{m}} + \boldsymbol{n}_{\mathrm{m}} \\ \boldsymbol{y}_{\mathrm{u}} &= \boldsymbol{x}_{\mathrm{u}} + \boldsymbol{n}_{\mathrm{u}} \end{aligned} \tag{4.1}$$

where $\boldsymbol{x}_{\mathrm{m}} \in \mathbb{R}^N$ is the non-observable high-resolution vectorized MR image, $\boldsymbol{y}_{\mathrm{m}} \in \mathbb{R}^M$ is the observed low-resolution vectorized MR image and $\boldsymbol{n}_{\mathrm{m}} \in \mathbb{R}^N$ is the independent and identically distributed (i.i.d.) noise vector corrupting the MR image, assumed to be Gaussian as in [GP95]. Note that $\boldsymbol{C} \in \mathbb{R}^{N\times N}$ is a block circulant with circulant blocks matrix modelling the blurring effect of the MRI by a point spread function (PSF) and that $\boldsymbol{S} \in \mathbb{R}^{M\times N}$ (with $N = s^2 M$) is a decimation operator with a decimation factor s. On the other hand, $\boldsymbol{y}_{\mathrm{u}} \in \mathbb{R}^N$ is the observed vectorized B-mode US image, $\boldsymbol{x}_{\mathrm{u}} \in \mathbb{R}^N$ is the noise-free vectorized US image and $\boldsymbol{n}_{\mathrm{u}} \in \mathbb{R}^N$ is an i.i.d. additive log-Rayleigh noise with localization parameter γ. Note that the speckle noise affecting US images is mainly caused by diffusion, i.e., by the constructive and destructive interferences between echoes originated by small (with respect to the US wavelength) point targets called scatterers. Note also that all the vectors in (4.1) are obtained by vectorizing the corresponding images using the lexicographical order. Finally, we assume that $\boldsymbol{x}_{\mathrm{m}}$ and $\boldsymbol{x}_{\mathrm{u}}$ have the same spatial sampling, which can be obtained in practical applications by adjusting the decimation factor d in the MRI model, so that pixels in the super-resolved MR and US images have the same size.

4.2.1.2 Relation between US and MR images

MR and US imaging systems exploit different physical phenomena. Consequently, when imaging the same tissues, even in the virtual case of a perfect acquisition (without noise) allowing $\boldsymbol{x}_{\mathrm{m}}$ and $\boldsymbol{x}_{\mathrm{u}}$ to be directly observable, these two systems would not provide the same measurements. Thus, images $\boldsymbol{x}_{\mathrm{m}}$ and $\boldsymbol{x}_{\mathrm{u}}$ in (4.1) are not equal, even if they correspond to the same tissue. For solving the fusion task, we propose to link these two images by a parametric model. More precisely, we adopt the model originally proposed in [RPMA01] for MR/US image registration. This model is motivated by the fact that US image formation is essentially based on the gradient of the acoustic impedance between neighbouring tissues and is thus able to highlight the interfaces between anatomical structures. For US imaging, US waves (short pulses) are transmitted by the transducer, propagate through the tissues, and return to the transducer as reflected echoes. The reflected echoes correspond to US wave reflection at the interfaces between tissues with different acoustic impedances. Thus, the most important features in US images correspond to regions with gradient of impedance. The noise-free US envelope image (after amplitude demodulation of beamformed RF signals) can be expressed as

$$\boldsymbol{a}_{\boldsymbol{u}} = \nabla \boldsymbol{Z}^{H} \boldsymbol{u} \tag{4.2}$$

where $\boldsymbol{a}_{\boldsymbol{u}}$ is the speckle-free US envelope image, $\boldsymbol{Z}$ is the acoustic impedance map, $\boldsymbol{u}$ is the scan direction, ^{H} stands for Hermitian transpose and ∇ is the discrete gradient operator. The B-mode or log envelop of $\boldsymbol{a}_{\boldsymbol{u}}$, denoted by $\boldsymbol{x}_{\boldsymbol{u}}$ in (4.1) is

$$\boldsymbol{x}_{\boldsymbol{u}} = b \log[\nabla \boldsymbol{Z}^{H} \boldsymbol{u}] + g \tag{4.3}$$

where b and g are linear gains.

Exploiting the previous US image model relating US and MR pixel amplitudes turns out to finding a relationship between the MRI amplitude and the acoustic impedance $\boldsymbol{Z}$, denoted by ϕ such that

$$\boldsymbol{Z} = \phi[\boldsymbol{x}_{\mathrm{m}}]. \tag{4.4}$$

Computing the gradient of (4.4) leads to

$$\nabla \boldsymbol{Z} = \phi'[\boldsymbol{x}_{\mathrm{m}}]\nabla \boldsymbol{x}_{\mathrm{m}} \tag{4.5}$$

where ϕ' is the derivative of the unknown function ϕ. By plugging (4.5) into (4.3), the following relation between the US and MR images is obtained

$$\boldsymbol{x}_{\boldsymbol{u}} = b \log\left[\phi'(\boldsymbol{x}_{\mathrm{m}})\nabla \boldsymbol{x}_{\mathrm{m}}^{H}\boldsymbol{u}\right] + g \tag{4.6}$$

where b and g are constants. Note that the amplitude of one pixel in $\boldsymbol{x}_{\boldsymbol{u}}$ not only depends on the value of its counterpart in $\boldsymbol{x}_{\mathrm{m}}$, but also on the gradient of the MR image. To simplify the notations, this functional mapping between the US and MR images is defined as

$$\boldsymbol{x}_{\boldsymbol{u}} = f(\boldsymbol{x}_{\mathrm{m}}, \nabla \boldsymbol{x}_{\mathrm{m}}^{H}\boldsymbol{u}) \tag{4.7}$$

where $f : \mathbb{R}^{\mathbb{N}} \times \mathbb{R}^{\mathbb{N}} \rightarrow \mathbb{R}^{\mathbb{N}}$ is an unknown function and $\nabla \boldsymbol{x}_{\mathrm{m}}^{H}\boldsymbol{u} \in \mathbb{R}^{\mathbb{N}}$ contains in its ith line the inner product between the ith local gradient $\boldsymbol{x}_{\mathrm{m}}$ and the US scan direction $\boldsymbol{u}$.

We propose in this thesis to approximate the unknown function f in (4.7) by a polynomial (as in [RPMA01]) such that

$$x_{\boldsymbol{u},i} = \sum_{p+q\leq d} c_{pq} x_{\mathrm{m},i}^{p} (\nabla \boldsymbol{x}_{\mathrm{m}}^{H}\boldsymbol{u})_{i}^{q} \tag{4.8}$$

where c_{pq} are the unknown polynomial coefficients, index i stands for the i^{th} coefficient of a vector and d is the degree of the polynomial.

Remark 1. *For simplicity, one might consider that the unknown function f can be approximated by a linear function that links directly the US image to the MRI and the gradient of MRI (see [MBV+19]). However, due to the complex relation between MRI and US gray-level intensities, a linear function is not sufficient to model this relationship.*

4.2.1.3 A Bayesian approach for MR and US image fusion

Using the relationship between MR and US images in (4.7), the image formation models in (4.1) can be rewritten as

$$\begin{aligned} \boldsymbol{y}_{\mathrm{m}} &= \boldsymbol{S}\boldsymbol{C}\boldsymbol{x} + \boldsymbol{n}_{\mathrm{m}} \\ \boldsymbol{y}_{\mathrm{u}} &= f(\boldsymbol{x}, \nabla \boldsymbol{x}^{H}\boldsymbol{u}) + \boldsymbol{n}_{\mathrm{u}} \end{aligned} \tag{4.9}$$

where $\boldsymbol{x} \in \mathbb{R}^N$ is the unknown image to be estimated, containing relevant information from both MR and US data. The conditional distributions of $\boldsymbol{y}_\mathrm{m}$ and $\boldsymbol{y}_\mathrm{u}$ can be determined using the noise distributions

$$\begin{aligned} \boldsymbol{y}_\mathrm{m}|\boldsymbol{x} &\sim \mathcal{N}(\boldsymbol{S}\boldsymbol{C}\boldsymbol{x}, \sigma_m^2 \boldsymbol{I}_N) \\ \boldsymbol{y}_\mathrm{u}|\boldsymbol{x} &\sim \mathcal{LR}(\gamma) \end{aligned} \tag{4.10}$$

where $\mathcal{N}(\boldsymbol{\mu}, \boldsymbol{\Sigma})$ denotes the normal distribution with mean vector $\boldsymbol{\mu}$ and covariance matrix $\boldsymbol{\Sigma}$, and $\mathcal{LR}(\gamma)$ is the log-Rayleigh distribution with parameter γ[1]. Using Bayes rule and the independence between the noise vectors $\boldsymbol{n}_\mathrm{m}$ and $\boldsymbol{n}_\mathrm{u}$, the posterior distribution of $\boldsymbol{x}$ can be computed

$$p(\boldsymbol{x}|\boldsymbol{y}_\mathrm{m}, \boldsymbol{y}_\mathrm{u}) \propto p(\boldsymbol{y}_\mathrm{m}|\boldsymbol{x}) p(\boldsymbol{y}_\mathrm{u}|\boldsymbol{x}) p(\boldsymbol{x}) \tag{4.11}$$

where $p(\boldsymbol{x})$ is the prior probability distribution of $\boldsymbol{x}$ and $\propto$ means "proportional to". Finally, the log-posterior distribution can be written as

$$\begin{aligned} -\log p(\boldsymbol{x}|\boldsymbol{y}_\mathrm{m}, \boldsymbol{y}_\mathrm{u}) = \mathrm{K} + \underbrace{\frac{1}{2}\|\boldsymbol{y}_\mathrm{m} - \boldsymbol{S}\boldsymbol{C}\boldsymbol{x}\|^2}_{\text{MRI data fidelity}} - \underbrace{\log\left[p(\boldsymbol{x})\right]}_{\text{regularization}} \\ + \underbrace{\sum_{i=1}^{N} \Big[\exp(y_{\mathrm{u},i} - f_i(\boldsymbol{x}, \nabla\boldsymbol{x}^H\boldsymbol{u})) - \gamma(y_{\mathrm{u},i} - f_i(\boldsymbol{x}, \nabla\boldsymbol{x}^H\boldsymbol{u}))\Big]}_{\text{US data fidelity}} \end{aligned} \tag{4.12}$$

where $y_{u,i}$ and $f_i(\boldsymbol{x}, \nabla\boldsymbol{x}^H\boldsymbol{u})$ are the ith components of $\boldsymbol{y_u}$ and $f(\boldsymbol{x}, \nabla\boldsymbol{x}^H\boldsymbol{u})$ and K is a constant.

Different prior distributions $p(\boldsymbol{x})$ have been considered in the literature to solve ill-posed problems. In this study, we propose to use the classical total variation (TV) promoting piece-wise constant fused images. Estimating $\boldsymbol{x}$ in the sense of the maximum *a posteriori* principle using this TV regularization leads to the following minimization problem

$$\begin{aligned} \hat{\boldsymbol{x}} = \underset{\boldsymbol{x}}{\operatorname{argmin}} \quad \frac{1}{2}\|\boldsymbol{y}_\mathrm{m} - \boldsymbol{S}\boldsymbol{C}\boldsymbol{x}\|^2 + \tau_1\|\nabla\boldsymbol{x}\|^2 + \tau_3\|\nabla f(\boldsymbol{x}, \nabla\boldsymbol{x}^H\boldsymbol{u})\|^2 + \\ \tau_2 \sum_{i=1}^{N} \Big[\exp(y_{\mathrm{u},i} - f_i(\boldsymbol{x}, \nabla\boldsymbol{x}^H\boldsymbol{u})) - \gamma(y_{\mathrm{u},i} - f_i(\boldsymbol{x}, \nabla\boldsymbol{x}^H\boldsymbol{u}))\Big] \end{aligned} \tag{4.13}$$

---

[1] The probability density function (pdf) of a variable distributed according to a log-Rayleigh distribution denoted as $z \sim \mathcal{LR}(\gamma)$ is $p(z) = \frac{(e^z)^2}{\gamma} \exp\left[-\frac{(e^z)^2}{2\gamma}\right] \mathbb{I}_{\mathbb{R}^+}(z)$, where $\mathbb{I}_{\mathbb{R}^+}$ is the indicator on $\mathbb{R}^+$.

where τ_1, τ_3 and τ_2 are hyperparameters balancing the weights of the data fidelity and TV regularization terms. Note that the cost function in (4.13) depends on the polynomial parameters c_{pq} relating US and MR pixel amplitudes, that need to be estimated before solving (4.13).

4.2.2 Algorithm for MR/US fusion

This section studies an optimization algorithm dedicated to solve (4.13). The presence of the non-linear polynomial function f in (4.13) prevents the use of algorithms based on the alternate direction method of multipliers (ADMM) [BPC+11] (as in [MBV+19]). Consequently, we propose hereafter an algorithm based on the proximal alternating linearized minimization (PALM), adapted to nonconvex and nonsmooth functions [BST14].

4.2.2.1 PALM summary

The PALM algorithm was originally designed to minimize functions of two vectors $\boldsymbol{x}$ and $\boldsymbol{v}$ that can be decomposed as

$$\min_{\boldsymbol{x},\boldsymbol{v}} \psi(\boldsymbol{x},\boldsymbol{v}) := l(\boldsymbol{x}) + g(\boldsymbol{v}) + H(\boldsymbol{x},\boldsymbol{v}) \tag{4.14}$$

where l and g are continuous convex functions and H may be non-linear. Moreover, these three functions must respect the following conditions to fit the PALM framework [BST14]

1. l and g are inf-bounded ($\inf_{\mathbb{R}^N}(f) > -\infty$ and $\inf_{\mathbb{R}^N}(g) > -\infty$).
2. For any fixed $\boldsymbol{v}$, the function $\boldsymbol{x} \mapsto H(\boldsymbol{x},\boldsymbol{v})$ is $C^{1,1}$, and the partial gradient $\nabla_{\boldsymbol{x}} H(\boldsymbol{x},\boldsymbol{v})$ is globally Lipschitz.
3. For any fixed $\boldsymbol{x}$, the function $\boldsymbol{v} \mapsto H(\boldsymbol{x},\boldsymbol{v})$ is $C^{1,1}$, and the partial gradient $\nabla_{\boldsymbol{v}} H(\boldsymbol{x},\boldsymbol{v})$ is globally Lipschitz.
4. ∇H is Lipschitz continuous on bounded subsets of the image domain.

PALM can be viewed as a minimization of the sum of the two functions l and g with a linearization of H around a given point $\boldsymbol{x}^k$. The alternate minimization with respect to the two blocks $\boldsymbol{x}$ and $\boldsymbol{v}$ proposed in [BST14] generates a sequence $\{(\boldsymbol{x}^k, \boldsymbol{v}^k)\}_{k\in\mathbb{N}}$ using the following steps

Step 1: Choose $\gamma_1 > 1$, set $c_k = \gamma_1 L_{\boldsymbol{x}}(\boldsymbol{v}^k)$ and update $\boldsymbol{x}^k$ as follows

$$\begin{aligned}\boldsymbol{x}^{k+1} &= \text{prox}^l_{c_k}\Big(\boldsymbol{x}^k - \frac{1}{c_k}\nabla_{\boldsymbol{x}} H(\boldsymbol{x}^k, \boldsymbol{v}^k)\Big)\\ &= \underset{\boldsymbol{x}}{\text{argmin}}(\boldsymbol{x} - \boldsymbol{x}^k)^H \nabla_{\boldsymbol{x}} H(\boldsymbol{x}^k, \boldsymbol{v}^k) + \frac{c_k}{2}\|\boldsymbol{x} - \boldsymbol{x}^k\|^2 + l(\boldsymbol{x})\end{aligned}$$

where $L_{\boldsymbol{x}}(\boldsymbol{v}^k)$ is the Lipschitz constant of $\boldsymbol{x} \mapsto \nabla_{\boldsymbol{x}} H(\boldsymbol{x}, \boldsymbol{v}^k)$ and $\boldsymbol{v}^k$ is the value of $\boldsymbol{v}$ at iteration $\#k$.

Step 2 : Choose $\gamma_2 > 1$, set $d_k = \gamma_2 L_{\boldsymbol{v}}(\boldsymbol{x}^k)$ and update $\boldsymbol{v}^k$ as folllows

$$\begin{aligned}\boldsymbol{v}^{k+1} &= \text{prox}^g_{d_k}\Big(\boldsymbol{v}^k - \frac{1}{d_k}\nabla_{\boldsymbol{v}} H(\boldsymbol{x}^k, \boldsymbol{v}^k)\Big)\\ &= \underset{\boldsymbol{v}}{\text{argmin}}(\boldsymbol{v} - \boldsymbol{v}^k)^H \nabla_{\boldsymbol{v}} H(\boldsymbol{x}^k, \boldsymbol{v}^k) + \frac{d_k}{2}\|\boldsymbol{v} - \boldsymbol{v}^k\|^2 + g(\boldsymbol{v})\end{aligned}$$

where $L_{\boldsymbol{v}}(\boldsymbol{x}^k)$ is the Lipschitz constant of $\boldsymbol{v} \mapsto \nabla_{\boldsymbol{v}} H(\boldsymbol{x}^k, \boldsymbol{v})$ and $\boldsymbol{x}^k$ is the value of $\boldsymbol{x}$ at iteration $\#k$.

Note that this iterative scheme requires to compute the Lipschitz constants $L_{\boldsymbol{x}}(\boldsymbol{v}^k)$ and $L_{\boldsymbol{v}}(\boldsymbol{x}^k)$.

4.2.2.2 PALM for MR/US fusion

In order to respect the constraints mentioned above and to adapt our image fusion minimization problem to the PALM framework, we propose the following parametrization

$$l(\boldsymbol{x}) = \frac{1}{2}\|\boldsymbol{y}_{\text{m}} - \boldsymbol{S}\boldsymbol{C}\boldsymbol{x}\|_2^2 + \tau_1\|\nabla\boldsymbol{x}\|^2 \tag{4.15}$$

$$g(\boldsymbol{v}) = \tau_2\sum_i[\exp(y_{\text{u},i} - v_i) - \gamma(y_{\text{u},i} - v_i)] + \tau_3\|\nabla\boldsymbol{v}\|^2 \tag{4.16}$$

$$H(\boldsymbol{x}, \boldsymbol{v}) = \tau_4\sum_{i=1}^{N}\Big(v_i - \sum_{p+q\leq 3} c_{pq} x_i^p (\nabla\boldsymbol{x}^H\boldsymbol{u})_i^q\Big) \tag{4.17}$$

where

$$\boldsymbol{v} = f(\boldsymbol{x}, \nabla\boldsymbol{x}^H\boldsymbol{u}).$$

Remark 2. *With this choice of functions l, g and h, the four assumptions stated previously are satisfied, as explained hereafter.*

1. Assumption 1 ensures that the PALM algorithm is well defined, which can be easily verified in our case.
2. Assumptions 2 and 3: Since $\boldsymbol{x} \mapsto \nabla_{\boldsymbol{x}} H(\boldsymbol{x}, \boldsymbol{v})$ and $\boldsymbol{v} \mapsto \nabla_{\boldsymbol{v}} H(\boldsymbol{x}, \boldsymbol{v})$ are polynomial functions, they are globally Lipschitz and their domains are bounded.
3. Since H is C^2, Assumption 4 is satisfied as a consequence of the mean value theorem.

We denote hereafter by $\{(\boldsymbol{x}^k, \boldsymbol{v}^k)\}_{k\in\mathbb{N}}$ the sequence generated by the PALM algorithm.

4.2.2.3 Lipschitz constants

Before going into the details of the PALM algorithm used to solve Problem (4.14), this section explains how the Lipschitz constants $L_{\boldsymbol{x}}(\boldsymbol{v})$ and $L_{\boldsymbol{v}}(\boldsymbol{x})$ of $\boldsymbol{x} \mapsto \nabla_{\boldsymbol{x}} H(\boldsymbol{x}, \boldsymbol{v})$ and $\boldsymbol{v} \mapsto \nabla_{\boldsymbol{v}} H(\boldsymbol{x}, \boldsymbol{v})$ can be computed. Eq. (4.17) leads to

$$\nabla_{\boldsymbol{v}} H(\boldsymbol{x}, \boldsymbol{v}) = 2\tau_4 \Big(\boldsymbol{v} - \sum_{p+q\leq 3} c_{pq} \boldsymbol{x}^p (\nabla \boldsymbol{x}^H \boldsymbol{u})^q \Big). \tag{4.18}$$

The computation of the Lipschitz constant [1] $L_{\boldsymbol{v}}(\boldsymbol{x})$ is straightforward and leads to $L_{\boldsymbol{v}}(\boldsymbol{x}) = 2\tau_4, \ \forall \boldsymbol{x}$. The Lipschitz constant of $\boldsymbol{x} \mapsto \nabla_{\boldsymbol{x}} H(\boldsymbol{x}, \boldsymbol{v})$ is more complicated to evaluate. We therefore use PALM with a backtracking stepsize rule as suggested in [BT09]. Note that one of the pillars of PALM's convergence proof is the following lemma for smooth functions.

Lemma 1. *Let $h : \mathbb{R}^n \to \mathbb{R}$ be a continuously differentiable function with Lipschitz continuous gradient and Lipschitz constant L_h. Then for any $L \geq L_h$ and $\forall \boldsymbol{x}, \boldsymbol{y} \in \mathbb{R}^n$*

$$h(\boldsymbol{x}) \leq h(\boldsymbol{y}) + (\boldsymbol{x} - \boldsymbol{y})^H \nabla_{\boldsymbol{x}} h(\boldsymbol{x}) + \frac{L}{2} \|\boldsymbol{x} - \boldsymbol{y}\|_2^2. \tag{4.19}$$

---

[1] For function $f : \mathbb{R}^n \mapsto \mathbb{R}$, Lipschitz constant denotes the smallest constant $M > 0$ in the Lipschitz condition, namely the nonnegative number

$$\sup_{\boldsymbol{x}\neq \boldsymbol{y}} \frac{|f(\boldsymbol{x}) - f(\boldsymbol{y})|}{\|\boldsymbol{x} - \boldsymbol{y}\|}$$

where $\|.\|$ is the associated norm to the Euclidean space.

Using simple algebra, one can show that the function ψ defined in (4.14) satisfies the following relation

$$\psi(\boldsymbol{x}, \boldsymbol{v}) \leq Q_L(\boldsymbol{x}, \boldsymbol{y}, \boldsymbol{v}) \tag{4.20}$$

where

$$Q_L(\boldsymbol{x}, \boldsymbol{y}, \boldsymbol{v}) = l(\boldsymbol{x}) + g(\boldsymbol{v}) + H(\boldsymbol{y}, \boldsymbol{v}) + (\boldsymbol{x} - \boldsymbol{y})^H \nabla_{\boldsymbol{x}} H(\boldsymbol{y}, \boldsymbol{v}) + \frac{L}{2}\|\boldsymbol{x} - \boldsymbol{y}\|^2.$$

In order to ensure the convergence of the PALM algorithm, the backtracking rule consists of verifying that the inequality (4.20) is satisfied at every step. To estimate the Lipschitz constant, at each iteration k, we search for the smallest nonnegative integers i_k such that $L_{k+1} = \lambda^{i_k} L_k$ verifies

$$\psi(p_{\bar{L}}(\boldsymbol{x}^k), \boldsymbol{v}^k) \leq Q_{\bar{L}}(p_{\bar{L}}(\boldsymbol{x}^k), \boldsymbol{x}^k, \boldsymbol{v}^k)$$

with

$$p_{\bar{L}}(\boldsymbol{x}^k) = \operatorname{prox}^l_{L_{k+1}}\left(\boldsymbol{x}^k - \frac{1}{L_{k+1}} \nabla_{\boldsymbol{x}} H(\boldsymbol{x}^k, \boldsymbol{v}^k)\right).$$

Remark 3. *The sequence of values $\psi(\boldsymbol{x}^k, \boldsymbol{v}^k)$ computed by PALM is decreasing for all $\boldsymbol{x}^k$ and $\boldsymbol{v}^k$. The proof is straightforward. For every $k \geq 1$*

$$\psi(\boldsymbol{x}^{k+1}, \boldsymbol{v}^k) \leq Q_{L_{k+1}}(\boldsymbol{x}^{k+1}, \boldsymbol{x}^k, \boldsymbol{v}^k)$$

and

$$Q_{L_{k+1}}(\boldsymbol{x}^{k+1}, \boldsymbol{x}^k, \boldsymbol{v}^k) \leq Q_{L_{k+1}}(\boldsymbol{x}^k, \boldsymbol{x}^k, \boldsymbol{v}^k) = \psi(\boldsymbol{x}^k, \boldsymbol{v}^k).$$

Thus

$$\psi(\boldsymbol{x}^{k+1}, \boldsymbol{v}^k) \leq \psi(\boldsymbol{x}^k, \boldsymbol{v}^k)$$

and

$$\psi(\boldsymbol{x}^k, \boldsymbol{v}^{k+1}) \leq \psi(\boldsymbol{x}^k, \boldsymbol{v}^k)$$

which concludes the proof.

Remark 4. *Since inequality (4.20) is satisfied for $L \geq L_{\boldsymbol{x}}(\boldsymbol{v}), \forall \boldsymbol{v}$, where $L_{\boldsymbol{x}}(\boldsymbol{v})$ is the Lipschitz constant of $x \to \nabla_{\boldsymbol{x}} H(\boldsymbol{x}, \boldsymbol{v})$, the following inequalities can be obtained*

$$L_{\boldsymbol{x}}(\boldsymbol{v}^k) \leq L_{k+1} \leq \lambda L_H(\boldsymbol{v}^k). \tag{4.21}$$

Note that the inequality $L_{\boldsymbol{x}}(\boldsymbol{v}^k) \leq L_{k+1}$ is sufficient to ensure the convergence of PALM. However, the second inequality $L_{k+1} \leq \lambda L_H(\boldsymbol{v}^k)$ allows the convergence rate to be controlled by an appropriate choice of λ.

In the following subsections, the updates of each variable within PALM algorithm are described in details.

4.2.2.4 Update of $\boldsymbol{x}$

The update of $\boldsymbol{x}$ is achieved by minimizing the sum of quadratic functions, leading to

$$\begin{aligned}\boldsymbol{x}^{k+1} &= \mathrm{prox}^{l}_{L_{k+1}}\left(\boldsymbol{x}^k - \frac{1}{L_{k+1}}\nabla_{\boldsymbol{x}} H(\boldsymbol{x}^k, \boldsymbol{v}^k)\right)\\ &= \underset{\boldsymbol{x}}{\mathrm{argmin}} \quad \frac{1}{2}\|\boldsymbol{SCx} - \boldsymbol{y}_{\mathrm{m}}\|^2 + \tau_1\|\nabla \boldsymbol{x}\|^2 + \frac{L_{k+1}}{2}\|\boldsymbol{x} - (\boldsymbol{x}^k - \frac{1}{L_{k+1}}\nabla_{\boldsymbol{x}} H(\boldsymbol{x}^k, \boldsymbol{v}^k))\|^2\end{aligned}$$

where l is defined in (4.15) and L_{k+1} is the Lipschitz constant at iteration $k+1$. This minimization problem admits an analytical solution, which can be computed efficiently in the Fourier domain. The practical tractability of this solution is possible for large images using the decomposition of the decimation matrix $\boldsymbol{S}$ proposed in [ZWB+16b], since the convolution operator is diagonalizable in the Fourier domain. The update of $\boldsymbol{x}$ at the $(k+1)$th iteration is then obtained as follows

$$\boldsymbol{x}^{k+1} = \left[\boldsymbol{C}^H\boldsymbol{S}^H\boldsymbol{SC} + 2\left(\tau_1\boldsymbol{D} + \frac{L_{k+1}}{2}\mathbb{I}_N\right)\right]^{-1}\boldsymbol{R} \tag{4.22}$$

with

$$\boldsymbol{R} = \boldsymbol{C}^H\boldsymbol{S}^H y_{\mathrm{m}} + 2L_{k+1}\left(\boldsymbol{x}^k - \frac{1}{L_{k+1}}\nabla_{\boldsymbol{x}} H(\boldsymbol{x}^k, \boldsymbol{v}^k)\right)$$
$$\boldsymbol{D} = \boldsymbol{D}_h^H\boldsymbol{D}_h + \boldsymbol{D}_{\boldsymbol{v}}^H\boldsymbol{D}_{\boldsymbol{v}}$$

where $\boldsymbol{D}_h$ and $\boldsymbol{D}_{\boldsymbol{v}}$ are the horizontal and vertical finite difference operators.

The direct computation of the solution (4.22) requires the inversion of high dimensional matrices. To overcome this problem, we adopt herein the solution proposed in [ZWB+16b], which is recalled hereafter. Based on the circulant boundary conditions, the blurring matrix $\boldsymbol{C}$ is a block circulant with circulant blocks matrix (BCCB) that can be decomposed as

$$\boldsymbol{C} = \boldsymbol{F}^H\boldsymbol{\Lambda}\boldsymbol{F}$$

where $\boldsymbol{F}$ and $\boldsymbol{F^H}$ are 2D Fourier and 2D inverse Fourier operators, $\boldsymbol{\Lambda} = \text{diag}(\boldsymbol{F}\boldsymbol{h})$, with $\boldsymbol{h}$ the first column of the matrix $\boldsymbol{C}$. Taking into account this property and using the Woodbury inverse formula [ZWB$^+$16b], the update of $\boldsymbol{x}$ can be rewritten as

$$\boldsymbol{x}^{k+1} = \frac{1}{\tau_1 L_{k+1}} \boldsymbol{F}^H \boldsymbol{\psi} \boldsymbol{F} \boldsymbol{r} - \frac{1}{\tau_1 L_{k+1}} \boldsymbol{F}^H \boldsymbol{\psi} \underline{\boldsymbol{\Lambda}}^H (2\tau_1 s \mathbb{I}_N + \underline{\boldsymbol{\Lambda}} \boldsymbol{\psi} \underline{\boldsymbol{\Lambda}}^H)^{-1} \underline{\boldsymbol{\Lambda}} \boldsymbol{\psi} \boldsymbol{F} \boldsymbol{r} \tag{4.23}$$

where

$$\boldsymbol{r} = \boldsymbol{C}^H \boldsymbol{S}^H \boldsymbol{y}_{\text{m}} + L_{k+1} \left(\boldsymbol{x}^k - \frac{1}{L_{k+1}} \nabla_{\boldsymbol{x}} H(\boldsymbol{x}^k, \boldsymbol{v}^k) \right)$$

and the matrix $\underline{\boldsymbol{\Lambda}}$ is a block diagonal matrix denoted as

$$\underline{\boldsymbol{\Lambda}} = [\boldsymbol{\Lambda}_1, ..., \boldsymbol{\Lambda}_d]$$

where the blocks $\boldsymbol{\Lambda_i}$ are the diagonal matrices of $\boldsymbol{\Lambda}$, and where

$$\boldsymbol{\psi} = \boldsymbol{F}(\tau_1(\boldsymbol{D}_h^H \boldsymbol{D}_h + \boldsymbol{D}_{\boldsymbol{v}}^H \boldsymbol{D}_{\boldsymbol{v}}) + \frac{L_{k+1}}{2} \mathbb{I}_N)^{-1} \boldsymbol{F}^H.$$

4.2.2.5 Update of $\boldsymbol{v}$

The vector $\boldsymbol{v}$ is updated using a gradient descent algorithm with backtracking line search, given that the function to minimize in this step is differentiable and convex. More precisely, the following update has ben considered

$$\begin{aligned} \boldsymbol{v}^{k+1} &= \underset{\boldsymbol{v}}{\text{argmin}} \quad \tau_2 \sum_i [\exp(y_{\text{u},i} - v_i) - \gamma(y_{\text{u},i} - v_i)] \\ &+ \tau_3 \|\nabla \boldsymbol{v}\|^2 + \frac{d_k}{2} \|\boldsymbol{v} - (\boldsymbol{v}^k - \frac{1}{d_k} \nabla_{\boldsymbol{v}} H(\boldsymbol{x}^{k+1}, \boldsymbol{v}^k))\|^2 \\ &= \text{prox}_{d_k}^g \left(\boldsymbol{v}^k - \frac{1}{d_k} \nabla_{\boldsymbol{v}} H(\boldsymbol{x}^{k+1}, \boldsymbol{v}^k) \right) \end{aligned} \tag{4.24}$$

where g is defined in (4.16) and $d_k = L_{\boldsymbol{v}}(\boldsymbol{x}^k)$ is the Lipschitz constant of $\nabla_{\boldsymbol{v}} H$ at iteration k.

4.2.2.6 Estimation of the global polynomial function

For a given order d, the unknown polynomial function f relating $\boldsymbol{x}_{\mathrm{m}}$ to $\boldsymbol{x}_{\mathrm{u}}$ is defined by $N_d = (d+1)(d+2)/2$ coefficients gathered in the vector $\boldsymbol{c}_d = \{c_{pq} \mid p+q \leq d\}$. To estimate these coefficients, we assume that the observed MR and US images are related as follows

$$y_{\mathrm{u},i} = \sum_{p+q\leq 3} c_{pq} y_{\mathrm{m},i}^{p} (\nabla y_{\mathrm{m}}^{H} u)_i^q + \epsilon_i \quad i = 1, ..., N$$

or equivalently, in algebraic form

$$\boldsymbol{y}_{\mathrm{u}} = \boldsymbol{A}_m \boldsymbol{c}_d + \boldsymbol{\epsilon} \tag{4.25}$$

where $\boldsymbol{A}_m \in \mathbb{R}^{N\times N_d}$ is a matrix whose elements are $y_{\mathrm{m},i}^{p} (\nabla y_{\mathrm{m}}^{H} u)_i^q$ for $p+q \leq d$ and $\boldsymbol{\epsilon} = (\epsilon_1, ..., \epsilon_N)^T$.

The least-squares estimator of $\boldsymbol{c}_d$ (which is also the maximum likelihood estimator for i.i.d. Gaussian errors ϵ_i) is defined by

$$\hat{\boldsymbol{c}}_d = \boldsymbol{A}_m^{\dagger} \boldsymbol{y}_u \tag{4.26}$$

where $\boldsymbol{A}_m^{\dagger} = (\boldsymbol{A}_m^T \boldsymbol{A}_m)^{-1} \boldsymbol{A}_m^T$ is the pseudo-inverse of the matrix $\boldsymbol{A}_m$. This estimator will be used to estimate the coefficients of the polynomial function f in our experiments.

4.2.2.7 Algorithm summary

Algo. 1 summarizes all the steps of the proposed MR/US image fusion method.

4.2.3 Simulation results

4.2.3.1 Simulation setup

This section demonstrates the efficiency of the proposed MRI/US fusion method using two sets of synthetic images with controlled ground truth. The observed MR images were generated from the high resolution MR images displayed in Figs. 4.1(a) and 4.2(a), after blurring, decimation and contamination by an additive i.i.d. white Gaussian noise leading to Figs. 4.1(c) and 4.2(c). The blurring kernel was a 2D Gaussian filter of size 9 × 9 with variance $\sigma_m^2 = 4$. The decimation factors were set to $s = 4$ for the first dataset and $s = 2$ for the second dataset. A Gaussian noise was finally

```
Algorithm 1: Proposed MR/US image fusion algorithm.
    Input $\boldsymbol{y_u}$, $\boldsymbol{y_m}$, $\boldsymbol{S}$, $\boldsymbol{C}$, $\tau$, $\lambda$, $\mu$
    0 - Estimate the polynomial function $f$ (see Section 4.2.2.6)
    REPEAT
    1 - Find the smallest nonnegative integers $i_k$ such that
            $\psi(p_{\bar{L}}(\boldsymbol{x^k}), \boldsymbol{v^k}) \leq Q_{\bar{L}}(p_{\bar{L}}(\boldsymbol{x^k}), \boldsymbol{x^k}, \boldsymbol{v^k})$
    with $\bar{L} = \gamma^{i_k} L_k$. Set $L_{k+1} = \gamma^{i_k} L_k$ and update $\boldsymbol{x}$ using (4.23)
    2 - Set $d_k = L_{\boldsymbol{v}}(\boldsymbol{x}^{k+1}) = 2\tau_4$ and update $v$ using (4.24)
    Until stopping criterion is satisfied
    Output: Fused image $\boldsymbol{x}$
```

added to the blurred and decimated MRI images with signal-to-noise ratios equal to SNR $= 23.26$ dB for the first image and SNR $= 20.73$ dB for the second image. Note that the sizes of the observed MR images were 64×64 and 75×75 for the two datasets. A third order polynomial ($d = 3$) was used to generate the clean US images from the corresponding clean high-resolution MR images, as shown in Figs. 4.1(b) and 4.2(b). To generate the observed US images, log-Rayleigh noise was added to the B-mode US images yielding the images displayed in Figs. 4.1(d) and 4.2(d). Note that the SNRs for the Rayleigh noise affecting the US images were SNR $= 13.72$ dB for the first dataset and SNR $= 13.80$ dB for the second dataset. A linear normalization was finally applied to the observed MRI and US images in order to have pixel values in the interval $(0, 1)$. It transforms a grayscale image with intensity values in the range $(\min, \max)$ into a new image with intensity values in the range $(0, 1)$ according to

$$\boldsymbol{I_n} = \frac{\boldsymbol{I} - \min(\boldsymbol{I})}{\max(\boldsymbol{I}) - \min(\boldsymbol{I})}$$

where $\boldsymbol{I}$ is the grayscale image and $\boldsymbol{I_n}$ is the normalized image. This normalization ensures that MRI and US pixels have a comparable gray level scale and has been used successfully in many application such as [Chr03].

4.2.3.2 Performance evaluation

The performance of the proposed fusion algorithm was evaluated for synthetic data using four quantitative metrics: the root mean square error (RMSE), the peak signal to noise ratio (PSNR), the improved signal-to-noise ratio (ISNR) and the mean structural similarity (MSSIM) [HZ10]. These metrics are defined explicitely in (4.27), where $\boldsymbol{x}$ denotes the ground truth image, $\hat{\boldsymbol{x}}$ is the estimated image and $\underline{\boldsymbol{y}}$ is the bicubic interpolated MR image:

$$\begin{aligned}
\text{RMSE} &= \sqrt{\frac{1}{N}\|\hat{\boldsymbol{x}} - \boldsymbol{x}\|_2^2} \\
\text{PSNR} &= 20\log_{10}\frac{\max(\hat{\boldsymbol{x}}, \boldsymbol{x})}{\text{RMSE}} \\
\text{ISNR} &= 10\log_{10}\frac{\|\underline{\boldsymbol{y}} - \boldsymbol{x}\|}{\|\hat{\boldsymbol{x}} - \boldsymbol{x}\|^2} \\
\text{MSSIM} &= \frac{1}{M}\sum_{j=1}^{M}\text{SSIM}(\boldsymbol{x}_j, \hat{\boldsymbol{x}}_j).
\end{aligned} \tag{4.27}$$

The metric MSSIM is implemented blockwise, where M is the number of local windows, $\hat{\boldsymbol{x}}_j$ and $\boldsymbol{x}_\mathrm{j}$ are local regions extracted from $\hat{\boldsymbol{x}}$ and $\boldsymbol{x}$ and SSIM is the structural similarity index computed for each window as in [WBSS04]. Note that the different metrics were computed using the fused image and the US and MRI ground truth images. The proposed algorithm was compared to two existing image restoration algorithms:

- An MR restoration algorithm proposed in [ZWB+16b] to estimate a high-resolution MR image from the observed low resolution MR image.
- A denoising algorithm adapted to US images proposed in [GSA16].

4.2.3.3 Simulation results

The fused images obtained using the proposed algorithm are displayed in Figs. 4.1(g) and 4.2(g). The first interesting result is that for both datasets, the fused image contains information from both MR and US modalities in an enhanced image compared to the two observed MRI and US images. The fused images are compared visually in Figs. 4.1 and 4.2 to the despeckled US image

(a) Ground truth MRI (b) Ground truth US (c) MRI observation

(d) US observation (e) Estimated HR MR image (f) Despeckeled US image

(g) Fused image

Figure 4.1: US and MRI fusion: (a) True high resolution MR image, (b) Simulated US image using a polynomial function applied to the MR image (a), (c) MR low-resolution and blurred image, (d) noisy US image, (e) high resolution MR image estimated using the fast super resolution algorithm of [ZWB$^+$16b], (f) despeckled US image using TV regularization, (g) fused image obtained with Algo 1.

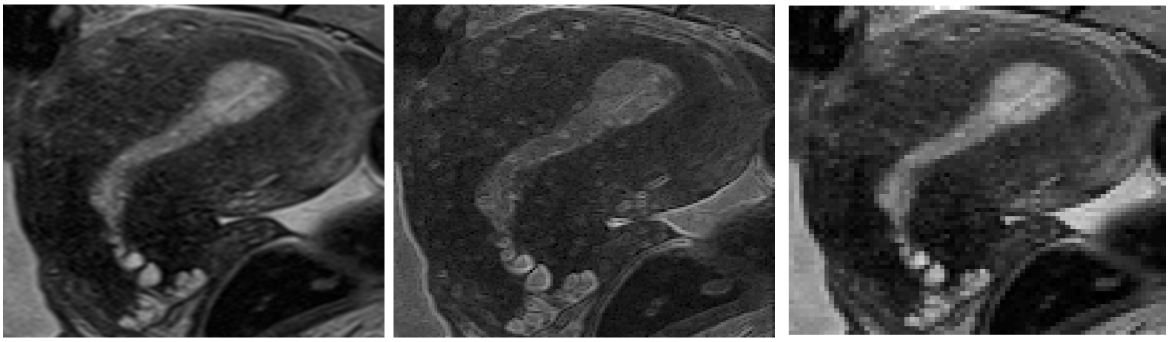

(a) Ground truth MRI (b) Ground truth US (c) MRI observation

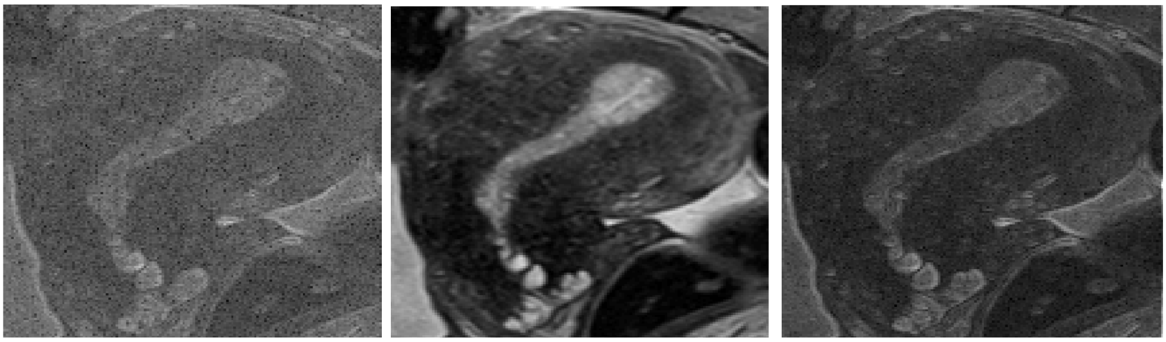

(d) US observation (e) Estimated HR MR image (f) Despeckeled US image

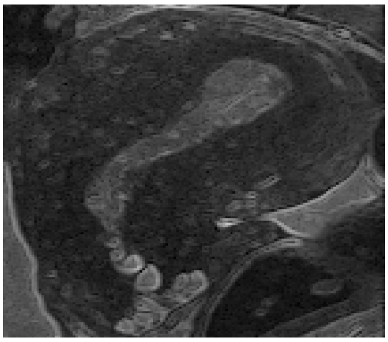

(g) Fused image

Figure 4.2: US and MRI fusion: (a) True high resolution MR image, (b) Simulated US image using a polynomial function applied to the MR image in (a), (c) MR low-resolution and blurred image, (d) noisy US image, (e) high resolution MR image estimated using the fast super resolution algorithm in [ZWB+16b], (f) despeckled US image using TV regularization, (g) fused image obtained with Algo 1.

(obtained by solving the denoising problem using a gradient descent algorithm, with a log-Rayleigh noise hypothesis and TV regularization) and to the super-resolved (SR) MR image obtained using the algorithm in [ZWB+16b] (that accounts for Gaussian noise and TV regularization). The quantitative results reported in Table 4.1 confirm the interest of fusing images of two different modalities, when compared to the images restored from each imaging modality separately. Considering MR and US data jointly allows both spatial resolution and image contrast to be enhanced.

Table 4.1: Quantitative results on simulated data.

	Dataset 1 (Fig. 4.1)			
	Fused image vs MRI	SR MRI	Fused image vs US	Despeckeled US
RMSE	0.060	0.081	0.18	0.29
PSNR [dB]	24.37	21.08	15.78	10.67
ISNR [dB]	5.25	2.11	4.1	0.98
MSSIM [dB]	0.70	0.69	0.68	0.64
	Dataset 2 (Fig. 4.2)			
	Fused image vs MRI	SR MRI	Fused image vs US	Despeckeled US
RMSE	0.052	0.071	0.3	0.37
PSNR [dB]	15.7	11.37	7.34	5.38
ISNR [dB]	4.25	1.98	3.01	1.29
MSSIM [dB]	0.74	0.61	0.58	0.24

4.2.3.4 Polyvinyl Alcohol Phantom

MRI experiments were performed using a 3T clinical imaging system (Philips Achieva dStream, Inserm/UPS UMR1214 ToNIC Technical Platform, Toulouse, France). Axial fat-suppressed T_1-weighted sequences (multishot mode, 4mm slice thickness, voxel matrix $4 \times 1 \times 4$ mm) and axial, sagittal and coronal T_2-weighted sequences (multishot mode, 2 mm slice thickness, voxel matrix $0.8 \times 2 \times 2$ mm) were acquired. For the image fusion, only the T_2-weighted image was used (see Table

4.2).

	Sagittal T2W	**Coronal T2W**
MRI observation	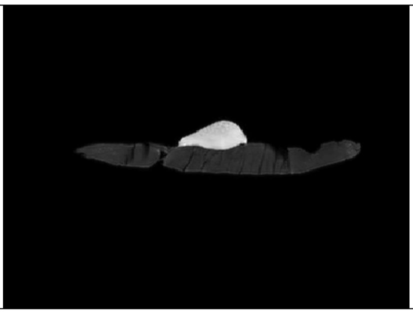	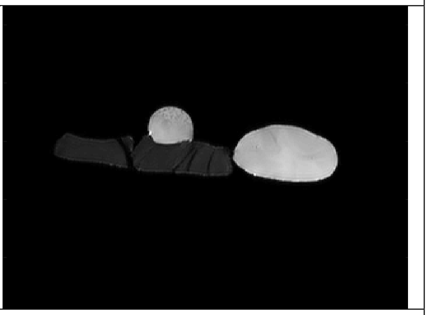
Voxel matrix(mm)	0.8 × 2 × 2	0.8 × 2 × 2
Matrix	320 × 320	320 × 320
Repetition time (ms)	4641	4843
Echo time (ms)	100	100
Section thickness (mm)	2	2
Acquisition time	1min45s	1min44s

Table 4.2: MRI protocol

For US image acquisition, the experimental model was immersed in a bucket full of water. A US examination was performed using a Voluson S9 system (General Electrics). All images were acquired with a 10-MHz linear array transducer (for more details see Appendix A).

In all the experiments below, the degree of the polynomial relating US and MR pixel intensities was set to $d = 4$, which implies that the number of coefficients in $\boldsymbol{c}_d$ is $N_d = 15$. This choice was motivated by our results on experimental data showing that $d = 4$ is the smallest degree ensuring a good fit between US and MR images, as highlighted in Fig. 4.3. The estimation of the vector $\boldsymbol{c}_d$ was considered in a preprocessing step using (4.26). Fig. 4.4 shows the effect of applying the estimated polynomial function onto one MR image, which can be compared to the corresponding US image. The same structures can be observed in the two images. In particular, the glue that is not visible in the MRI can be clearly seen in the transformed image displayed in Fig. 4(b). Finally, it is interesting to mention that the regularization parameters were fixed to their best values by visual inspection of the fused images, leading to $\tau_1 = 10^{-2}$, $\tau_2 = 3.10^{-6}$, $\tau_3 = 2.10^{-4}$ and $\tau_4 = 10^{-5}$. Interestingly, these values were not modified for the two experimental datasets considered in this study. Section 4.2.3.5 detailed the influence of the hyperparameters on the fused image.

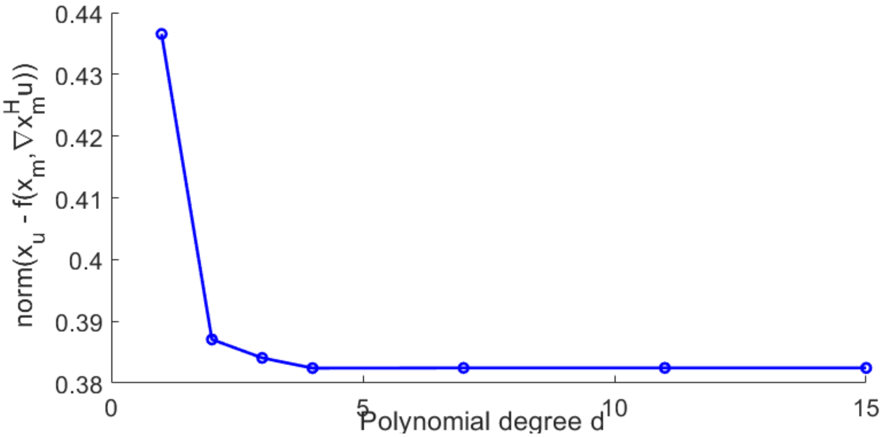

Figure 4.3: Error norms between experimental US and MR images versus the polynomial degree d.

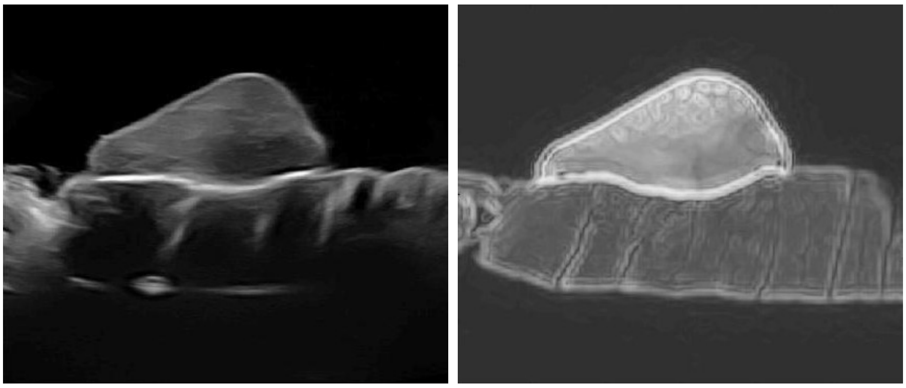

(a) $\mathbf{y}_\mathrm{u}$

(b) $f(\mathbf{y}_\mathrm{m}, \nabla\mathbf{y}_\mathrm{m}{}^H\mathbf{u})$

Figure 4.4: (a) US image, (b) MR image obtained after applying the estimated polynomial function, representing the same imaged medium. The original MR image is shown in Fig. 4.5(b)

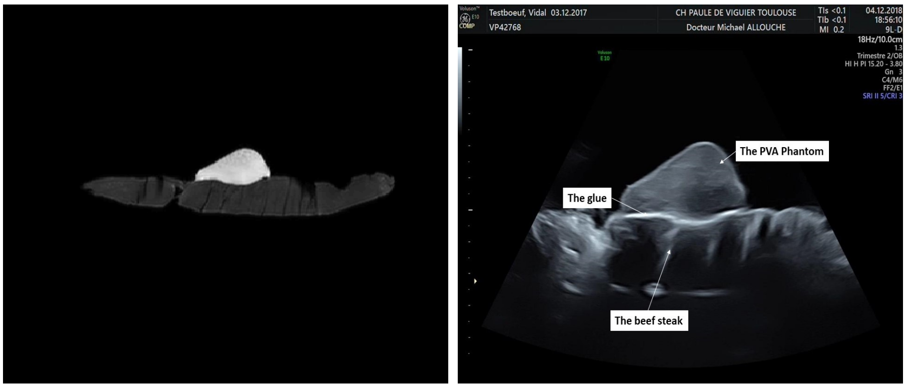

(a) MRI observation (b) US observation

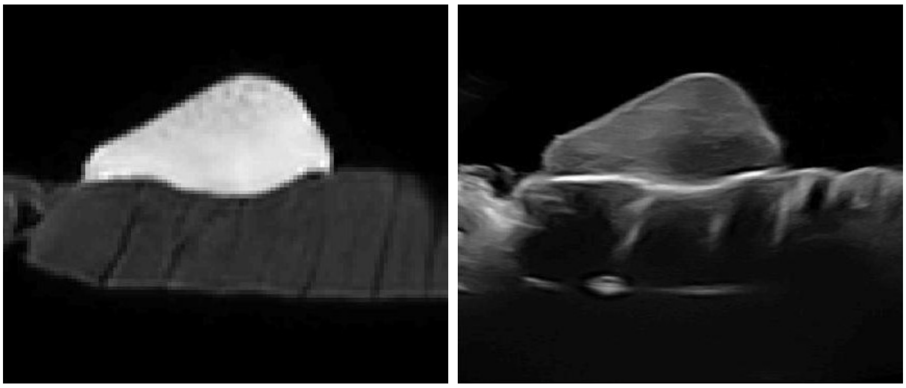

(c) MRI observation cropped (d) US observation cropped

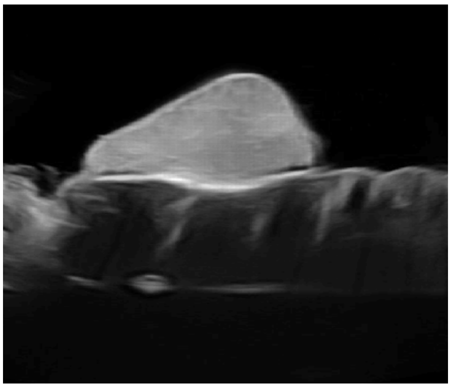

(e) Fused image

Figure 4.5: Image fusion results. (a,b) Full view and cropped MR images, (c,d) Full view and cropped US images, (e) fused image with the proposed method.

(a) MRI observation (b) US observation

(c) MRI observation cropped (d) US observation cropped

(e) Fused image

Figure 4.6: Image fusion results. (a,b) Full view and cropped MR images, (c,d) Full view and cropped US images, (e) fused image with the proposed method.

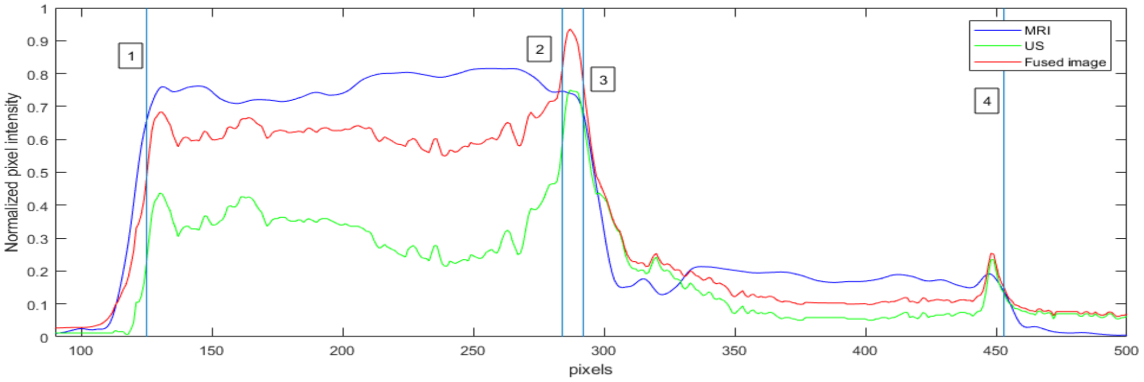

(a)

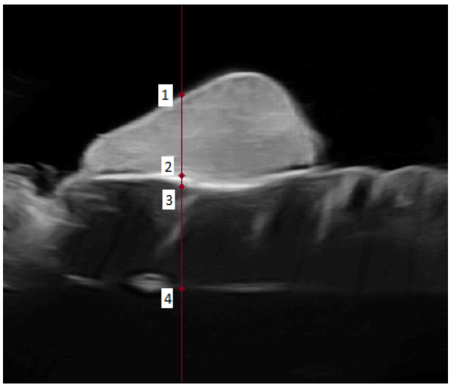

(b)

Figure 4.7: (a) shows normalized pixel intensities of extracted lines from MRI, US and the fused image in 4.5. The MRI observation is in blue, the US observation is in green and the fused image is in red. The vertical straight lines indicate the delimited regions depicted in (b).

Table 4.3: CNR comparison for the phantom images.

	CNR		
	MRI	US	Fused image
SET 1 (Fig. 3)	48.76 dB	20.64 dB	37.73 dB
SET 2 (Fig. 4)	54.71 dB	15.72 dB	45.85 dB

The MRI and US observations displayed in Figs. 4.5(a-d) and 4.5(a-d) clearly contain complementary information. MRI provides a wide field of view and a good contrast between the beef steak and the polyvinyl alcohol phantom, but with limited spatial resolution. The lack of spatial resolution prevents, for example, the observation of the glue between the slice of meat and the Polyvinyl Alcohol Phantom (PVA) phantom. On the other hand, US images have a limited field of view but provide a better spatial resolution, allowing for example the glue structure to be imaged very precisely. Figs. 4.5(e) and 4.6(e) show the fused images obtained with the proposed algorithm. The benefit of fusing the two imaging modalities can be observed, yielding a fused image having the good contrast of MRI and the fine spatial resolution of US. In addition to the visual inspection of the different images, the performance of the proposed fusion method was evaluated using two quantitative measures. The first measure is the contrast-to-noise ratio (CNR) [WR13], which can be used to evaluate the contrast between two different structures in MR, US and fused images. The CNR is defined as

$$\text{CNR} = \frac{|\mu_i - \mu_j|}{\sqrt{\sigma_i^2 + \sigma_j^2}}$$

where μ_i, μ_j, σ_i^2 and σ_j^2 are the means and standard deviations of two blocks of pixels extracted from two different structures. The two regions considered in this study were chosen inside the PVA phantom and the beef steak, respectively (see Fig. 4.5(b)). The CNR values associated with these two regions are reported in Table 4.3. They clearly demonstrate that image fusion allows the image contrast to be improved for both experiments (by factors of 82.1% and 191.67% for the two datasets) compared to US images.

The objective of the second quantitative measure is to evaluate the spatial resolution of MR, US and fused images. It is based on the image profiles crossing the boundary between different structures. The slope of these profiles at the interface between two structures was computed and is used as an indicator of spatial resolution [MBBK15]. Fig. 4.7 and Table **??** highlight the improved spatial resolution resulting from the fusion of the two modalities. We observe that the fused image can differentiate neighbouring structures and highlight small structures as the glue, contrary to MRI images. For example, the second interface in Fig. 4.7, between the PVA phantom and the glue is not distinguishable in the MRI, while it is clearly visible in the US and fused images. This observation is confirmed by the slope coefficients reported in Table **??**. These two measures confirm the benefit of fusing the two imaging modalities, yielding a fused image having a good contrast (better than the contrasts of US images) and a fine spatial resolution (better than the low spatial resolution of MRI).

4.2.3.5 Hyperparameters

Similarly to most of the existing image reconstruction algorithms, the quality of the fusion algorithm investigated in this chapter depends on the values of the hyperparameters. The proposed algorithm requires to adjust 4 hyperparameters:

- τ_1: this hyperparameter balances the weight between the MRI data fidelity term and the total variation regularization. Considering that TV promotes a piece-wise constant fused image, increasing τ_1 decreases the resolution of the fused image, which is measured using slope interfaces (see Fig. 7 in the paper). This remark has been highlighted in Fig. 4.8 below: when τ_1 exceeds 5.10^{-2}, the slope 2 interface starts to decrease and the fused image is blurred.

- τ_3: this hyperparameter has the same effect as τ_1 on the fused image.

- τ_4: this hyperparameter is essential in the proposed fusion algorithm. The choice of τ_4 is based on the quality of MRI and US images. Different values of τ_4 provide different fusion results. When τ_4 has a low value, the fused image is close to the high-resolution MRI image. Conversely, when τ_4 has a high value, the fused image is a despeckled US image as shown in Fig. 4.9.

- τ_2: this hyperparameter has the same effect as τ_4 on the fused image.

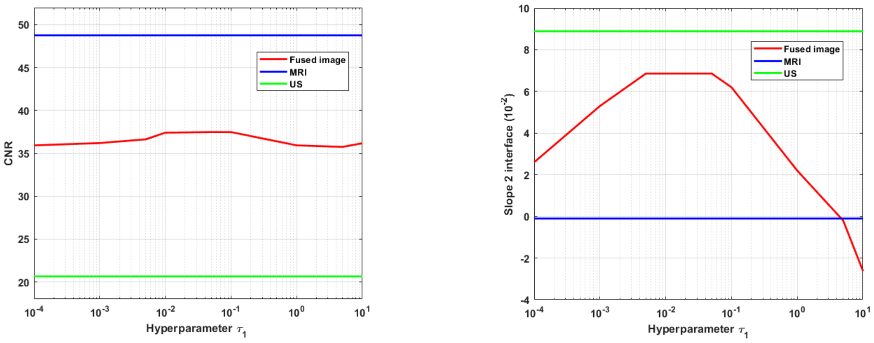

Figure 4.8: Influence of the hyperparameter τ_1 on the fused image. (a) shows the CNR evolution whereas (b) shows the evolution of the interface 2 slope.

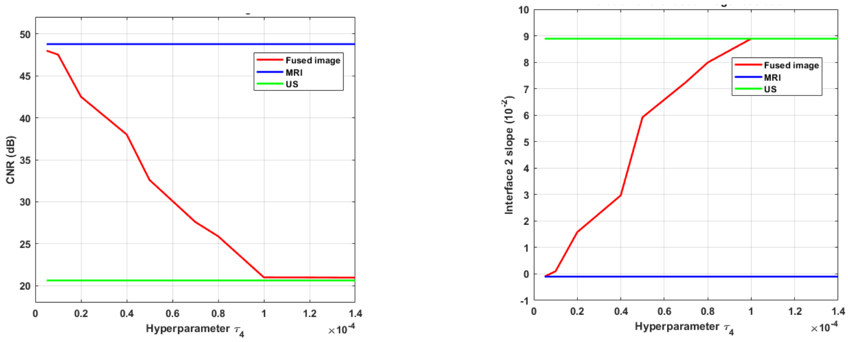

Figure 4.9: Influence of the hyperparameter τ_4 on the fused image. (a) shows the CNR evolution whereas (b) shows the evolution of the interface 2 slope.

The values of the regularization parameters can also be chosen after visual inspection of the fused image using the performance measures studied in this section. However, it would be interesting to investigate some methods to tune these hyperparameters automatically from the data as the SURE algorithm [PSC+16] or other Bayesian methods.

4.2.3.6 Comparison between several fusion methods for MRI and US images

Qualitative comparison results

This section demonstrates the efficiency of the proposed MRI/US fusion method, and presents some comparative results with different fusion techniques. We have considered a multi-scale Laplacian method [AAVB16] and a discrete wavelet transform [LBCA10] whose outputs are displayed in Fig.

4.10 (for more details about these fusion techniques, see Chapter 3). In order to make a more fair comparison, we have denoised the US image before fusion since our proposed strategy also performs denoising. The figures displayed below show the effect of noise on the fused image. For low SNR, the multi-scale fused image and the wavelet fused image contain distracting artifacts, especially in the regions containing strong transitions between organs.

Quantitative comparison results

The performance of the proposed fusion algorithm was evaluated using a quantitative metric, namely the Petrovic fusion metric [Pet07]. This metric associates important visual information with the edge information in each pixel. Thus, a measure of fusion performance is obtained by evaluating the amount of edge information that is transferred from input images to the fuse image. Fig. 4.11 clearly demonstrates that for higher noise levels the fusion becomes more complicated.

SNR $= 40$dB

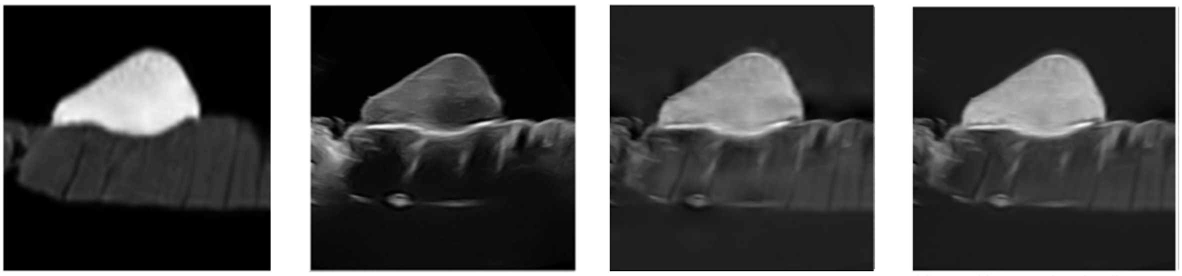

(a) MRI image

(b) Ultrasound image
$\mathrm{SN}R = 40$ dB

(c) Fused image using the Laplacian pyramid method without denoising
$\mathrm{SN}R = 40$ dB

(d) Fused image using the discrete wavelet method without denoising
$\mathrm{SN}R = 40$ dB

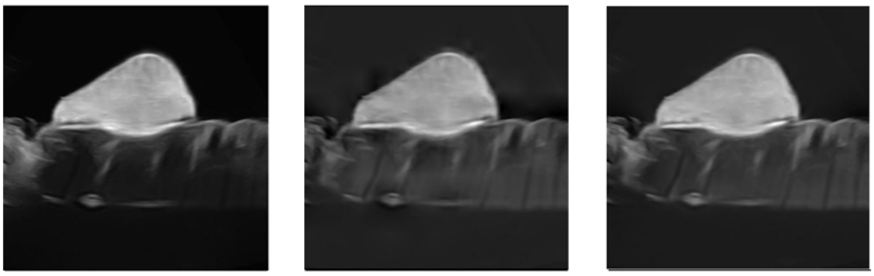

(e) The proposed fused image

(f) Fused image using the Laplacian pyramid method with denoising

(g) Fused image using the discrete wavelet method with denoising

SNR $= 25$dB

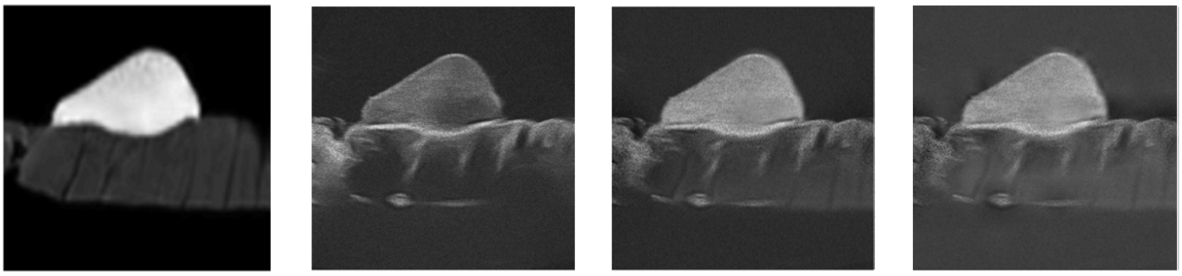

(a) MRI image

(b) Ultrasound image
$\mathrm{SN}R = 25$ dB

(c) Fused image using the Laplacian pyramid method without denoising
$\mathrm{SN}R = 25$ dB

(d) Fused image using the discrete wavelet method without denoising
$\mathrm{SN}R = 25$ dB

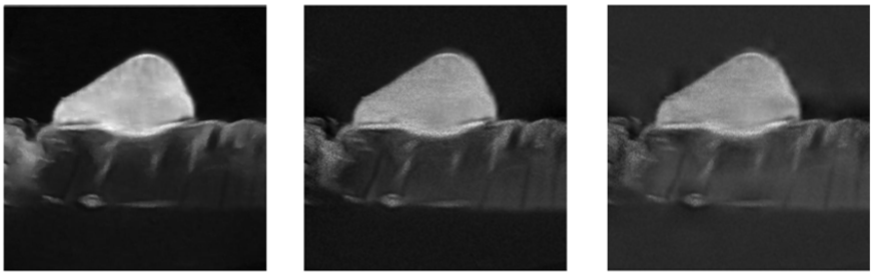

(e) The proposed fused image

(f) Fused image using the Laplacian pyramid method with denoising

(g) Fused image using the discrete wavelet method with denoising

SNR = 10dB

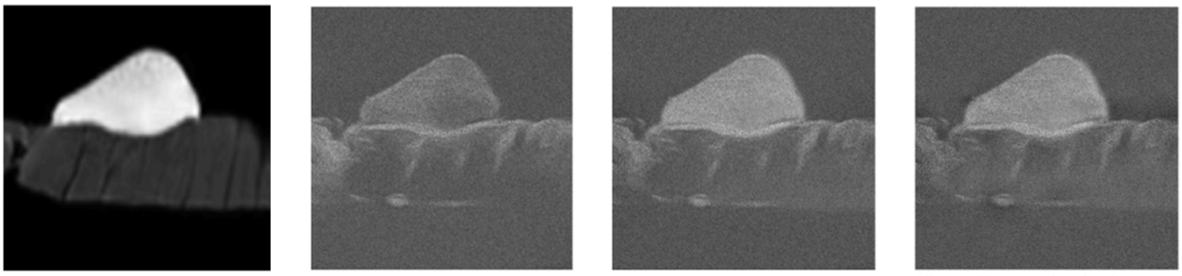

(a) MRI image

(b) Ultrasound image $SNR = 10$ dB

(c) Fused image using the Laplacian pyramid method without denoising $SNR = 10$ dB

(d) Fused image using the discrete wavelet method without denoising $SNR = 10$ dB

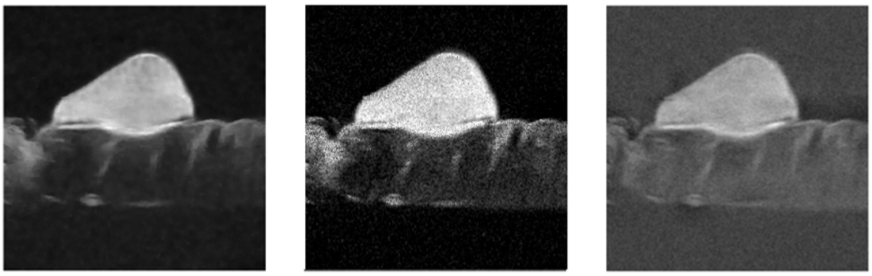

(e) The proposed fused image

(f) Fused image using the Laplacian pyramid method with denoising

(g) Fused image using the discrete wavelet method with denoising

SNR = 5dB

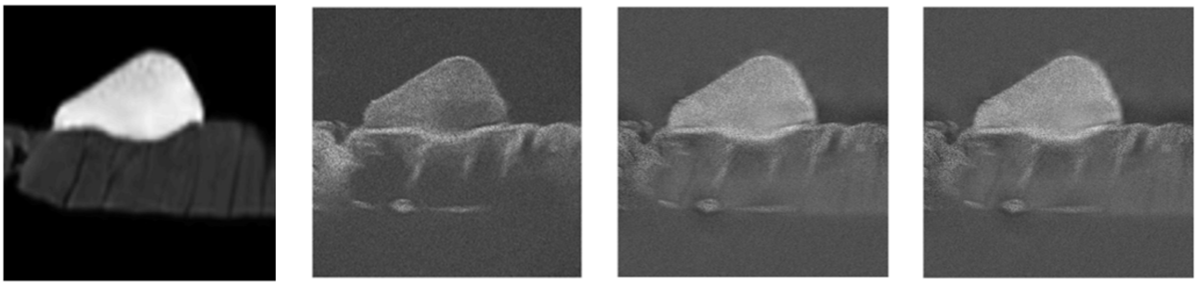

(a) MRI image

(b) Ultrasound image $SNR = 5$ dB

(c) Fused image using the Laplacian pyramid method without denoising $SNR = 5$ dB

(d) Fused image using the discrete wavelet method without denoising $SNR = 5$ dB

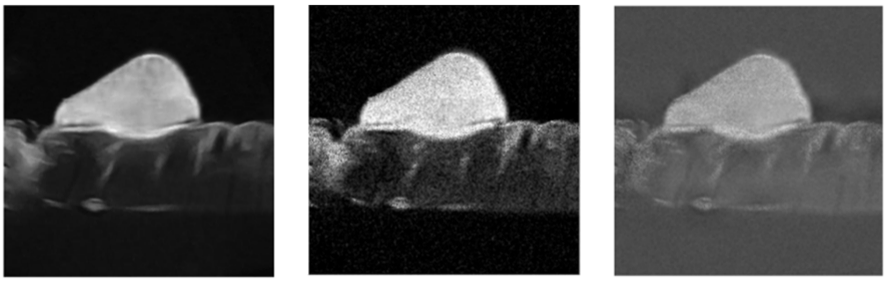

(e) The proposed fused image

(f) Fused image using the Laplacian pyramid method with denoising

(g) Fused image using the discrete wavelet method with denoising

Figure 4.10: Influence of SNR of the ultrasound image on the fused images, (a) and (b) are the MRI and US images, (c) and (d) show the fused images using the Laplacian pyramid and the discrete wavelet methods without denoising the US image, (e) shows the fused image using the proposed method, (f) and (g) show the fused images using the Multi-scale Laplacian pyramid and the discrete wavelet methods after denoising the US image.

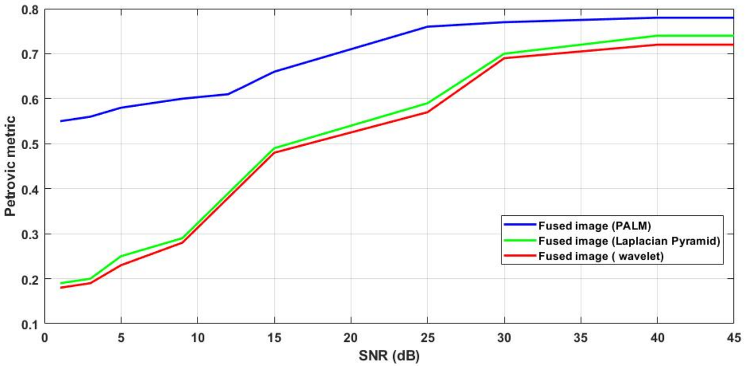

Figure 4.11: Influence of SNR on the Petrovic metric for the fused images. The proposed fusion method is in blue, the Multi-scale Laplacian method is in green and the discrete wavelet transform fusion is in red.

4.2.3.7 PALM initialization

The PALM algorithm alternates between two optimization problems estimating $\boldsymbol{x}$ and $\boldsymbol{v}$ alternatively. The two vectors $\boldsymbol{x}$ and $\boldsymbol{v}$ are supposed to have the same size. All algorithms were initialized using a high resolution (HR) MRI image for $\boldsymbol{x}$ and the observed US image for $\boldsymbol{v}$. The HR MRI image was computed using the nearest-neighbor interpolation.

We introduce other sets of images to initialize Algo 1. For the initialization of $\boldsymbol{x}$, we consider two methods:

1. MRI1: HR MRI using the nearest-neighbor interpolation method.
2. MRI2: HR MRI using Fast Single Image Super-resolution method with an analytical solution [ZWB+16a].

For the initialization of $\boldsymbol{v}$:

1. US1: The observed US image.
2. US2: Denoised US image using deep neural network (MATLAB pretrained neural network that identifies and removes artifacts and noise from images).
3. US3: Denoised US image using wavelet image denoising [AO12]

Some examples obtained using different initializations are presented below. As we can see, the obtained solutions are very similar for all these initializations.

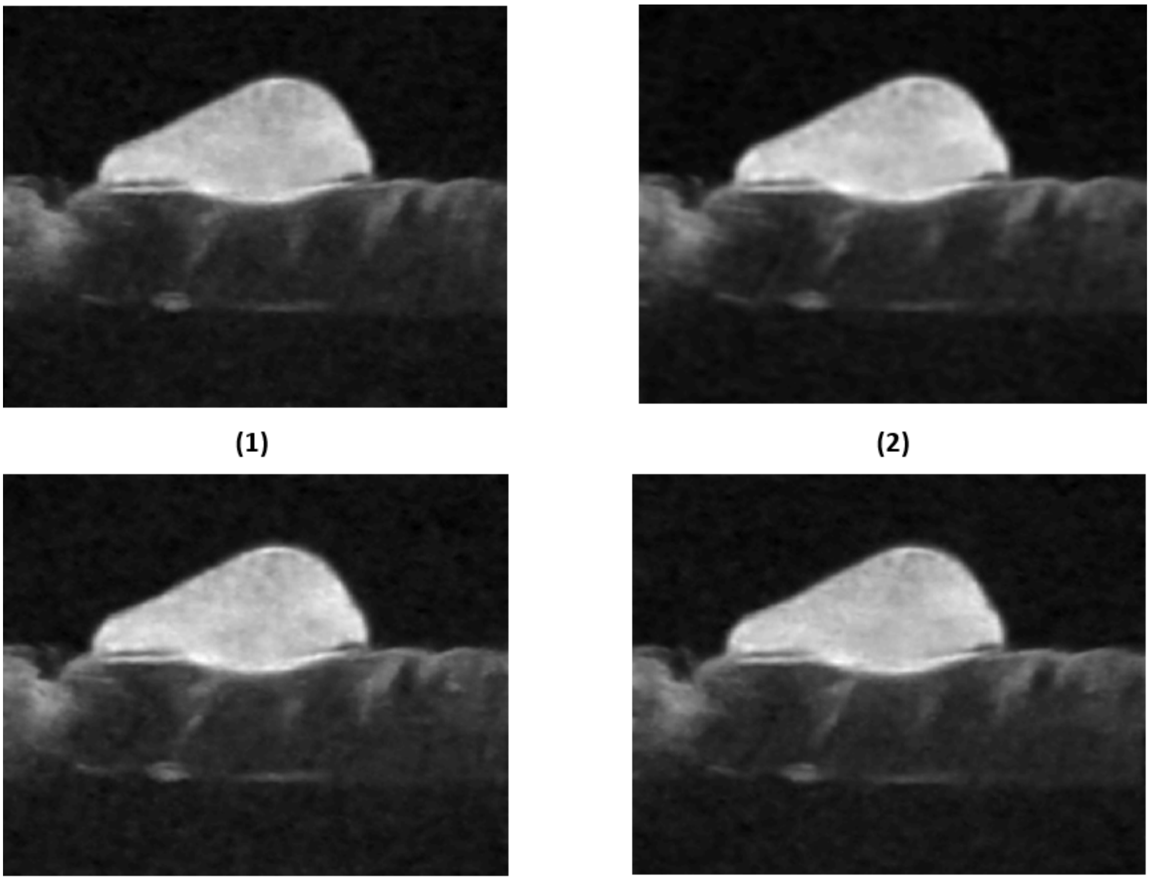

(1)

(2)

(3)

(4)

Figure 4.12: Figure 1 :Fusion results with different initializations: (1) $\boldsymbol{x}_0$ = MRI1 and $\boldsymbol{v}_0$ = US1, (2) $\boldsymbol{x}_0$ = MRI2 and $\boldsymbol{v}_0$ = US1, (3) $\boldsymbol{x}_0$ = MRI2 and $\boldsymbol{v}_0$ = US2, (4) $\boldsymbol{x}_0$ = MRI2 and $\boldsymbol{v}_0$ = US3.

4.3 MR/US images fusion using a patch-wise polynomial

MR/US image fusion using a patch-wise polynomial model is based on observation model presented in Section 4.2 but presents a variant of the function f to model the relationship between MRI and US images. The function f was represented by a global polynomial in the previous section, and in [RPMA01] for multimodal image registration. However, the relationship between MR and US images may depend on tissue acoustic and magnetic properties, and thus may change from one image region to another. Thus, considering a global polynomial model may lead to inaccurate gray level matching in specific image regions. To overcome this issue, this section introduces a more general patch-based polynomial model, fitting independently low-order polynomial functions to each overlapping patch extracted from MR and US images. This patch-based polynomial model is defined as

$$\boldsymbol{P}_p \boldsymbol{x}_{\text{us}} = f_p(\boldsymbol{P}_p \boldsymbol{x}_{\text{mr}}, \boldsymbol{P}_p \nabla \boldsymbol{x}_{\text{mr}}^H \boldsymbol{u}), \tag{4.28}$$

where $\boldsymbol{P}_p \in \mathbb{R}^{n \times N}$ is a binary operator that extracts the pth patch of size n from an image of size N. In the following, N_p will denote the total number of patches. Replacing f_p by a polynomial function, the relation between patches from the US and MR images becomes

$$\boldsymbol{P}_p \boldsymbol{x}_{\text{us}} = \sum_{l+k \leq d_p} c_{l,k,p} \, \boldsymbol{P}_p \boldsymbol{x}_{\text{mr}}^l \odot (\boldsymbol{P}_p \nabla \boldsymbol{x}_{\text{mr}}^H \boldsymbol{u})^k, \tag{4.29}$$

where $p = 1, ..., N_p$ is the patch number, d_p and $c_{l,k,p}$ are the order and the coefficients of the polynomial function f_p corresponding to patch $\#p$, $\odot$ is the Hadamard product (element by element multiplication) and the power operations applied to vectors are element-wise. The final function f is obtained by averaging patch-wise polynomials, since each pixel of the image is contained in several overlapping patches. More precisely, the transformation of the ith pixel denoted as $f_i : \mathbb{R}^N \times \mathbb{R}^N \to \mathbb{R}$ is the average of all the polynomials associated with the patches containing this pixel.

4.3.1 Estimation of the polynomial functions f_p

For a given degree d_p, the polynomial function f_p relating patches $\boldsymbol{P}_p \boldsymbol{x}_{\text{mr}}$ and $\boldsymbol{P}_p \boldsymbol{x}_{\text{us}}$ is defined by $(d_p + 1)(d_p + 2)/2$ coefficients assembled in the vector $\boldsymbol{c}_{d,p} = \{c_{k,l,p} \mid k + l \leq d_p\}$. To estimate these coefficients, we consider that the pth observed MR and US patches are related according to

$$\boldsymbol{P}_p y_{\text{us}} = \sum_{k+l\leq 3} c_{kl,p} \boldsymbol{P}_p \boldsymbol{y}_{\text{mr}}^l \odot (\boldsymbol{P}_p \nabla \boldsymbol{y}_{\text{mr}}^H u)^k + \epsilon_p,$$

or in a matrix form

$$\boldsymbol{P}_p \boldsymbol{y}_{\text{us}} = \boldsymbol{A}_{\text{mr},p} \boldsymbol{c}_{d,p} + \boldsymbol{\epsilon}_p, \tag{4.30}$$

where $\boldsymbol{A}_{\text{mr},p}$ is a matrix whose elements are $\boldsymbol{P}_p \boldsymbol{y}_{\text{mr}}^l \odot (\boldsymbol{P}_p \nabla \boldsymbol{y}_{\text{mr}}^H \boldsymbol{u})^k$ for $l + k \leq d_p$, and $\boldsymbol{\epsilon}_p$ is the measurement error.

The least-squares estimator of $\boldsymbol{c}_{d,p}$ is defined by

$$\hat{\boldsymbol{c}}_{d,p} = \boldsymbol{A}_{\text{mr},p}^{\dagger} \boldsymbol{P}_p \boldsymbol{y}_{\text{us}}, \quad p = 1, ..., N_p,$$

where $\boldsymbol{A}_{\text{mr},p}^{\dagger} = (\boldsymbol{A}_{\text{mr},p}^T \boldsymbol{A}_{\text{mr},p})^{-1} \boldsymbol{A}_{\text{mr},p}^T$ is the pseudo-inverse of the matrix $\boldsymbol{A}_{\text{mr},p}$.

In order to estimate the polynomial degree of the p^{th} patch, we minimize the least square distance between $\boldsymbol{P}_p \boldsymbol{y}_{\text{mr}}$ and $\boldsymbol{P}_p \boldsymbol{y}_{\text{us}}$, i.e., solve the following problem

$$\underset{d_p}{\text{argmin}} \quad \|\boldsymbol{P}_p \boldsymbol{y}_{\text{us}} - f_p(\boldsymbol{P}_p \boldsymbol{y}_{\text{mr}}, \boldsymbol{P}_p \nabla \boldsymbol{y}_{\text{mr}}^H \boldsymbol{u})\|^2, \tag{4.31}$$

where we highlight that the polynomial degree d_p depends on the patch size. In the results provided in this paper, patches of size 30×30 were extracted from images containing 600×600 pixels, with an overlap of 25%. The degree of the polynomial relating the patches was constrained to $d_p \in \{1, ..., 3\}$.

Note that the same algorithm (Algo. 1) can be used for this fusion method with a function f estimated using Eqs. 4.30 and 4.31 instead of Eqs. 4.25 and 4.26.

4.3.2 Experimental results using a patch-wise polynomial function

To mitigate the relatively good SNR obtained due to the phantom design, the US image was further degraded by log-Rayleigh noise as shown in Fig. 4.13(c). Figs. 4.13(a,b,c) highlight the differences in gray levels, spatial resolution, contrast, and noise between the two MR and US images. Three main structures can be observed in these images: a PVC phantom (bright structure in the MR image), a piece of beef meat (gray structure in the MR image), and the glue used to attach them, only visible

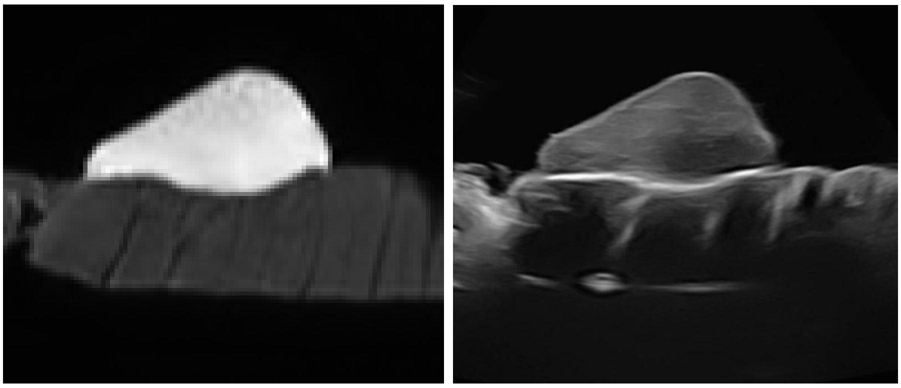

(a) MRI (b) US image

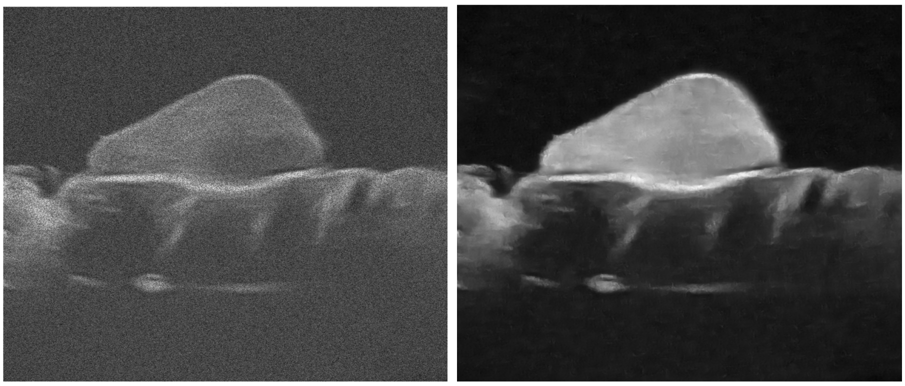

(c) Noisy US image (d) Global polynomial fused image

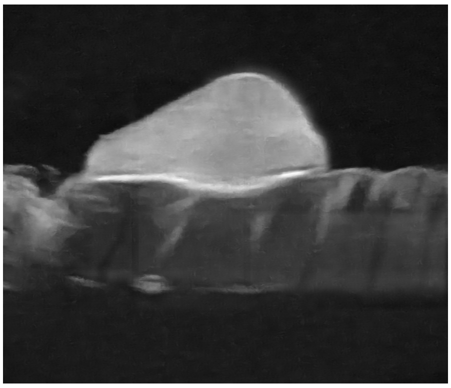

(e) Patch-wise polynomial fused image

Figure 4.13: Original MR image (200 × 200 pixels) and US image (600 × 600 pixels) and fusion results: (a) observed MRI, (b) original US image, (c) noisy US image, (d) fused image using a global polynomial model, (e) fused image with the proposed path-based polynomial model.

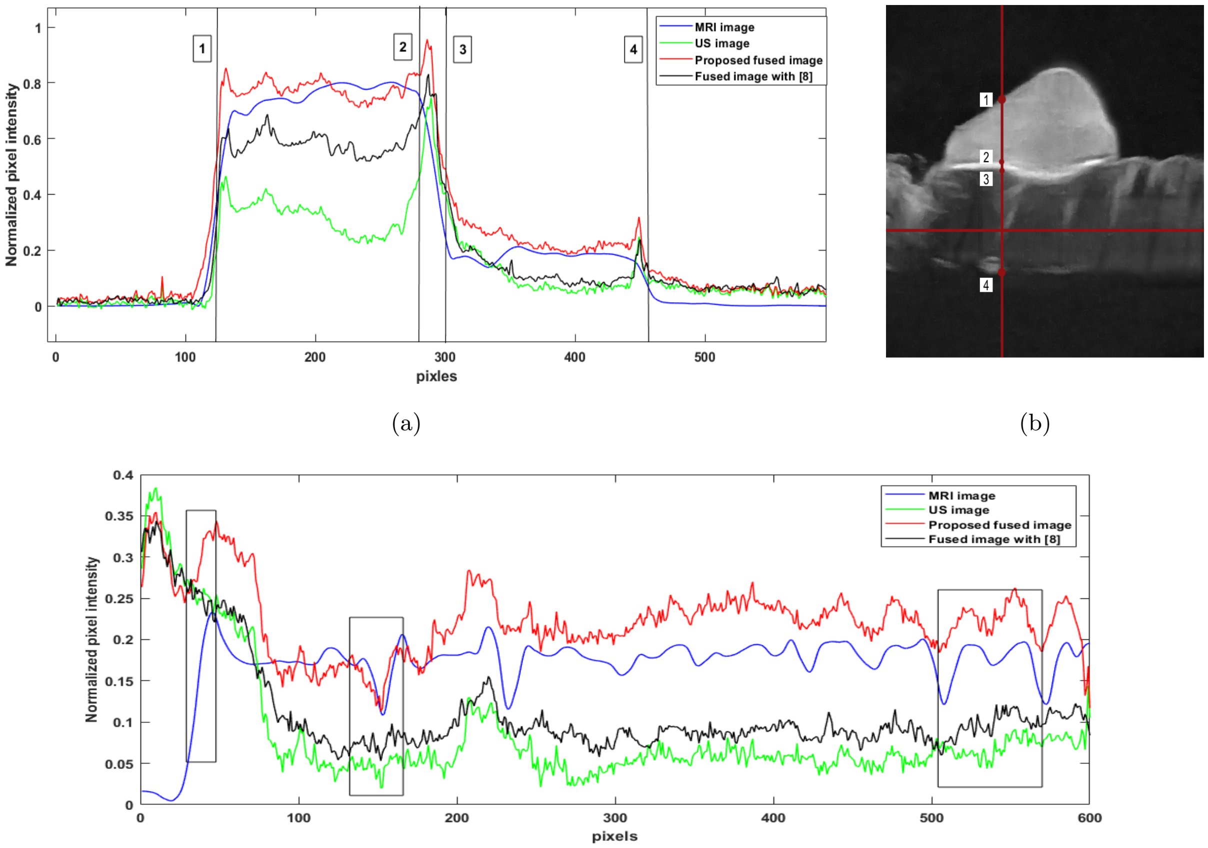

(a) (b)

(c)

Figure 4.14: (a) and (c) show normalized pixel intensities of extracted lines from the MR, US and fused images (using the global polynomial fusion and the proposed patch-based fusion). (a) shows the vertical straight lines in (b) whereas (c) displays the horizontal straight lines in (b).

Table 4.4: CNR results

CNR			
MRI	US	Fused image with [EMVB⁺20]	Proposed
48.76 dB	20.64 dB	37.73 dB	41.72

Table 4.5: Slope values at the interface between different regions of interest in the MR, US and fused images, corresponding to the vertical profile in Fig. 4.14.

Slope	MRI	US	Fused image with [EMVB⁺20]	Proposed
#1	2.89	7.42	7.42	7.42
#2	-0.10	8.89	6.86	7.15
#3	3.57	5.47	4.61	5.24
#4	-1.35	-1.95	-2.05	-2.05

in the US image. Figs. 4.13(c,d) show the fused images obtained using a global polynomial and the local approach. Both fused images gather information from MR and US images (with a small preference to the local method): they provide a good contrast between the PVC and the beef tissue (similar to MRI), a good spatial resolution (similar to US) allowing small structures such as the glue to be distinguished, and good SNR. Moreover, the image obtained after fusion seems to carry more information than MRI, especially in the beef tissue.

In addition to visual inspection, the performance of the proposed patch-wise method was evaluated using two quantitative measures and compared to the global fusion method of [EMVB$^+$20]: 1) the contrast-to-noise ratio (CNR) [WR13] between the PVC and the beef meat, and 2) the slope between two neighboring structures as an indication of the spatial resolution [MBBK15]. As reported in Tables 4.4 and 4.5, the patch-wise approach offers a good compromise between MR and US images with a CNR close to that of the MRI and a slope close to that of the US image. Fig. 4.14 confirms these results, showing that the patch-wise fused image captures more details from the MRI than the global model-based fused image. However, we would like to mention that the patch-wise approach is more time consuming compared to the global polynomial. Thus, the choice of the adapted method depends on the application.

4.4 Conclusion

This chapter studied new fusion methods for magnetic resonance (MR) and ultrasound (US) images. The proposed methods were able to reconstruct a fused image containing information from both observations, by solving a super-resolution inverse problem for MRI and a despeckling problem for US images. These two problems were solved jointly by using appropriate statistical models and polynomial relationships between the images of interest. A PALM algorithm was finally investigated to solve the resulting fusion problem. Results obtained on simulated and real images clearly showed the interest of combining the information contained in these two imaging modalities, instead of restoring them independently.

To the best of our knowledge, this work is a first attempt for fusing MR and US images. It opens several interesting perspectives. A natural progression of this work is to combine the proposed framework with multimodal image registration, which would allow the proposed MR/US image fusion to be robustified, which is the aim of the next chapter.

CHAPTER 5

Joint registration and fusion of MRI and ultrasound images

Contents

5.1 Introduction . . . 115
5.2 MR/US image fusion and registration . . . 116
  5.2.1 Observation models . . . 116
  5.2.2 US/MR dependence model . . . 117
  5.2.3 Proposed inverse problem . . . 119
5.3 Proposed registration . . . 120
  5.3.1 Similarity measure . . . 120
  5.3.2 Spatial transformation . . . 121
  5.3.3 Regularization . . . 123
5.4 Optimization algorithm for joint fusion and registration . . . 123
  5.4.1 Estimation of the fused image for known (T_c) . . . 124
  5.4.2 Estimation of the spatial transformation . . . 126
  5.4.3 Estimation of the polynomial function . . . 127
  5.4.4 Proposed algorithm . . . 127
  5.4.5 Performance measures . . . 127
  5.4.6 Simulation results on synthetic data . . . 129
  5.4.7 Experimental results on phantom data . . . 131
  5.4.8 Hyperparameters . . . 137
5.5 Conclusions . . . 137

5.1 Introduction

This chapter presents a joint registration and fusion method for MR and US images. Considering the limitations of each modality, we have constructed in the previous chapter two observation models to enhance the quality (in terms of resolution and contrast) of both images. A first model is introduced for the MR image based on a linear model formed by blurring and downsampling matrices. This model has been used for super-resolution in several studies [GEW10, GPOK02, MCB+10b]. A denoising model is considered for the US image in order to mitigate the effect of speckle noise [AB07b, TSP88b, GCS05b]. Since US and MR modalities are different by their nature and content, there is no simple correspondence between gray levels in these images. A polynomial function was used in [RPMA01, EMVB+20] and in the previous chapter to link intensities of MR and US images. However, in order to consider the possible misalignment between MR and US images, we consider an MR/US registration step in order to estimate the non-linear transformation relating these two images. This transformation is composed of a local transformation based on B-splines and a global transformation based on an affine operator. This leads to a sophisticated and complex optimization problem, which is handled via a PALM algorithm [BST14]. The main contribution of this chapter with respect to Chapter 4 is a fusion algorithm able to mitigate the mis-registration errors between the MR and US images. The possibility of handling mis-registration errors is essential for clinical applications since MR and US images are not aligned because of the differences in acquisition setups, while their alignment is a crucial requirement for the fusion process. Simulated data with controlled ground truth are used to evaluate the proposed fusion/registration method. Experimental data collected on a phantom with some similar characteristics to endometriosis are then considered.

5.2 MR/US image fusion and registration

5.2.1 Observation models

As explained previously, MR and US images are two medical modalities that have their specific strengths and weaknesses. The main purpose of obtaining a fused image from these two modalities is to take benefit from their strengths and mitigate their weaknesses. In the following, $\mathbf{y}_{\mathrm{m}} \in \mathbb{R}^M$ and $\mathbf{y}_{\mathrm{u}} \in \mathbb{R}^N$ denote the observed MR and US images, which are the inputs of the proposed fusion algorithm. Both observed images are related to the ideal fused image through two models accounting for the degradation affecting the two modalities. In particular, the limited spatial resolution of the

MR image is classically modelled using a blur, a down-sampling operator and additive white Gaussian noise [GEW10, GPOK02, MCB+10b]. The speckle noise contaminating the US image is modelled as an additive log-Rayleigh noise [AB07b, TSP88b, GCS05b]. The resulting joint observation models associated with the MR and US images (introduced in Chapter 4) are:

$$\begin{aligned} \boldsymbol{y}_{\mathrm{m}} &= \boldsymbol{S}\boldsymbol{C}\boldsymbol{x}_{\mathrm{m}} + \boldsymbol{n}_{\mathrm{m}} \\ \boldsymbol{y}_{\mathrm{u}} &= \boldsymbol{x}_{\mathrm{u}} + \boldsymbol{n}_{\mathrm{u}}, \end{aligned} \tag{5.1}$$

where $\boldsymbol{x}_{\mathrm{m}} \in \mathbb{R}^N$ is the MR high-resolution image and $\boldsymbol{x}_{\mathrm{u}} \in \mathbb{R}^N$ is the despeckled US image, $\boldsymbol{C} \in \mathbb{R}^{N\times N}$ is a BCCB matrix (block circulant with circulant blocks) that models the blur in the MR image and $\boldsymbol{S} \in \mathbb{R}^{M\times N}$ (with $N = s^2M$) is a decimation matrix (with a decimation factor of s in each spatial direction). The two observation equations in (5.1) are used to estimate the fused image of interest by taking benefit from both MR and US measurements. The first equation in (5.1) has been used in many super-resolution methods to recover the high-resolution MR image $\boldsymbol{x}_{\mathrm{m}}$ from its noisy low-resolution counterpart $\boldsymbol{y}_{\mathrm{m}}$ [GEW10, GPOK02, MCB+10b]. The second equation in (5.1) has been considered in denoising methods for US images [AB07b, TSP88b, GCS05b]. The proposed approach combines both observation equations to improve the resolution of the MR image and denoise the US image. An additional model, detailed in the next section, is also considered to link $\boldsymbol{x}_{\mathrm{m}}$ and $\boldsymbol{x}_{\mathrm{u}}$ that are different even in the ideal noiseless case, because of the different physical phenomena behind each imaging modality.

5.2.2 US/MR dependence model

The proposed joint fusion and registration method is a pure intensity-based approach that does not require any feature extraction. It relies on the assumption that the differences between $\boldsymbol{x}_{\mathrm{m}}$ and $\boldsymbol{x}_{\mathrm{u}}$ are due to two properties: i) the MR and US images are not perfectly aligned. This misalignment is modelled by a geometric transform denoted as T, and ii) the relation between the pixel intensities in the two images can be well approximated by a deterministic non-linear function denoted as $f_{\boldsymbol{c}}$. Combining these two properties, the principle of the proposed algorithm is to search for a spatial transformation T and an intensity mapping $f_{\boldsymbol{c}}$, in order to match $\boldsymbol{x}_{\mathrm{u}}$ to $T(\boldsymbol{x}_{\mathrm{m}})$. Note that the function $f_{\boldsymbol{c}}$ does not relate the pixel intensities from the two images directly, but it uses the fact that the US image is mainly sensitive to interfaces between anatomical surfaces with different acoustic impedances. As explained in the previous chapter, the mapping $f_{\boldsymbol{c}}$ relates the US gray levels to the gray levels and the gradients of the MR image calculated in the direction of US wave propagation (see [RPMA01] for more details). Plugging T and $f_{\boldsymbol{c}}$ into (5.1) results into the following observation models:

$$\begin{aligned} \boldsymbol{y}_{\mathrm{m}} &= \boldsymbol{S}\boldsymbol{C}\boldsymbol{x} + \boldsymbol{n}_{\mathrm{m}} \\ \boldsymbol{y}_{\mathrm{u}} &= f_{\boldsymbol{c}}(T(\boldsymbol{x}), \nabla T(\boldsymbol{x})^H \boldsymbol{u}) + \boldsymbol{n}_{\mathrm{u}}, \end{aligned} \tag{5.2}$$

where $\boldsymbol{x} \in \mathbb{R}^N$ is the fused image to be estimated, which contains information from both MR and US modalities. The function $f_{\boldsymbol{c}} : \mathbb{R}^{\mathbb{N}} \times \mathbb{R}^{\mathbb{N}} \to \mathbb{R}^{\mathbb{N}}$ allows the gray level intensities of MR and US images to be matched, and $T(.)$ is a geometric transformation due to possible mis-registration. Note that the ith component of $\nabla T(\boldsymbol{x})^H \boldsymbol{u} \in \mathbb{R}^{\mathbb{N}}$ contains the inner product between the ith local gradient of $T(\boldsymbol{x})$ and the US scan direction $\boldsymbol{u}$. Note also that the proposed fusion model (5.2) reduces to the model investigated in the previous chapter when $T(\boldsymbol{x}) = \boldsymbol{x}$, which corresponds to the ideal case where the MR and US images are perfectly aligned.

As shown in [RPMA01, EMVB$^+$20], the unknown function $f_{\boldsymbol{c}}$ in (5.2) can be efficiently approximated by a polynomial of order d. This approximation consists of decomposing the ith component of $\boldsymbol{x}_{\boldsymbol{u}} = f_{\boldsymbol{c}}(T, \boldsymbol{x}_{\mathrm{m}}, \boldsymbol{u})$ as:

$$x_{\boldsymbol{u},i} = \sum_{p+q \leq d} c_{pq} T(\boldsymbol{x}^p_{\mathrm{m},i})(\nabla T(\boldsymbol{x}_{\mathrm{m}})^H \boldsymbol{u})^q_i, \tag{5.3}$$

where $\boldsymbol{c}$ is a vector containing all the unknown polynomial coefficients c_{pq} and the index $i \in \{1, ..., N\}$ is used for the ith coefficient of a vector. From the observation model (5.2) and the polynomial model (5.3), the objective of the proposed algorithm is to estimate the fused image $\boldsymbol{x}$ (with better spatial resolution, contrast and signal-to-noise ratio (SNR) than the original images $\boldsymbol{x}_{\mathrm{m}}$ and $\boldsymbol{x}_{\mathrm{u}}$, the geometric transform T (accounting for a possible mis-registration between the MR and US images) and the polynomial coefficients c_{pq} from the MR and US images $(\boldsymbol{y}_{\mathrm{m}}, \boldsymbol{y}_{\mathrm{u}})$ associated with the same tissue.

5.2.3 Proposed inverse problem

Based on some noise assumptions, i.e., additive Gaussian and additive log-Rayleigh noises for the MR and US images, an inverse problem was introduced in [EMVB+20] for the fusion of registered MR and US images. This problem was defined as

$$\begin{aligned}\hat{\boldsymbol{x}} = \underset{\boldsymbol{x}}{\operatorname{argmin}} \quad & \underbrace{\frac{1}{2}\|\boldsymbol{y}_{\mathrm{m}} - \boldsymbol{SCx}\|^2}_{\text{MR data fidelity}} \\ & + \underbrace{\tau_2 \sum_{i=1}^{N} \exp\left[y_{\mathrm{u},i} - f_i(\boldsymbol{x},\boldsymbol{u}) - \gamma(y_{\mathrm{u},i} - f_i(\boldsymbol{x},\boldsymbol{u}))\right]}_{\text{US data fidelity}} \\ & + \underbrace{\tau_1\|\nabla\boldsymbol{x}\|^2 + \tau_3\|\nabla f(\boldsymbol{x}, \nabla\boldsymbol{x}^H\boldsymbol{u})\|^2}_{\text{regularization}},\end{aligned} \tag{5.4}$$

where τ_1, τ_2 and τ_3 are hyperparameters that balance the weights of the total variation (TV) regularization and the data fidelity term, and $y_{u,i}$, $f_i(\boldsymbol{x},\boldsymbol{u})$ are the ith components of $\boldsymbol{y}_{\mathrm{u}}$ and $f(\boldsymbol{x}, \nabla\boldsymbol{x}^H\boldsymbol{u})$. Note that the two regularizations in (5.4) ensure some smoothness in the MR and US terms.

The fusion method based on (5.4) requires an accurate registration between MR and US images, as well as the knowledge of the pixel intensity mapping function $f_{\boldsymbol{c}}$. Of course, in practical applications, these two geometric and gray level transformations are not known and have to be estimated jointly with the fused image $\boldsymbol{x}$ from the data. Note that the perfect alignment between MR and US images is an important requirement for the success of most fusion algorithms. Thus considering the estimation of the geometric transform T jointly with the fused image is still an important challenge. This chapter proposes to tackle the joint fusion and registration problem by solving the following optimization problem

$$\begin{aligned}(\hat{\boldsymbol{x}}, \hat{T}, \hat{\boldsymbol{c}}) = \underset{\boldsymbol{x},T,\boldsymbol{c}}{\operatorname{argmin}} \quad & \underbrace{\frac{1}{2}\|\boldsymbol{y}_{\mathrm{m}} - \boldsymbol{SCx}\|^2}_{\text{MR data fidelity}} \\ & + \underbrace{\tau_2 \sum_{i=1}^{N} \exp\left[y_{\mathrm{u},i} - f_{\boldsymbol{c},i}(T,\boldsymbol{x},\boldsymbol{u}) - \gamma(y_{\mathrm{u},i} - f_{\boldsymbol{c},i}(T,\boldsymbol{x},\boldsymbol{u}))\right]}_{\text{US data fidelity}} \\ & + \underbrace{\tau_1\|\nabla\boldsymbol{x}\|^2 + \tau_3\|\nabla f_{\boldsymbol{c}}(T,\boldsymbol{x},\boldsymbol{u})\|^2 + \tau_5 R_{\mathrm{s}}(T)}_{\text{regularization}},\end{aligned} \tag{5.5}$$

where the optimization is conducted with respect to the transformation T, the polynomial coefficient vector $\boldsymbol{c}$ and the image of interest $\boldsymbol{x}$, $f_{\boldsymbol{c},i}(T, \boldsymbol{x}, \boldsymbol{u})$ is the ith component of $f_{\boldsymbol{c}}(T, \boldsymbol{x}, \boldsymbol{u})$ and $R_{\mathrm{s}}(T)$ is an additional regularization whose objective is to constrain the geometric transform T, as explained in the next section.

5.3 Proposed registration

5.3.1 Similarity measure

Most of the existing image registration methods can be classified into two categories: area-based and feature-based methods. In this chapter, it is more accurate to use an intensity-based technique because MR and US images are two distinct modalities from which it is difficult to extract automatically the same features. In general, any registration algorithm requires the following ingredients:

- An image similarity measure that quantifies the degree of similarity between the two images to be registered. The most common similarity measures (in particular for multi-modal image registration) are the mutual information (MI), the normalized mutual information (NMI) and the cross-correlation (CC). However, the mapping defined by the function $f_{\boldsymbol{c}}$ in (5.5) that matches the pixel intensities from the two image modalities was shown to be more appropriate to MR and US images in [RPMA01] and in the previous chapter. The proposed fusion algorithm estimates the function $f_{\boldsymbol{c}}$, which allows us to take advantage of this polynomial mapping

$$\boldsymbol{x}_{\mathrm{u}} = f_{\boldsymbol{c}}(T(\boldsymbol{x}_{\mathrm{m}}), \nabla T(\boldsymbol{x}_{\mathrm{m}})^{H} \boldsymbol{u}) \tag{5.6}$$

- A model for the geometric transform T, which can be linear (e.g., affine) or non-rigid (also called elastic) enabling images to be registered with local geometric differences. Non-rigid registration, which is preferred in medical applications, can be defined using radial basis functions (thin-plate or surface splines, multiquadrics, and compactly-supported transformations [CR03, CHH04, RSH+99]), physical continuum models, and large deformation models (diffeomorphisms) [RVW+11]. The model used in this work is detailed in the next section.

5.3.2 Spatial transformation

The geometric transform used for MR/US image registration has to be sufficiently general to account for local non-rigid deformations, but also for large global affine deformations that occur because of the different acquisition setups. Therefore, we consider a transformation T built as a combination of a global affine transformation $T_{\boldsymbol{\theta}}$ and a local B-spline-based transform $T_{\boldsymbol{\phi}}$, in order to map the points in the target MR image to those in the reference US image, i.e.,

$$T = T_{\boldsymbol{\phi}} \circ T_{\boldsymbol{\theta}},$$

where $\circ$ denotes the operator used for the composition of two functions. Note that this combination has been used successfully in many applications, see, e.g., [RSH+99, SKS10]. The two transforms $T_{\boldsymbol{\theta}}$ and $T_{\boldsymbol{\phi}}$ are detailed in the next sections.

1) Affine transformation $T_{\boldsymbol{\theta}}$

A 2D affine model is parametrized by 6 parameters describing the rotation, translation and scaling factor of the reference image compared to the target image. These parameters define the following matrix (homogeneous coordinates)

$$\begin{pmatrix} \theta_{11} & \theta_{12} & \theta_{13} \\ \theta_{21} & \theta_{22} & \theta_{23} \\ 0 & 0 & 1 \end{pmatrix} \tag{5.7}$$

where θ_{ij} are the parameters to be estimated.

2) Non-rigid local transformation $T_{\boldsymbol{\phi}}$

The affine model only captures the global deformations between the two images and is thus not sufficient for MR and US images. Therefore, in this work, we also consider a local non-rigid transformation, denoted as $T_{\boldsymbol{\phi}}$, defined as a B-spline deformation mesh (see, e.g., [RSH+99] for motivations). The basic idea of this model is to deform a pattern by manipulating a mesh of control points, that control the shape of the deformation pattern and ensure smooth and continuous deformation fields. Fig. 5.1 shows a schematic representation of the deformation field generated from the displacement of local control points.

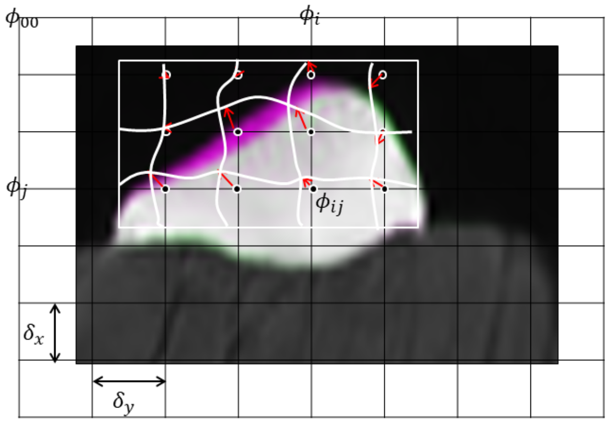

Figure 5.1: Overview of B-spline deformation mesh.

Denote as $\Omega = \{(x, y) \mid 0 \leq x < N,\ 0 \leq y < M\}$ the domain of the image-plane and consider an $n_x \times n_y$ mesh of control points ϕ_{ij} with identical spacing δ, denoted as Φ and shown in Fig. 5.1. The B-spline local transformation is defined as:

$$T_\phi(x, y) = \sum_{m=0}^{3} \sum_{n=0}^{3} B_m\Big(\frac{x}{n_x}\Big) B_l\Big(\frac{y}{n_y}\Big) \phi_{i_x+m, j_y+n}, \tag{5.8}$$

where $i_x = \lfloor\ x/n_x \rfloor - 1$, $j_y = \lfloor y/n_y \rfloor - 1$ and $\lfloor . \rfloor$ is used for the integer part. The cubic B-spline uniform functions considered in this work are defined as:

$$\begin{aligned} B_0(u) &= \frac{(1-u)^3}{6} \\ B_1(u) &= \frac{3u^3 - 6u^2 + 4}{6} \\ B_2(u) &= \frac{-3u^3 + 3u^2 + 3u + 1}{6} \\ B_3(u) &= \frac{u^3}{6}. \end{aligned}$$

Once the grid of the B-spline has been constructed, it is used to deform the local neighborhood of every control point in the MR image. Once the moving image has been deformed, it is compared to the reference image (here, the US image) using the similarity measure defined by the polynomial f_c.

5.3.3 Regularization

This work considers a regularization to smooth the estimated transformation $T_{\boldsymbol{\phi}}$. Indeed, since the registration of MR and US images requires a small spacing mesh, it may lead to B-spline functions that are not sufficiently smooth. The regularization considered in this work is composed of second-order derivatives of $T_{\boldsymbol{\phi}}$:

$$R_{\mathrm{s}}(T_{\boldsymbol{\phi}}) = \int_{\Omega} \Big[\frac{\partial^2 T_{\boldsymbol{\phi}}}{\partial x^2} + \frac{\partial^2 T_{\boldsymbol{\phi}}}{\partial y^2} + \frac{\partial^2 T_{\boldsymbol{\phi}}}{\partial x \partial y}\Big] dxdy. \tag{5.9}$$

In practice, the integral (5.9) (a scalar) is approximated by standard numerical integration providing a discrete time regularization, which will be used in this chapter.

Note that there is no need to regularize the global transform $T_{\boldsymbol{\theta}}$ and that the regularization (5.9) reduces to zero for an affine transformation, therefore, penalizing only non-affine transformations.

5.4 Optimization algorithm for joint fusion and registration

This section details the proposed optimization algorithm used to minimize the cost function (5.5). For a fixed transformation T and a fixed vector $\boldsymbol{c}$, this minimization is clearly easier and can be solved using an algorithm similar to the one developed in Chapter 4. Thus, in order to decouple the optimizations with respect to $\boldsymbol{x}$ and $(T, \boldsymbol{c})$, we introduce a latent vector $\boldsymbol{v} = (v_1, ..., v_N)^T = f\Big(T(\boldsymbol{x}, \nabla T(\boldsymbol{x})^H \boldsymbol{u}\Big)$ leading to the following optimization problem equivalent to (5.5):

$$\begin{aligned}(\hat{\boldsymbol{x}}, \hat{T}, \hat{\boldsymbol{c}}, \hat{\boldsymbol{v}}) = \underset{\boldsymbol{x}, T, \boldsymbol{c}, \boldsymbol{v}}{\operatorname{argmin}} \quad & \frac{1}{2}\|\boldsymbol{y}_{\mathrm{m}} - \boldsymbol{S}\boldsymbol{C}\boldsymbol{x}\|^2 \\ & + \tau_2 \sum_{i=1}^{N} [\exp(y_{\mathrm{u},i} - v_i) - \gamma(y_{\mathrm{u},i} - v_i)] \\ & + \tau_1 \|\nabla \boldsymbol{x}\|^2 + \tau_3 \|\nabla \boldsymbol{v}\|^2 + \tau_5 R_{\mathrm{s}}(T) \\ & + \tau_4 \|\boldsymbol{v} - f_{\boldsymbol{c}}(T, \boldsymbol{x}, \boldsymbol{u})\|^2,\end{aligned} \tag{5.10}$$

where τ_4 is an additional hyperparameter. The proposed algorithm alternates between optimizations with respect to the fused image $\boldsymbol{x}$, the geometric transformation $\boldsymbol{T}$ and the polynomial coefficient vector $\boldsymbol{c}$, which are summarized below and detailed in the following sections.

1. Estimation of the fused image $\boldsymbol{x}$ and the latent vector $\boldsymbol{v}$ for a fixed $(T, \boldsymbol{c})$

$$\begin{aligned}\min_{\boldsymbol{x},\boldsymbol{v}} \quad & \frac{1}{2}\|\boldsymbol{y}_{\mathrm{m}} - \boldsymbol{S}\boldsymbol{C}\boldsymbol{x}\|^2 \\ & + \tau_2 \sum_{i=1}^{N} \Big[\exp(y_{\mathrm{u},i} - \boldsymbol{v}) - \gamma(y_{\mathrm{u},i} - \boldsymbol{v})\Big] \\ & + \tau_1\|\nabla \boldsymbol{x}\|^2 + \tau_3\|\nabla \boldsymbol{v}\|^2 \\ & + \tau_4\|\boldsymbol{v} - f_{\boldsymbol{c}}\Big(T(\boldsymbol{x}, \nabla T(\boldsymbol{x})^H \boldsymbol{u}\Big)\|^2.\end{aligned} \tag{5.11}$$

2. Estimation of the transformation T for a fixed $(\boldsymbol{x}, \boldsymbol{c}, \boldsymbol{v})$ (multimodal registration)

$$\min_{T} \quad \|\boldsymbol{v} - f_{\boldsymbol{c}}\Big(T(\boldsymbol{x}, \nabla T(\boldsymbol{x})^H \boldsymbol{u}\Big)\|^2 + \lambda R_{\mathrm{s}}(T). \tag{5.12}$$

   where $\lambda = \frac{\tau_5}{\tau_4}$

3. Estimation of the vector $\boldsymbol{c}$ associated with the polynomial $f_{\boldsymbol{c}}$ for a fixed $(\boldsymbol{x}, T, \boldsymbol{v})$

$$\min_{\boldsymbol{c}} \quad \|\boldsymbol{v} - f_{\boldsymbol{c}}\Big(T(\boldsymbol{x}, \nabla T(\boldsymbol{x})^H \boldsymbol{u}\Big)\|^2. \tag{5.13}$$

5.4.1 Estimation of the fused image for known (T_c)

Inspired from [EMVB+20], the fusion algorithm is based on the PALM algorithm [BST14], adapted to nonsmooth and nonconvex functions such as the objective function (5.11). The PALM algorithm is designed for minimization of cost functions with two variables $\boldsymbol{x}$ and $\boldsymbol{v}$ that can be written as:

$$\min_{\boldsymbol{x},\boldsymbol{v}} \psi(\boldsymbol{x}, \boldsymbol{v}) := l(\boldsymbol{x}) + g(\boldsymbol{v}) + H(\boldsymbol{x}, \boldsymbol{v}), \tag{5.14}$$

where l and g are convex and continuous functions and H is a non-linear function. In order to apply the PALM algorithm, we introduce the following notations:

$$l(\boldsymbol{x}) = \frac{1}{2}\|\boldsymbol{y}_{\mathrm{m}} - \boldsymbol{S}\boldsymbol{C}\boldsymbol{x}\|_2^2 + \tau_1\|\nabla \boldsymbol{x}\|^2 \tag{5.15}$$

$$g(\boldsymbol{v}) = \tau_2 \sum_i [\exp(y_{\mathrm{u},i} - v_i) - \gamma(y_{\mathrm{u},i} - v_i)] + \tau_3\|\nabla \boldsymbol{v}\|^2 \tag{5.16}$$

$$H(\boldsymbol{x}, \boldsymbol{v}) = \tau_4 \sum_{i=1}^{N} \Big(v_i - \sum_{p+q \leq 3} c_{pq} T(x_i^p)(\nabla T(\boldsymbol{x})^H \boldsymbol{u})_i^q \Big). \tag{5.17}$$

Note that this choice of functions fulfills all the assumptions required by PALM [BST14]:

1. l and g are bounded ($\inf_{\mathbb{R}^N}(f) > -\infty$ and $\inf_{\mathbb{R}^N}(g) > -\infty$).
2. For any fixed $\boldsymbol{v}$, the function $\boldsymbol{x} \mapsto H(\boldsymbol{x}, \boldsymbol{v})$ is $C^{1,1}$, and the partial gradient $\nabla_{\boldsymbol{x}} H(\boldsymbol{x}, \boldsymbol{v})$ is globally Lipschitz.
3. For any fixed $\boldsymbol{x}$, the function $\boldsymbol{v} \mapsto H(\boldsymbol{x}, \boldsymbol{v})$ is $C^{1,1}$, and the partial gradient $\nabla_{\boldsymbol{v}} H(\boldsymbol{x}, \boldsymbol{v})$ is globally Lipschitz.
4. ∇H is Lipschitz continuous function in the image domain.

The alternate optimization with respect to the two vectors $\boldsymbol{x}$ and $\boldsymbol{v}$ proposed in [BST14] generates a sequence $\{(\boldsymbol{x}^k, \boldsymbol{v}^k)\}_{k \in \mathbb{N}}$ using the following steps:

Step 1: Choose $\gamma_1 > 1$, set $c_k = \gamma_1 L_{\boldsymbol{x}}(\boldsymbol{v}^k)$ and update $\boldsymbol{x}^k$

$$\boldsymbol{x}^{k+1} = \text{prox}_{c_k}^{l} \Big(\boldsymbol{x}^k - \frac{1}{c_k} \nabla_{\boldsymbol{x}} H(\boldsymbol{x}^k, \boldsymbol{v}^k) \Big), \tag{5.18}$$

where $L_{\boldsymbol{x}}(\boldsymbol{v}^k)$ is the Lipschitz constant of $\boldsymbol{x} \mapsto \nabla_{\boldsymbol{x}} H(\boldsymbol{x}, \boldsymbol{v}^k)$ and $\boldsymbol{v}^k$ is the value of $\boldsymbol{v}$ at iteration $\#k$. The proximal operator providing $\boldsymbol{x}^{k+1}$ in (5.18) can be computed using straightforward computations (minimization of the sum of quadratic functions), that is,

$$\boldsymbol{x}^{k+1} = \underset{\boldsymbol{x}}{\text{argmin}} \quad \frac{1}{2}\|\boldsymbol{S}\boldsymbol{C}\boldsymbol{x} - \boldsymbol{y}_{\text{m}}\|^2 + \tau_1 \|\nabla \boldsymbol{x}\|^2 + \frac{L_{k+1}}{2} \|\boldsymbol{x} - (\boldsymbol{x}^k - \frac{1}{L_{k+1}} \nabla_{\boldsymbol{x}} H(\boldsymbol{x}^k, \boldsymbol{v}^k))\|^2, \tag{5.19}$$

where l has been defined in (5.15) and L_{k+1} is the Lipschitz constant of $\boldsymbol{x} \mapsto \nabla_{\boldsymbol{x}} H(\boldsymbol{x}, \boldsymbol{v}^{k+1})$ at iteration $\#(k+1)$. This minimization problem can be solved using an analytical solution, computed in the Fourier domain.

Step 2 : Choose $\gamma_2 > 1$, set $d_k = \gamma_2 L_{\boldsymbol{v}}(\boldsymbol{x}^k)$ and update $\boldsymbol{v}^k$ as follows

$$\boldsymbol{v}^{k+1} = \text{prox}_{d_k}^{g} \Big(\boldsymbol{v}^k - \frac{1}{d_k} \nabla_{\boldsymbol{v}} H(\boldsymbol{x}^k, \boldsymbol{v}^k) \Big),$$

where $L_{\boldsymbol{v}}(\boldsymbol{x}^k)$ is the Lipschitz constant of $\boldsymbol{v} \mapsto \nabla_{\boldsymbol{v}} H(\boldsymbol{x}^k, \boldsymbol{v})$ and $\boldsymbol{x}^k$ is the value of $\boldsymbol{x}$ at iteration $\#k$. A gradient descent algorithm with backtracking line search is used to update $\boldsymbol{v}$, since the function to minimize is convex and differentiable. More precisely, $\boldsymbol{v}^{k+1}$ comes:

$$\begin{aligned} \boldsymbol{v}^{k+1} = \underset{\boldsymbol{v}}{\operatorname{argmin}} \quad & \tau_2 \sum_i [\exp(y_{\mathrm{u},i} - v_i) - \gamma(y_{\mathrm{u},i} - v_i)] \\ + \tau_3 \|\nabla \boldsymbol{v}\|^2 + & \frac{d_k}{2} \|\boldsymbol{v} - (\boldsymbol{v}^k - \frac{1}{d_k} \nabla_{\boldsymbol{v}} H(\boldsymbol{x}^{k+1}, \boldsymbol{v}^k))\|^2, \end{aligned} \tag{5.20}$$

where g has been defined in (5.16) and $d_k = L_{\boldsymbol{v}}(\boldsymbol{x}^k)$ is the Lipschitz constant of $\nabla_{\boldsymbol{v}} H$ at iteration $\#k$. Note that the hyperparameter τ_4 has been included in the function H.

5.4.2 Estimation of the spatial transformation

The estimation of the parameters defining the transformations $T_{\boldsymbol{\theta}}$ and $T_{\boldsymbol{\phi}}$ in (5.7) and (5.8) (multimodal registration) is achieved by minimizing the cost function (5.12) in two steps:

1. In the first step, the local transform $T_{\boldsymbol{\phi}}$ is assumed to be the identity and we estimate the 6 parameters of the global affine transformation $T_{\boldsymbol{\theta}}$ by solving the following optimization problem (with respect to θ) with respect to $\boldsymbol{\theta}$:

$$\widehat{\boldsymbol{\theta}} = \underset{\boldsymbol{\theta}}{\operatorname{argmin}} \quad \|\boldsymbol{v}^k - f_{\boldsymbol{c}}\Big(T_{\boldsymbol{\theta}}(\boldsymbol{x}^k), \nabla T_{\boldsymbol{\theta}}(\boldsymbol{x}^k)^H \boldsymbol{u}\Big)\|^2. \tag{5.21}$$

2. Once the global transform $T_{\boldsymbol{\theta}}$ has been estimated, the second step estimates the local transformation $T_{\boldsymbol{\phi}}$ by solving the following problem (with respect to $\boldsymbol{\phi}$):

$$\widehat{\boldsymbol{\phi}} = \underset{\boldsymbol{\phi}}{\operatorname{argmin}} \quad \|\boldsymbol{v}^k - f_{\boldsymbol{c}}\Big(T_{\boldsymbol{\phi}} \circ T_{\boldsymbol{\theta}}(\boldsymbol{x}^k), \nabla T_{\boldsymbol{\phi}} \circ T_{\boldsymbol{\theta}}(\boldsymbol{x}^k)^H \boldsymbol{u}\Big)\|^2 + \lambda R_{\mathrm{s}}(T_{\boldsymbol{\phi}}). \tag{5.22}$$

Both optimizations are conducted using the Broyden-Fletcher-Goldfarb-Shanno (BFGS) algorithm [HZ85] (a quasi-Newton method using an approximation of the Hessian matrix).

5.4.3 Estimation of the polynomial function

For a known degree d, the polynomial function $f_{\boldsymbol{c}}$ to be estimated is defined by $N_d = (d+1)(d+2)/2$ coefficients collected in the vector $\boldsymbol{c}_d = \{c_{pq} \mid p+q \leq d\}$. We estimate these coefficients, by solving the problem (5.13) which leads to the least-squares estimator:

$$\hat{\boldsymbol{c}}_d = (\boldsymbol{A}_m^T \boldsymbol{A}_m)^{-1} \boldsymbol{A}_m^T \boldsymbol{v}, \tag{5.23}$$

where $\boldsymbol{A}_m \in \mathbb{R}^{N \times N_d}$ is a matrix whose elements are $T(x_i)^p (\nabla T(x)^H u)_i^q$ for $p+q \leq d$.

5.4.4 Proposed algorithm

The proposed MR and US image fusion and registration method is summarized in Algo. 2.

Algorithm 2: Proposed MR and US image fusion algorithm.

```
Input $\boldsymbol{y}_{\mathbf{u}}$, $\boldsymbol{y}_{\mathbf{m}}$, $\boldsymbol{S}$, $\boldsymbol{C}$, $\tau$, $\lambda$, $\mu$
0 - Initialization of $x$, $v$, $T$ and $c$
REPEAT
1 - Find the smallest nonnegative integers $i_k$ such that
        $\psi(p_{\bar{L}}(\boldsymbol{x^k}), \boldsymbol{v^k}) \leq Q_{\bar{L}}(p_{\bar{L}}(\boldsymbol{x^k}), \boldsymbol{x^k}, \boldsymbol{v^k})$
with $\bar{L} = \gamma^{i_k} L_k$. Set $L_{k+1} = \gamma^{i_k} L_k$ and update $\boldsymbol{x}$ using (5.19).
2 - Set $d_k = L_{\boldsymbol{v}}(\boldsymbol{x}^{k+1}) = 2\tau_4$ and update $\boldsymbol{v}$ using (5.20).
3 - Update $T_{\boldsymbol{\theta}}$ using (5.21).
4 - Update $T_{\boldsymbol{\phi}}$ using (5.22).
5 - Update $\hat{\boldsymbol{c}}_d$ using (5.23).

Until the number of iteration $k$ reaches $k = 30$
Output: Fused image $T(\boldsymbol{x})$
```

5.4.5 Performance measures

The performance of the proposed joint registration and fusion algorithm is evaluated by visual inspection and by using the following quantitative metrics: the root mean square error (RMSE), the peak signal-to-noise ratio (PSNR), the improved signal-to-noise ratio (ISNR) and the mean structural similarity (MSSIM). The mutual information (MI) is also used to evaluate the accuracy of the registration. The definitions of the different metrics are provided as follows:

$$\begin{aligned}
&\mathrm{RMSE} = \sqrt{\frac{1}{N}\|\hat{\boldsymbol{x}} - \boldsymbol{x}\|_2^2}, \quad \mathrm{PSNR} = 20\log_{10}\frac{\max(\hat{\boldsymbol{x}}, \boldsymbol{x})}{\mathrm{RMSE}}\\
&\mathrm{ISNR} = 10\log_{10}\frac{\|\boldsymbol{y} - \boldsymbol{x}\|}{\|\hat{\boldsymbol{x}} - \boldsymbol{x}\|^2}, \quad \mathrm{MI} = \sum_{i,j} p_{y\hat{y}}(i,j)\log\frac{p_{y\hat{y}}(i,j)}{p_y(i,.)p_{\hat{y}}(.,j)}\\
&\mathrm{MSSIM} = \frac{1}{M}\sum_{m=1}^{M}\mathrm{SSIM}(\boldsymbol{x}_m, \hat{\boldsymbol{x}}_m),
\end{aligned} \tag{5.24}$$

where $\boldsymbol{x}$ is the ground truth MR image, $\hat{\boldsymbol{x}}$ denotes the estimated image, the index m in the definition of MSSIM indicates a patch extracted from the corresponding images, $\boldsymbol{y}$ and $\hat{\boldsymbol{y}}$ are the US image and the registered MR image, and p_y, $p_{\hat{y}}$ are the marginal distributions of $\boldsymbol{y}$ and $\hat{\boldsymbol{y}}$, and $p_{y\hat{y}}$ is the joint bivariate distribution of $(\boldsymbol{y}, \hat{\boldsymbol{y}})$. Note that the distributions p_y, $p_{\hat{y}}$ and $p_{y\hat{y}}$ are practically obtained by computing the corresponding normalized histograms. Note also that the aspect of the fused image is compared to both a high-resolution enhanced MR image (estimated using the algorithm of [GEW10]) and a despeckled US image (estimated using the algorithm of [AB07b]). To ensure a fair comparison, the algorithms studied in [GEW10] and [AB07b] were adapted to be used with the forward models in (1) and the noise assumptions detailed in Section I.

The performance of the proposed method is also evaluated using two quantitative measures that do not require the knowledge of the ground truth images, which is interesting for experimental data: the contrast to noise ratio (CNR) and the slope of image profiles [MBBK15]. The CNR is classically used to evaluate the contrast between two patches extracted from two different structures in the examined tissue. It is defined by

$$\mathrm{CNR} = \frac{|\mu_1 - \mu_2|}{\sqrt{\sigma_1^2 + \sigma_2^2}} \tag{5.25}$$

where μ_1, μ_2, are the means of the two patches, and σ_1 and σ_2 are their standard deviations. The second metric evaluates the spatial resolution of the different restored images. It considers image profiles crossing the boundaries between distinct interfaces. The slope of these profiles at the interface between two structures can be used as an indicator of the spatial resolution.

Table 5.1: Quantitative performance measures for simulated data (F, SR and D stand for fused, super-resolved MR and despeckled images).

	Computed from images in Fig. 5.2			
	F vs MR	SR vs MR	F vs US	D-US vs US
RMSE	0.24	0.30	0.17	0.29
PSNR [dB]	17.51	15.84	20.74	16.17
ISNR [dB]	1.67	1.21	7.64	3.07
MSSIM [dB]	0.93	0.89	0.94	0.29

5.4.6 Simulation results on synthetic data

To demonstrate the efficiency of the proposed joint fusion and registration method, this section first considers a set of synthetic images with known ground truth. The MR observation image in Fig. 5.2(b) corresponds to a deformed, blurred, decimated and noisy version of the ground truth MR image in Fig. 5.2(a). The MR image was contaminated by an additive white Gaussian noise with variance $\sigma_m^2 = 4$ (SNR = 24dB), the decimation factor was $s = 6$ in each spatial direction and the blurring kernel is a Gaussian filter of size 9×9 with standard deviation $\sigma = 5$. Finally, a spatial deformation combining elastic B-spline and global affine transformations was used to obtain the observed MR image in Fig. 5.2(b). The simulated US image in Fig. 5.2(c) was generated by applying a polynomial of degree 4 to the gray levels of the MR image and by adding a log-Rayleigh noise with an SNR of 13.80 dB.

The fused image obtained using the proposed method is presented in Fig. 5.2(d). This result clearly shows the interest of the fused image (compared to the MR and US images), which contains all the significant information from both MR and US images. Specifically, the fused image is not affected by US speckle and MR blur, provides well-defined contours and good contrast compared to the native MR and US images. Note that it is not possible to observe registration errors in the fused image, which confirms the success of the multimodal registration. The estimated local transformation T_ϕ and the corresponding ground truth deformation field are superimposed in Fig. 5.2(e), confirming

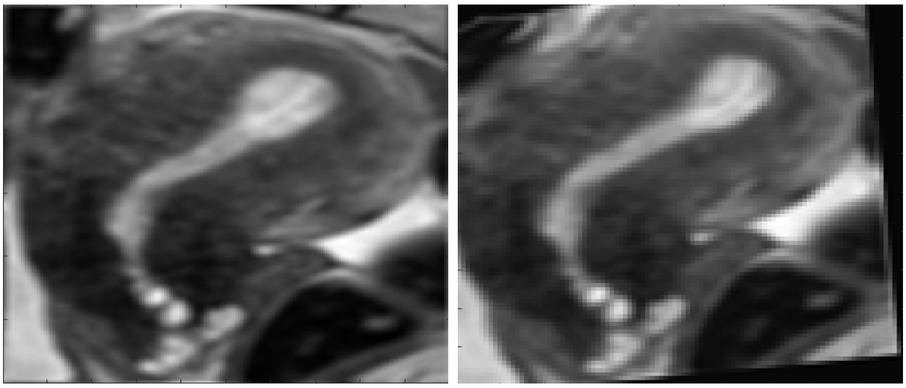

(a) Ground truth MR (b) MR observation

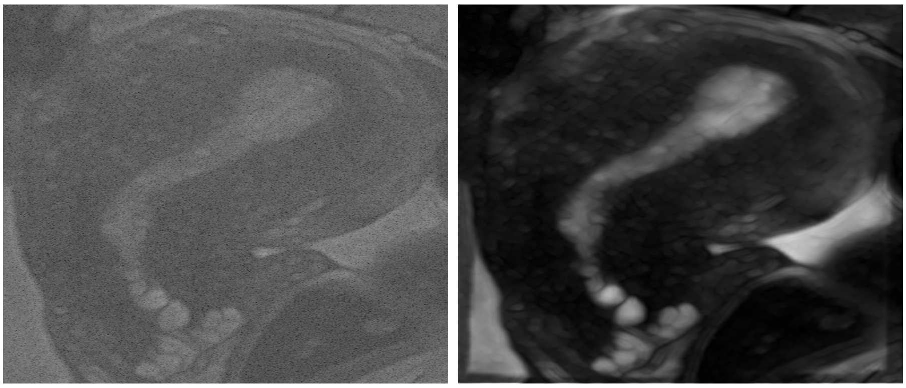

(c) US observation (d) Fused image

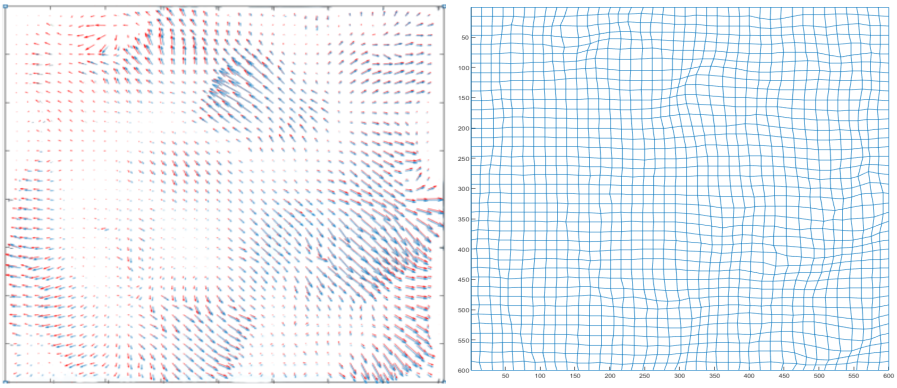

(e) B-spline transformation (f) Local transformation field

Figure 5.2: Joint fusion and registration of simulated US and MR images: (a) ground truth MR image, (b) observed MR image, (c) US image, (d) fused image obtained using the proposed method, (e) ground truth elastic deformation field (in red) and B-spline estimated transformation (in blue), (f) to be compared with the estimates using the B-splines (local transformation).

the accuracy of this registration.

Quantitative results corresponding to the images in Fig. 5.2 are shown in Table 5.1 and confirm the interest of the proposed fusion method. Table 5.2 shows quantitative results in terms of mutual information, computed between the US image and the registered and non-registered MR images. The mutual information increases significantly after registration, confirming the efficiency of the registration step.

Table 5.2: Mutual information between the US image $\boldsymbol{x}_{\mathrm{u}}$ and the registered $T(\boldsymbol{x}_{\mathrm{m}})$ and non-registered $(\boldsymbol{x}_{\mathrm{m}})$ MR images.

	Mutual Information	
	$\mathrm{MI}[\boldsymbol{x}_{\mathrm{u}}, T(\boldsymbol{x}_{\mathrm{m}})]$	$\mathrm{MI}[\boldsymbol{x}_{\mathrm{u}}, \boldsymbol{x}_{\mathrm{m}}]$
Simulated image (Fig. 5.2)	0.82	0.16
EXP 1 (Fig. 5.3)	4.59	2.01
EXP 2 (Fig. 5.4)	1.81	0.83

5.4.7 Experimental results on phantom data

The proposed MR/US image fusion and registration algorithm was validated on experimental phantom data. The phantom was made of a beaf steak glued to a cryogel (PVC) structure and designed to mimic uterus and endometrium responses to MR and US imaging. More details about the experimental model design and image acquisition can be found in [VMKB19]. Figs. 5.3(a,b) and 5.4(a,b) show two different views of the observed MR and US images. To mitigate the relatively good SNR obtained due to the phantom design, the US image was further degraded by log-Rayleigh noise as presented in Figs. 5.3(d) and 5.4(d). The MR image in the first experiment referred to as exp. 1 (Fig. 5.3(c)) was cropped and deformed. The MR observation in the second experiment referred to as exp. 2 (Fig. 5.4(c)) is only cropped since we can already distinguish a non-rigid transformation caused by the image acquisition. Three main structures can be observed in these images (as shown in Fig. 5.3(b)): a PVC phantom (bright structure in the MR image), a piece of beef meat (gray

(a) Ground truth MR (b) Ground truth US (c) MR acquisition

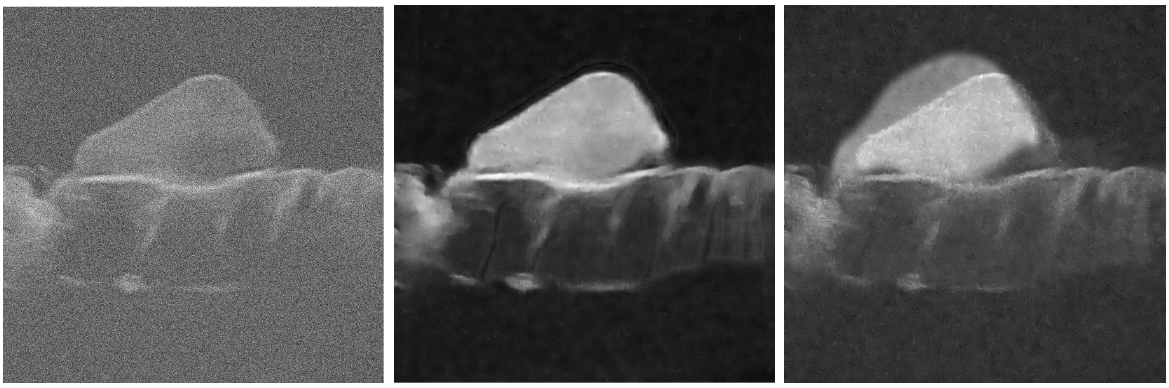

(d) US acquisition (e) Fused image (f) Fused image using Algo. 1

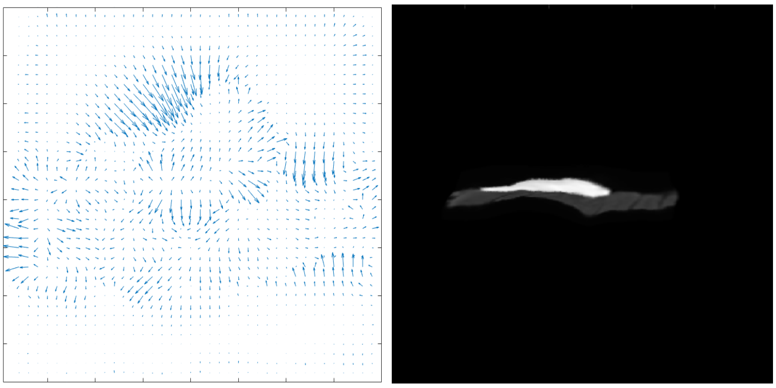

(g) Local transformation field (h) Registered MR using [RSH+99]

Figure 5.3: Joint fusion and registration of US and MR images: (a) Ground truth MR image, (b) Ground truth US image, (c) Deformed MR image, (d) US image, (e) Fused image using the proposed method, (f) Fused image using Algo. 1, (g) B-spline estimated transformation field, (h) Registered MR minimizing the cost function (5.1) (without performing any fusion).

(a) MR acquisition (b) US acquisition (c) MR observation

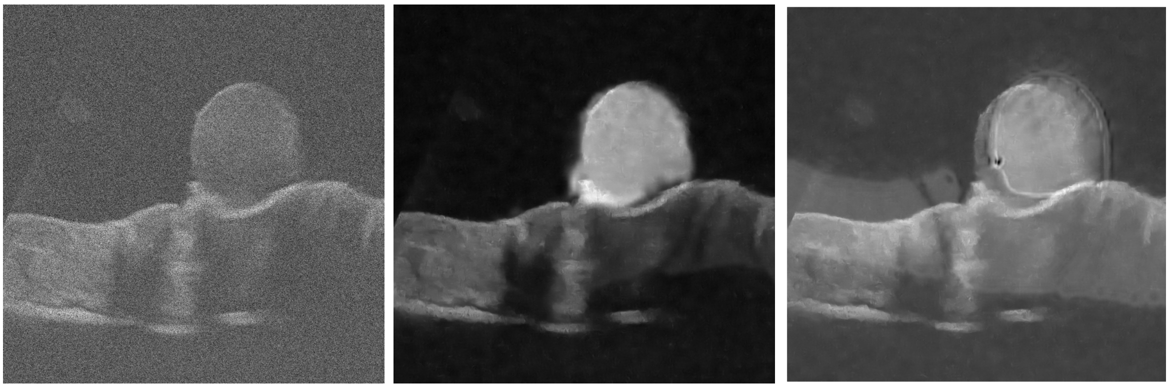

(d) US observation (e) Fused image (f) Fused image using Algo. 1

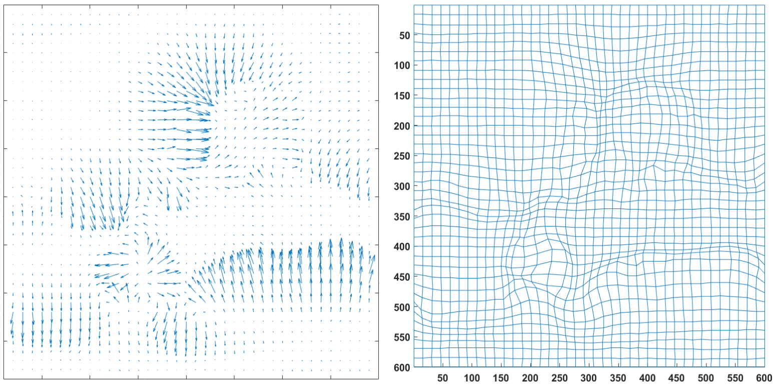

(g) B-spline transformation (h) Local transformation field

Figure 5.4: US and MR joint fusion and registration: (a) Ground truth MR image, (b) Ground truth US image, (c) Deformed MR observation, (d) US observation, (e) Fused image using the proposed method, (f) Fused image using Algo. 1, (g) B-spline estimated transformation field, (h) Mesh-grid B-spline transformation.

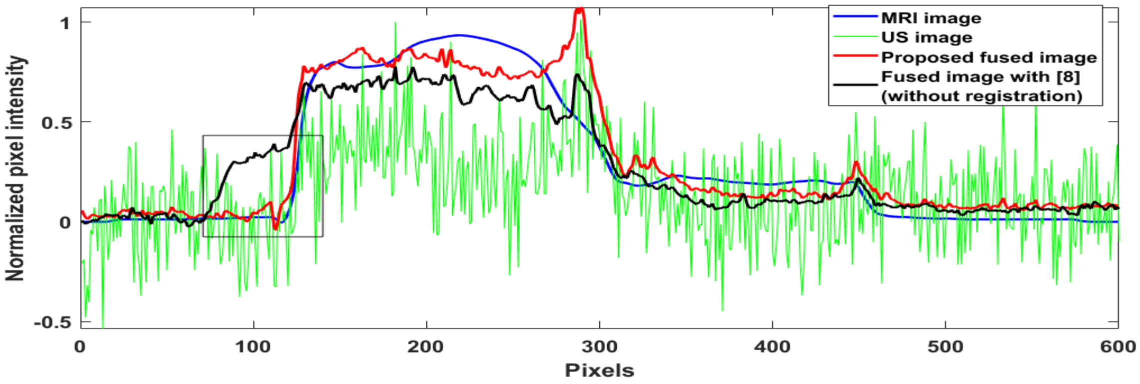

(a)

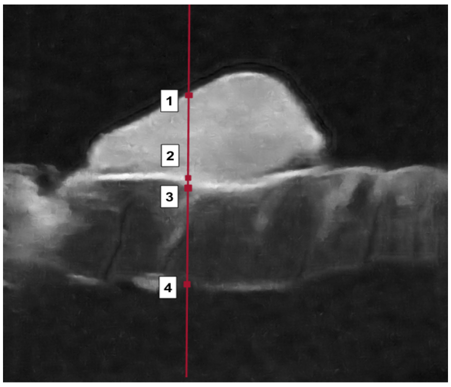

(b)

Figure 5.5: (a) displays normalized pixel intensities of extracted lines from MR, US and fused images that are estimated with the proposed algorithm (Fig. (5.3) (e)) and with the algorithm of the previous chapter (neglecting registration errors) in (Fig. (5.3) (f)). The MR observation is in blue, the US observation is in green, the fused image using the proposed algorithm is in red and the fused image using Algo. 1 is in black. The vertical straight line in (b) indicates where the profiles were extracted from.

structure in the MR image), and the glue used to attach them, only visible in the US image (thin bright structure).

Figs. 5.3(e,f) and 5.4(e,f) show the fused images obtained using the proposed method and the algorithm in Chapter 4 (Algo. 1). The fused images in Figs. 5.3(e) and 5.4(e) gather information from MR and US images: they provide a good contrast between the PVC and the beef tissue (similar to MR), a good spatial resolution (similar to US) allowing small structures such as the glue to be distinguished, and good SNR. Moreover, registration errors are significantly reduced in the fused and registered images when compared to the fused and unregistered images of Figs. 5.3(f) and 5.4(f) obtained using the Algo. 1 . The performance of the proposed algorithm compared to Algo. 1 confirms the interest of a joint fusion and registration. Figs. 5.3(g) and 5.4(g) display the estimated B-spline local transformation, which has been compensated in the proposed algorithm. Fig. 5.3(h) was obtained using the same multimodal registration algorithm as the one embedded in the proposed method. It clearly fails to register MR to the US image, because of its sensitivity to noise and to mismatching between the gray levels in the two imaging modalities. Finally, the efficiency of the registration step included in the proposed algorithm is confirmed by the values of MI shown in Table 5.2. Figs 5.3(a-d) and 5.4(a-d) show the MR and US observations, which clearly highlight the complementarity between the two imaging modalities: MR has a large field of view with excellent contrast between the polyvinyl alcohol and the beef steak with a limited spatial resolution especially at millimetric scale (it is impossible to observe the glue among the steak and the PVA). On the other hand, the US image has a good resolution that allows the glue to be imaged very precisely (mimicking the endomotrium depth of inflitration), but has a reduced field of view. The fused images obtained using Algo. 2 are presented in Figs. 5.3(e) and 5.4(e). The interest of fusing the two images can be appreciated, in particular the ability of the fused image to gather the good contrast of MR and the good spatial resolution of US. In addition to the visual examination of the different images, CNR was used to assess the contrast between two different structures of the images. The two patches considered to compute the CNR are extracted from the PVA phantom and the beef steak. Table 5.3 clearly demonstrates that the joint registration/fusion process improves the image contrast in both experiments compared to US images.

Table 5.3: Contrast to noise ratio (CNR) for experimental data.

	CNR		
	MR image	US image	Fused image
EXP 1 (Fig. 3)	40.25 dB	7.34 dB	33.31 dB
EXP 2 (Fig. 4)	58.20 dB	4.83 dB	30.92 dB

The spatial resolution of MR, US and the fused images was evaluated using the slope (see Fig. 5.5), of the image profiles crossing the boundaries between different structures. Table 5.4 summarizes the improvement of the resolution resulting from the fusion compared to the MR image.

Table 5.4: Profile slopes of the boundaries between different regions of interest in the MR, US and fused images (FI), that correspond to the vertical line in Fig. 5.5.

	MR ($\times 10^{-2}$)	US ($\times 10^{-2}$)	FI ($\times 10^{-2}$)
Slope #1	2.29	4.40	3.28
Slope #2	-0.03	8.71	6.51
Slope #3	2.62	3.44	3.71
Slope #4	-0.61	-1.05	-0.76

5.4.8 Hyperparameters

The proposed algorithm requires to adjust 5 hyperparameters denoted as τ_i for $i = 1, ..., 5$:

- τ_1 balances the weight between the MR data fidelity term and the TV regularization. Considering that TV promotes a piece-wise constant fused image, increasing τ_1 decreases the resolution of the fused image, which is measured using slope interfaces (see Fig. 5.5). When τ_1 exceeds 5.10^{-2}, Fig. 5.6 shows that the slope of the interface #2 starts to decrease and the resulting fused image is blurred. Thus, hyperparameter τ_1 should belong to the interval $[5 \times 10^{-3}, 10^{-1}]$ for this example.

- τ_3 has the same effect as τ_1 on the fused image and should be adjusted similarly see Fig. 5.8.

- τ_5 is a regularization parameter that defines the compromise between the similarity of the registered MR and US images and the smoothness of the B-spline transformation.

- The choice of hyperparameter τ_4 can be conducted as follows: when τ_4 has a low (resp. high) value, the fused image is close to the high-resolution MR image (resp. the US image). Thus, τ_4 should be fixed between these two values in order to ensure appropriate denoising (via the value of CNR) and a good resolution (via the values of interface slopes). Fig. 5.9 shows that $\tau_4 = 10^{-5}$ is a reasonable value for this hyperparameter.

- τ_2 has similar effect as τ_4 on the fused image (see Fig. 5.7).

The values of the regularization parameters can also be chosen after visual inspection of the fused image using the performance measures studied in Section 5.4.5. All the experiments presented in this chapter were obtained with $\tau_1 = 10^{-2}, \tau_2 = 3.10^{-6}, \tau_3 = 2.10^{-4}, \tau_5 = 1.62$ and $\tau_4 = 10^{-5}$.

5.5 Conclusions

This chapter presented a new joint registration and fusion method for MR and US images. This method estimates the transformation relating the two images allowing registration errors to be mitigated. It also provides an enhanced image with respect to MR and US images containing significant

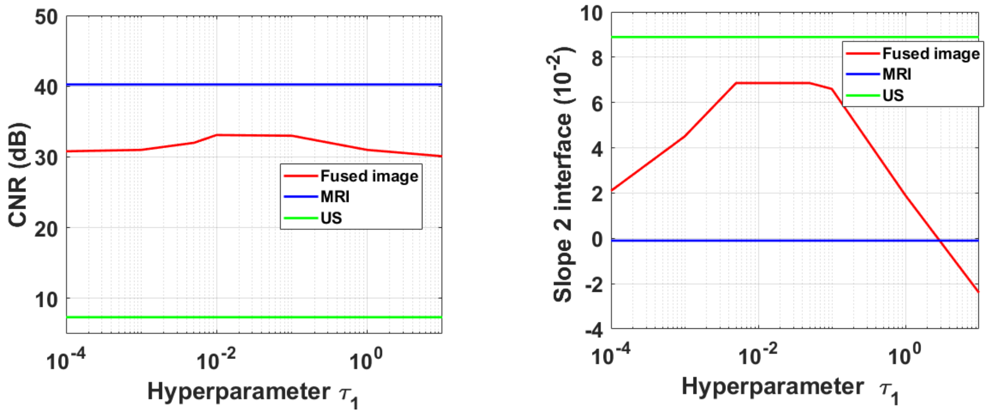

Figure 5.6: Influence of the hyperparameter τ_1 on the fused image. (a) CNR versus τ_1 (b) Slope of interface #2 versus τ_1.

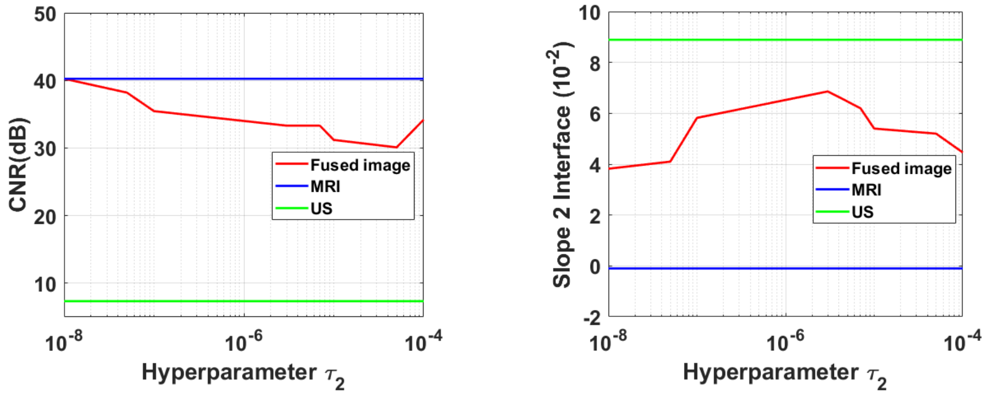

Figure 5.7: Influence of the hyperparameter τ_2 on the fused image. (a) CNR versus τ_2 (b) Slope of interface #2 versus τ_2.

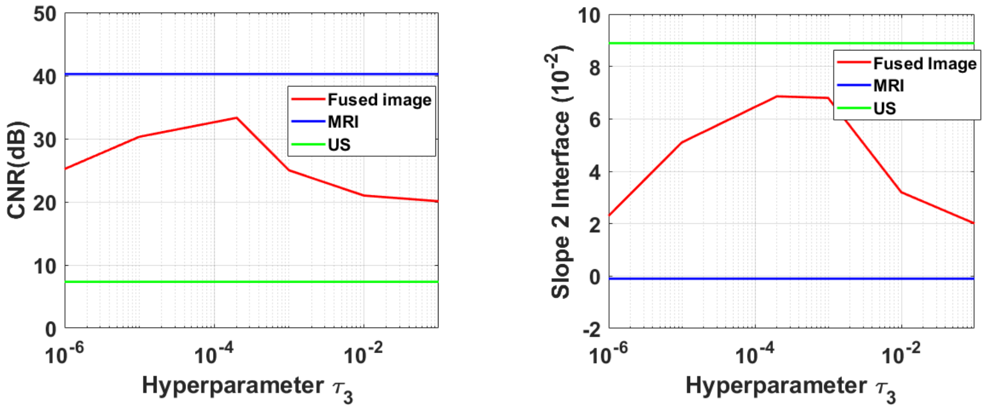

Figure 5.8: Influence of the hyperparameter τ_3 on the fused image. (a) CNR versus τ_3 (b) Slope of interface #2 versus τ_3.

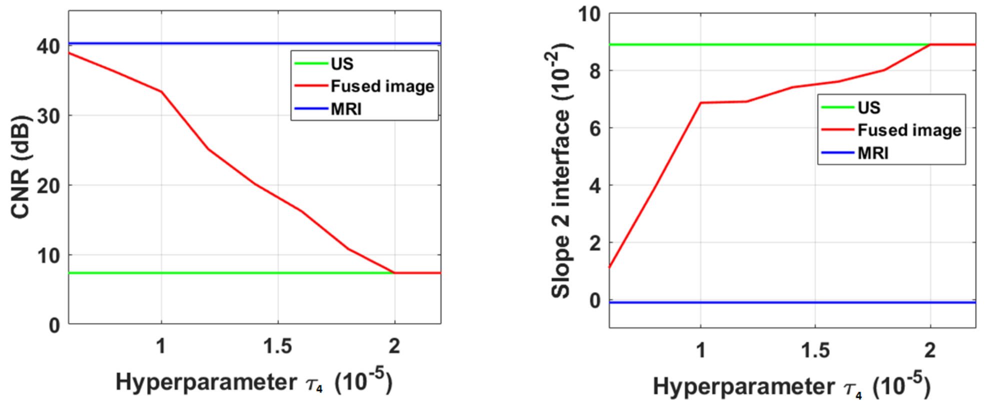

Figure 5.9: Influence of the hyperparameter τ_4 on the fused image. (a) CNR versus τ_4 (b) Slope of interface #2 versus τ_4.

information from both modalities. The key ingredients of the proposed method include the resolution of two inverse problems, ensuring a despeckling of the US image and a super-resolution of the MR, the use of a polynomial function relating the noiseless US and MR images and the consideration of local and global transformations in order to correct the registration errors. All these ingredients are incorporated in PALM algorithm, allowing the joint fusion and registration problem to be solved. Quantitative and qualitative results obtained with different datasets show very promising results for synthetic and phantom data. Future work will be dedicated to confirm the encouraging phantom results on *in vivo* data.

Chapter 6

Conclusions and perspectives

6.1 Conclusions

The objective of this PhD thesis was to investigate algorithms for the fusion of MRI and ultrasound images for the pre-operative diagnosis and the imaging guided-surgery of endometriosis. This fusion is a difficult task since MRI and US images are very different modalities that are contaminated by different kinds of noises. Our main contributions concerning the fusion of MRI and US images are summarized below:

The first work studied in Chapter 4 proposed a new fusion method for registered magnetic resonance (MR) and ultrasound (US) images. The proposed method was able to reconstruct a fused image containing information from both observations, by solving a super-resolution inverse problem for MRI and a despeckling problem for US images. These two problems were solved jointly by using appropriate statistical models and a polynomial relationship between the images of interest. The relation between MR and US images was modeled locally by two types of polynomial functions : a global polynomial function and a low-order polynomial functions associated with the image patches. A PALM algorithm was finally investigated to solve the resulting fusion problem. Results obtained on simulated and real images clearly showed the interest of combining the information contained in these two imaging modalities, instead of restoring them independently.

Results show that the patch-wise fusion method captures more details than the global polynomial fusion. However, it is more time consuming. Thus, the choice of the adapted method depends on the application. We would like to mention that these methods suppose that MRI and US images are perfectly registered, otherwise it is necessary to use the algorithm of Chapter 5 which is more efficient but at the price of a higher computational cost.

Chapter 5 presented a new joint registration and fusion method for MR and ultrasound images. This method estimates the transformation relating the two images allowing registration errors to be mitigated. It also provides an enhanced image with respect to MR and ultrasound images containing significant information from both modalities. The key ingredients of the proposed method include also the resolution of two inverse problems, ensuring a despeckling of the US image and a super-resolution of the MRI, the use of a polynomial function relating the noiseless ultrasound and MR images and the consideration of local and global transformations in order to correct the registration errors. All these ingredients are incorporated in PALM algorithm, allowing the joint fusion and registration problem to be solved. Quantitative and qualitative results obtained with different datasets show very promising results for synthetic and phantom data.

6.2 Future work

To the best of our knowledge, this work is a first attempt for fusing MR and US images. It opens several interesting perspectives.

6.2.1 Short-term perspectives

- **Observation models:** As a matter of simplicity and since the fusion is a complex and non-linear task, we choose the hypothesis of an independent identically distributed noise in both MRI and US images. A natural progression of this work is to take into account the possible correlation of noise samples especially for the US image, to take into account the presence of potential artifacts and to adapt the algorithm to not-fully developed speckle as in [DJ08].

- **Regularizations:** It is well known that inverse problems are ill-posed, which is a reason why we proposed to use an l_2-TV regularization to smooth MRI and US images. Other regularizers have been proposed in the literature that might improve the proposed fusion: [BEGR09] introduced a novel regularization adapted to MRI that combines an l_1-TV and Gaussian mixture regularization, [JB18] proposed a non-local total bounded variational (TBV) regularization to restore US images corrupted with data-correlated speckles and linear blurring artifacts. Such regularizations may lead to significant improvement of edge definition for the fused image compared to l_2-TV regularization that can over-smooth the edges.

- **Hyperparameters:** As explain in Chapters 4 and 5, hyperparameters play an important role in the obtained fused images. The choice of hyperparameters was done manually based on visual inspection of images and using appropriate metrics. However, it would be interesting to investigate some methods to tune these hyperparameters automatically from the data as the SURE algorithm [PSC$^+$16] or other Bayesian methods.

- **MRI and US relationship:** The key of an accurate image fusion is the choice of an adapted function that can model a realistic relationship between images. In this work, we choose global or patch-wise polynomial functions to link MRI and US images. An interesting prospect would be to introduce more general transformations resulting for instance from kernel methods (see [MZY15] for an example on point clouds) or to learn the functional dependence between MR and US images using machine learning algorithms as in [KS19].

- **3D image fusion and registration:** All the methods studied ion this work are restricted to 2D images. In order to use these techniques clinically would be important to adapt these methods for the fusion of 3D-MRI and 2D/3D US images.

6.2.2 Long-term perspectives

- **Augmented reality:** The fusion of 2D MRI and US images is a first step in a long study that aims to create a virtual navigator based on augmented reality for endometriosis surgery. The purpose of this study is to combine the fused MRI/US images that can provide a see-through organs and the videos collected during laparoscopy using a small camera that shows only the wall of organs. Combining these information can help to build an augmented reality of real-time organ states. Augmented reality can help surgeons to become more efficient and would change the life of many women.

- **Other medical applications:** There are other applications that use MRI and US images such as prostate biopsy [NKS$^+$09], tumor detection in the liver [KZW$^+$12] and brain shift correction

[GLP01]. It would be interesting to investigate the potential use of the methods studied in this PhD thesis to these new applications.

Appendices

APPENDIX A

Design of a pelvic phantom for MR/US fusion

This appendix is adapted from the conference article [VMKB19]

A.1 Phantom design

The purpose of this phantom is to imitate the uterus tissue that is infiltrated by an endometrioma, it eases the registration of MRI and ultrasound images and unable the fusion method (proposed in chapter 4) to be directly tested in real data. Fig. A.1 shows the layers that compose the uterus: the endometrium, myometrium, and serosa. The myometrium is the thicker layer and mostly consists of smooth muscle fibers. In order to mimic this uterus, a piece of beefsteak of size 17 × 10 × 1.5cm seems to be adapted because of its muscular component.

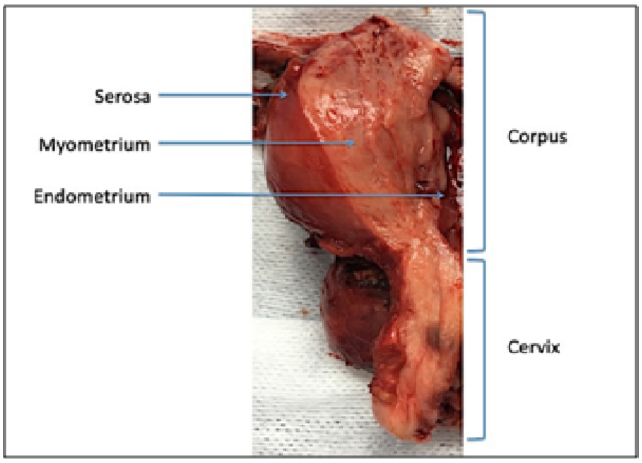

Figure A.1: Uterus specimen demonstrating successive layers of the wall [VMKB19]

Ovarian endometriosis or endometrioma is richly supplied with blood. To imitate this cyst, one can use cryogel based on a mixture of 10% of polyvinyl acid, 89% of deionized water, and 1% silica powder. PVA is boiled in hot water 100 gradually at intensive magnetic stirring (500 to 700 rpm). Then, after its dissolution, the silica is added. The preparation of this mixture takes approximately one hour.

The mixture rest of another hour in room temperature and then transferred into a spheroidal plastic mold that measures 4.3 × 3 × 1.5 cm.

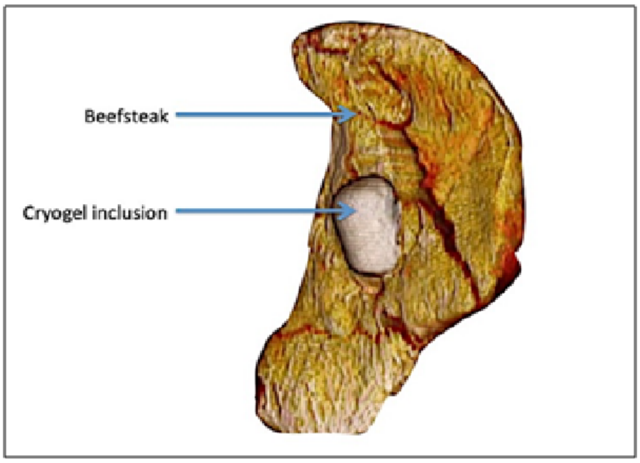

Figure A.2: Representation obtained from MRI 3D reconstruction of the customized phantom

Finally, after solidification of the prepared mixture, it is stuck to the beefsteak using cyanoacrylate glue (as shown in Fig. A.2). Then, the phantom is stored at −20C in order to use it for image acquisition.

A.2 Imaging techniques

For MRI acquisitions, a Philips Achieva dStream (Inserm/UPS UMR 1214, ToNIC Technical platform, Toulouse, France) is used with a magnetization equal to 3T. Many sequences are acquired such as axial fat-suppressed T1-weighted sequences (multishot mode; 4 mm slice thickness; voxel matrix 4 × 1 × 4 mm) and T2-weighted sequences (multishot mode; 2 mm slice thickness; voxel matrix 0.8 × 2 × 2 mm).

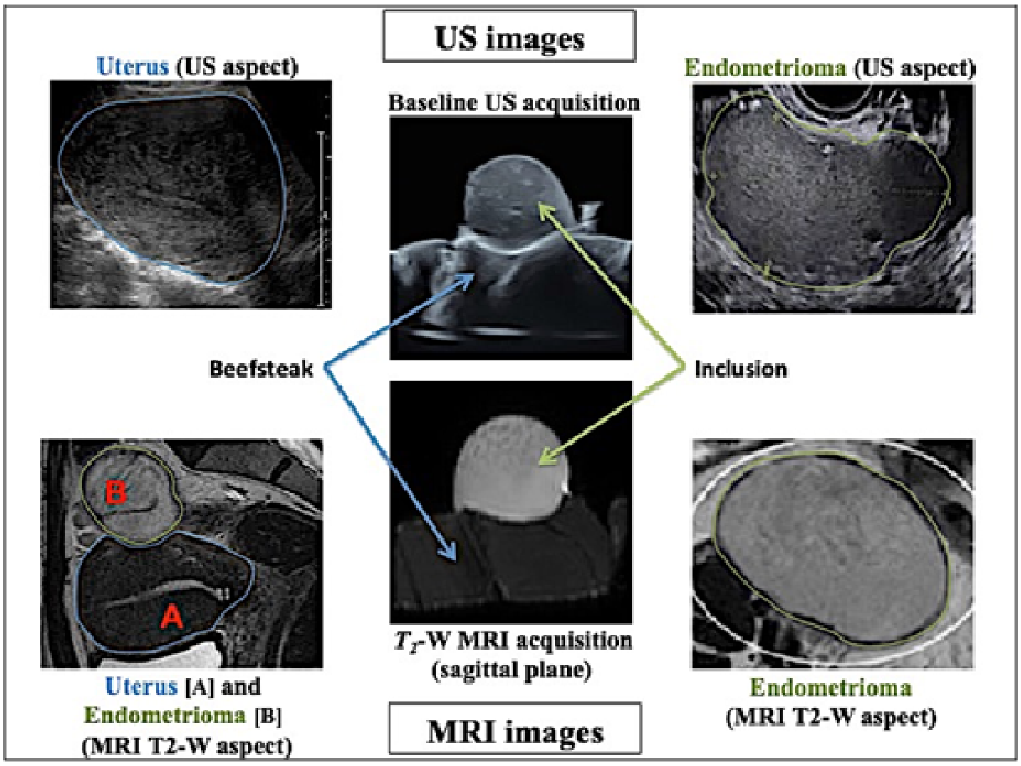

Figure A.3: US and MRI image acquired using the proposed customized phantom, showed by comparison with uterus and endometrioma images acquired in vivo

For Ultrasound acquisition, the phantom is immersed in water and then a 10-MHz linear array transducer (Voluson S10 system) is used to capture the image. The US acquisition of US image was done just after the acquisition of MRI to avoid a loss of information.

A.3 Imaging results

Myometrium is very well imitated by the beefsteak in the phantom as shown in the MRI image see Fig A.3 Also the PVA based mixture shows a homogenous low-level echogenicity content and well present the endometrioma The glue used that appears in the US image as a high-intensity line that separates the muscular part from the inclusion is very informative sing it represents a deep infiltration of endometrioma in the uterus.

Bibliography

[AA15] Nemir Ahmed Al-Azzawi. Medical image fusion based on shearlets and human feature visibility. *International Journal of Computer Applications*, 125(12):1–12, 2015.

[AAM$^+$04] Tal Arbel, Tal Arbel, Xavier Morandi, Roch M Comeau, and D Louis Collins. Automatic non-linear MRI-ultrasound registration for the correction of intra-operative brain deformations. *Computer Aided Surgery*, 9(4):123–136, 2004.

[AASAI09] Nemir Al-Azzawi, Harsa Amylia Mat Sakim, Ahmed K Wan Abdullah, and Haidi Ibrahim. Medical image fusion scheme using complex contourlet transform based on PCA. In *Proc. 2009 Annual International Conference of the IEEE Engineering in Medicine and Biology Society*, pages 5813–5816, Minneapolis, MN, 2009.

[AAVB16] Codruta O Ancuti, Cosmin Ancuti, Christophe De Vleeschouwer, and Alan C Bovik. Single-scale fusion: An effective approach to merging images. *IEEE Trans. Image Processing*, 26(1):65–78, 2016.

[AB07a] Tuncer C Aysal and Kenneth E Barner. Rayleigh-maximum-likelihood filtering for speckle reduction of ultrasound images. *IEEE Trans. Med. Imag.*, 26(5):712–727, 2007.

[AB07b] Tuncer C Aysal and Kenneth E Barner. Rayleigh-maximum-likelihood filtering for speckle reduction of ultrasound images. *IEEE Trans. Med. Imag.*, 26(5):712–727, 2007.

[ABT01] Alin Achim, Anastasios Bezerianos, and Panagiotis Tsakalides. Novel bayesian multiscale method for speckle removal in medical ultrasound images. *IEEE transactions on medical imaging*, 20(8):772–783, 2001.

[AEGG08] Brian B Avants, Charles L Epstein, Murray Grossman, and James C Gee. Symmetric diffeomorphic image registration with cross-correlation: evaluating automated labeling of elderly and neurodegenerative brain. *Medical image analysis*, 12(1):26–41, 2008.

[AGS$^+$20] Angélica Atehortúa, Mireille Garreau, Antoine Simon, Erwan Donal, Mathieu Lederlin, and Eduardo Romero. Fusion of 3D real-time echocardiography and cine MRI using a saliency analysis. *Computer Assisted Radiology and Surgery*, 15(2):277–285, 2020.

[AHPG09] Claire Allen, Sally Hopewell, Andrew Prentice, and Daisy Gregory. Nonsteroidal anti-inflammatory drugs for pain in women with endometriosis. *Cochrane Database of Systematic Reviews*, (2), 2009.

[AKHAFH09] Hanan Al Kadri, Samar Hassan, Haya M Al-Fozan, and Ali Hajeer. Hormone therapy for endometriosis and surgical menopause. *Cochrane Database of Systematic Reviews*, (1), 2009.

[AL19] Reza Abazari and Mehrdad Lakestani. Non-subsampled shearlet transform and log-transform methods for despeckling of medical ultrasound images. *Informatica*, 30(1):1–19, 2019.

[ANA18] M. Amin-Naji and A. Aghagolzadeh. Multi-focus image fusion in DCT domain using variance and energy of Laplacian and correlation coefficient for visual sensor networks. *Journal of AI and Data Mining*, 6:233–250, 2018.

[Anu20] Treatment of endometriosis. `http://www.safertility.co.uk/Treatment_of_endometriosis`, 2020.

[AO12] Anestis Antoniadis and Georges Oppenheim. *Wavelets and statistics*, volume 103. 2012.

[APABP03] MS Arruda, Carlos A Petta, Mauricio S Abrão, and Cristina L Benetti-Pinto. Time elapsed from onset of symptoms to diagnosis of endometriosis in a cohort study of Brazilian women. *Human reproduction*, 18(4):756–759, 2003.

[AR16] Fakhre Alam and Sami Ur Rahman. Intrinsic registration techniques for medical images: A state-of-the-art review. *Journal of Postgraduate Medical Institute (Peshawar-Pakistan)*, 30(2), 2016.

[ARU$^+$16] F Alam, SU Rahman, S Ullah, A Khalil, and A Uddin. A review on extrinsic registration methods for medical images. *Tech. J. Univ. Engineering Technol. Taxila*, 21:110–9, 2016.

[ATL14] Tarun Kumar Agarwal, Mayank Tiwari, and Subir Singh Lamba. Modified histogram based contrast enhancement using homomorphic filtering for medical images. In *Proc. 2014 IEEE International Advance Computing Conference (IACC)*, Chicago, Illinois, 2014.

[Ban08] Isaac Bankman. *Handbook of medical image processing and analysis*. Elsevier, 2008.

[BB11] Jerrold T Bushberg and John M Boone. *The essential physics of medical imaging*. Lippincott Williams & Wilkins, 2011.

[BBH$^+$17] Marc Bazot, Nishat Bharwani, Cyrille Huchon, K Kinkel, Teresa Margarida Cunha, Algesira Guerra, Lucia Manganaro, Laura Bunesch, Aki Kido, Kaori Togashi, et al. European society of urogenital radiology (ESUR) guidelines: MR imaging of pelvic endometriosis. *European radiology*, 27(7):2765–2775, 2017.

[BCBB10] Carlo Bulletti, Maria Elisabetta Coccia, Silvia Battistoni, and Andrea Borini. Endometriosis and infertility. *Journal of assisted reproduction and genetics*, 27(8):441–447, 2010.

[BEGR09] Avraham Ben-Ezra, Hayit Greenspan, and Yossi Rubner. Regularized super-resolution of brain MRI. In *Proc 2009 IEEE International Symposium on Biomedical Imaging: From Nano to Macro*, pages 254–257, Boston, MA, 2009.

[BGSW07] Serdar K Balci, Polina Golland, Martha Elizabeth Shenton, and William Mercer Wells. Free-form B-spline deformation model for groupwise registration. *Med. Imag. Comput. Assist. Interv.*, 10:23–30, 2007.

[BK89] Ruzena Bajcsy and Stane Kovačič. Multiresolution elastic matching. *Computer vision, graphics, and image processing*, 46(1):1–21, 1989.

[BKGD17] Durga Prasad Bavirisetti, Vijayakumar Kollu, Xiao Gang, and Ravindra Dhuli. Fusion of MRI and CT images using guided image filter and image statistics. *International journal of Imaging systems and Technology*, 27(3):227–237, 2017.

[BLCL08] Erik Blasch, Xiaokun Li, Genshe Chen, and Wenhua Li. Image quality assessment for performance evaluation of image fusion. In *Proc. 2008 11th International Conference on Information Fusion*, pages 1–6, Cologne, 2008.

[BLR$^+$09] Marc Bazot, Clarisse Lafont, Roman Rouzier, Gilles Roseau, Isabelle Thomassin-Naggara, and Emile Daraï. Diagnostic accuracy of physical examination, transvaginal sonography, rectal endoscopic sonography, and magnetic resonance imaging to diagnose deep infiltrating endometriosis. *Fertility and sterility*, 92(6):1825–1833, 2009.

[BM92] Paul J Besl and Neil D McKay. Method for registration of 3-D shapes. In *Sensor fusion IV: control paradigms and data structures*, volume 1611, pages 586–606, Boston, MA, United States, 1992.

[BMTY05] M Faisal Beg, Michael I Miller, Alain Trouvé, and Laurent Younes. Computing large deformation metric mappings via geodesic flows of diffeomorphisms. *International journal of computer vision*, 61(2):139–157, 2005.

[BN92] Richard K Beatson and Garry N Newsam. Fast evaluation of radial basis functions. *Computers & Mathematics with Applications*, 24(12):7–19, 1992.

[BNB03] Djamal Boukerroui, J Alison Noble, and Michael Brady. Velocity estimation in ultrasound images: A block matching approach. In *Information Processing in Medical Imaging*, pages 586–598, Heidelberg, Germany, 2003.

[BPC$^+$11] Stephen Boyd, Neal Parikh, Eric Chu, Borja Peleato, Jonathan Eckstein, et al. Distributed optimization and statistical learning via the alternating direction method of multipliers. *Foundations and Trends in Machine learning*, 3(1):1–122, 2011.

[BS16] Jayachandran Jai Jaganath Babu and Gnanou Florence Sudha. Adaptive speckle reduction in ultrasound images using fuzzy logic on coefficient of variation. *Biomedical Signal Processing and Control*, 23:93–103, 2016.

[BST14] Jérôme Bolte, Shoham Sabach, and Marc Teboulle. Proximal alternating linearized minimization or nonconvex and nonsmooth problems. *Mathematical Programming*, 146(1-2):459–494, 2014.

[BT09] Amir Beck and Marc Teboulle. A fast iterative shrinkage-thresholding algorithm for linear inverse problems. *SIAM journal on imaging sciences*, 2(1):183–202, 2009.

[Bur78] Christoph B Burckhardt. Speckle in ultrasound B-mode scans. *IEEE Transactions on Sonics and ultrasonics*, 25(1):1–6, 1978.

[C$^+$02] Boaz Cohen et al. New maximum likelihood motion estimation schemes for noisy ultrasound images. *Pattern Recognition*, 35(2):455–463, 2002.

[CCB06] N Cvejic, CN Canagarajah, and DR Bull. Image fusion metric based on mutual information and Tsallis entropy. *Electronics letters*, 42(11):626–627, 2006.

[CD14] Tianfeng Chai and Roland R Draxler. Root mean square error (RMSE) or mean absolute error (MAE)?–arguments against avoiding rmse in the literature. *Geoscientific model development*, 7(3):1247–1250, 2014.

[CE97] D. Louis Collins and Alan C. Evans. Animal: validation and applications of nonlinear registration-based segmentation. *International journal of pattern recognition and artificial intelligence*, 11(08):1271–1294, 1997.

[CEA00] SuChin Chen Coutre, MW Evens, and SG Armato. Performance evaluation of image registration. In *Proc. International Conference of the IEEE Engineering in Medicine and Biology Society (Cat. No. 00CH37143)*, volume 4, pages 3140–3143, Chicago, USA, 2000.

[CFK+18] Akshay S Chaudhari, Zhongnan Fang, Feliks Kogan, Jeff Wood, Kathryn J Stevens, Eric K Gibbons, Jin Hyung Lee, Garry E Gold, and Brian A Hargreaves. Super-resolution musculoskeletal MRI using deep learning. *Magnetic resonance in medicine*, 80(5):2139–2154, 2018.

[CGM+04] G Carbognin, A Guarise, L Minelli, I Vitale, R Malagó, G Zamboni, and C Procacci. Pelvic endometriosis: US and MRI features. *Abdominal imaging*, 29(5):609, 2004.

[Che16] Zhouye Chen. *Reconstruction of enhanced ultrasound images from compressed measurements*. PhD thesis, 2016.

[CHH04] William R Crum, Thomas Hartkens, and DLG Hill. Non-rigid image registration: theory and practice. *The British journal of radiology*, 77(2):S140–S153, 2004.

[Chr03] James D Christensen. Normalization of brain magnetic resonance images using histogram even-order derivative analysis. *Magnetic resonance imaging*, 21(7):817–820, 2003.

[Cia10] Mario Ciampi. Medical image fusion for color visualization via 3D RDWT. In *Proc. 10th IEEE International Conference on Information Technology and Applications in Biomedicine*, pages 1–6, Corfu, Greece, 2010.

[CLBC] Nedeljko Cvejic, Artur Loza, David Bull, and Nishan Canagarajah. A similarity metric for assessment of image fusion algorithms. *International journal of signal processing*, 2(3):178–182.

[CMD$^+$95] André Collignon, Frederik Maes, Dominique Delaere, Dirk Vandermeulen, Paul Suetens, and Guy Marchal. Automated multi-modality image registration based on information theory. In *Information processing in medical imaging*, volume 3, pages 263–274, Leuven, Belgium, 1995.

[CP00] Xydeas CS, , and Vladimir Petrovic. Objective image fusion performance measure. *Electronics letters*, 36(4):308–309, 2000.

[CR03] Haili Chui and Anand Rangarajan. A new point matching algorithm for non-rigid registration. *Computer Vision and Image Understanding*, 89(2-3):114–141, 2003.

[CXZ$^+$18] Yuhua Chen, Yibin Xie, Zhengwei Zhou, Feng Shi, Anthony G Christodoulou, and Debiao Li. Brain MRI super resolution using 3D deep densely connected neural networks. In *Proc. IEEE Int. Symp. Biomed. Imaging (ISBI)*, pages 739–742, Washington, DC, 2018.

[CZW09] Zhiming Cui, Guangming Zhang, and Jian Wu. Medical image fusion based on wavelet transform and independent component analysis. In *Proc. 2009 International Joint Conference on Artificial Intelligence*, pages 480–483, Hainan Island, 2009.

[DA00] James S Duncan and Nicholas Ayache. Medical image analysis: Progress over two decades and the challenges ahead. *IEEE Trans. Pattern Anal. and machine intelligence*, 22(1):85–106, 2000.

[DAC$^+$14] James MN Duffy, Kirana Arambage, Frederico JS Correa, David Olive, Cindy Farquhar, Ray Garry, David H Barlow, and Tal Z Jacobson. Laparoscopic surgery for endometriosis. *Cochrane Database of Systematic Reviews*, (4), 2014.

[DCdBdM$^+$04] Mathieu De Craene, Aloys du Bois d'Aische, Benoît Macq, Florian Kipfmueller, Neil Weisenfeld, Steven Haker, and Simon K Warfield. Multimodal nonrigid registration using a stochastic gradient approximation. In *Proc. International Symposium on Biomedical Imaging: Nano to Macro*, pages 1459–1462, Arlington, VA, USA, 2004.

[DEDV19] Leandro Morera Delfin, Raul Pinto Elias, Humberto de Jesús Ochoa Domínguez, and Osslan Osiris Overgara Villegas. Auto-regularized gradients of adaptive interpolation for MRI super-resolution. *Journal of Signal Processing Systems*, 91(8):885–898, 2019.

[Des09] T Deserno. Medical image processing. *Optipedia, SPIE Press, Bellingham, WA*, 2009.

[Dia13] Bakary Diarra. *Study and optimization of 2D matrix arrays for 3D ultrasound imaging*. PhD thesis, Université Claude Bernard - Lyon I, 2013.

[DJ08] Jihad S Daba and Philip Jreije. Advanced stochastic models for partially developed speckle. *World Academy of Science, Engineering and Technology*, 41:566–570, 2008.

[DK12] Sudeb Das and Malay Kumar Kundu. NSCT-based multimodal medical image fusion using pulse-coupled neural network and modified spatial frequency. *Medical & biological engineering & computing*, 50(10):1105–1114, 2012.

[DLLX16] Jiao Du, Weisheng Li, Ke Lu, and Bin Xiao. An overview of multi-modal medical image fusion. *Neurocomputing*, 215:3–20, 2016.

[DLXN16] Jiao Du, Weisheng Li, Bin Xiao, and Qamar Nawaz. Union Laplacian pyramid with multiple features for medical image fusion. *Neurocomputing*, 194:326–339, 2016.

[DM07] Elaine Denny and Christopher H Mann. Endometriosis-associated dyspareunia: the impact on women's lives. *BMJ Sexual & Reproductive Health*, 33(3):189–193, 2007.

[DMVS03] Emiliano D'agostino, Frederik Maes, Dirk Vandermeulen, and Paul Suetens. A viscous fluid model for multimodal non-rigid image registration using mutual information. *Medical image analysis*, 7(4):565–575, 2003.

[DNPCR90] Jacques Donnez, M Nisolle-Pochet, and F Casanas-Roux. Endometriosis-associated infertility: evaluation of preoperative use of danazol, gestrinone, and buserelin. *International Journal of Fertility*, 35(5):297–301, 1990.

[Doi07] Kunio Doi. Computer-aided diagnosis in medical imaging: historical review, current status and future potential. *Computerized medical imaging and graphics*, 31(4-5):198–211, 2007.

[DR17] Olivier Donnez and Horace Roman. Choosing the right surgical technique for deep endometriosis: shaving, disc excision, or bowel resection? *Fertility and sterility*, 108(6):931–942, 2017.

[DV05] Minh N Do and Martin Vetterli. The contourlet transform: an efficient directional multiresolution image representation. *IEEE Trans. imag. process.*, 14(12):2091–2106, 2005.

[DVB$^+$93] Sherri L Darrow, John E Vena, Ronald E Batt, Maria A Zielezny, Arthur M Michalek, and Sharon Selman. Menstrual cycle characteristics and the risk of endometriosis. *Epidemiology*, pages 135–142, 1993.

[DY11] Richard Dosselmann and Xue Dong Yang. A comprehensive assessment of the structural similarity index. *Signal, Image and Video Processing*, 5(1):81–91, 2011.

[EMVB$^+$20] Oumaima El Mansouri, Fabien Vidal, Adrian Basarab, Pierre Payoux, Denis Kouamé, and Jean-Yves Tourneret. Fusion of magnetic resonance and ultrasound images for endometriosis detection. *IEEE Trans. Image Process.*, 29:5324–5335, 2020.

[Fal56] Roy E Fallas. Endometriosis demonstration for the Sampson theory by a human anomaly. *American Journal of Obstetrics & Gynecology*, 72(3):557–561, 1956.

[FAS$^+$12] Parastoo Farnia, Alireza Ahmadian, Mahdi Sedighpoor, Alireza Khoshnevisan, and Meysam Siyah Mansoory. On the performance of improved ICP algorithms for registration of intra-ultrasound with pre-MR images; a phantom study. In *Proc. 2012*

Annual International Conference of the IEEE Engineering in Medicine and Biology Society, pages 4390–4393, San Diego, CA, 2012.

[FBF+11] Jessica Fourquet, Lorna Báez, Michelle Figueroa, Iván Iriarte, and Idhaliz Flores. Quantification of the impact of endometriosis symptoms on health-related quality of life and work productivity. *Fertility and sterility*, 96(1):107–112, 2011.

[FDG85] Hiroshi Fujita, Kunio Doi, and Maryellen Lissak Giger. Investigation of basic imaging properties in digital radiography. 6. MTFs of digital imaging systems. *Medical physics*, 12(6):713–720, 1985.

[FFP+18] Pietro Valerio Foti, Renato Farina, Stefano Palmucci, Ilenia Anna Agata Vizzini, Norma Libertini, Maria Coronella, Saveria Spadola, Rosario Caltabiano, Marco Iraci, Antonio Basile, et al. Endometriosis: clinical features, MR imaging findings and pathologic correlation. *Insights into imaging*, 9(2):149–172, 2018.

[FLM+13] Leyuan Fang, Shutao Li, Ryan P McNabb, Qing Nie, Anthony N Kuo, Cynthia A Toth, Joseph A Izatt, and Sina Farsiu. Fast acquisition and reconstruction of optical coherence tomography images via sparse representation. *IEEE Trans. Med. Imag.*, 32(11):2034–2049, 2013.

[FM04] Bernd Fischer and Jan Modersitzki. A unified approach to fast image registration and a new curvature based registration technique. *Linear Algebra and its applications*, 380:107–124, 2004.

[FTT14] Konstantina Fotiadou, Grigorios Tsagkatakis, and Panagiotis Tsakalides. Low light image enhancement via sparse representations. In *Proc. Int. Conference on Image Analysis and Recognition*, pages 84–93, Vilamoura, Algarve, Portugal, 2014.

[FWMN14] Bernhard Fuerst, Wolfgang Wein, Markus Müller, and Nassir Navab. Automatic ultrasound-MRI registration for neurosurgery using the 2D and 3D LC2 metric. *Medical image analysis*, 18(8):1312–1319, 2014.

[GCS05a] Savita Gupta, Ramesh Chand Chauhan, and Sweta Chaman Saxena. Locally adaptive wavelet domain Bayesian processor for denoising medical ultrasound images using speckle modelling based on Rayleigh distribution. *IEE Proc. Vis. Image Signal Process.*, 152(1):129–135, 2005.

[GCS05b] Savita Gupta, Ramesh Chand Chauhan, and Sweta Chaman Saxena. Locally adaptive wavelet domain bayesian processor for denoising medical ultrasound images using speckle modelling based on Rayleigh distribution. *IEE Proc. Vis. Image Signal Process.*, 152(1):129–135, 2005.

[GD84] Maryellen Lissak Giger and Kunio Doi. Investigation of basic imaging properties in digital radiography. i. modulation transfer function. *Medical Physics*, 11(3):287–295, 1984.

[GD85] Maryellen Lissak Giger and Kunio Doi. Investigation of basic imaging properties in digital radiography. 3. effect of pixel size on SNR and threshold contrast. *Medical physics*, 12(2):201–208, 1985.

[GDF86] Maryellen Lissak Giger, Kunio Doi, and Hiroshi Fujita. Investigation of basic imaging properties in digital radiography. 7. noise wiener spectra of ii–tv digital imaging systems. *Medical physics*, 13(2):131–138, 1986.

[GEW10] Ali Gholipour, Judy A Estroff, and Simon K Warfield. Robust super-resolution volume reconstruction from slice acquisitions: application to fetal brain MRI. *IEEE Trans. Med. Imag.*, 29(10):1739–1758, 2010.

[Giu10] Linda C Giudice. Endometriosis. *New England Journal of Medicine*, 362(25):2389–2398, 2010.

[GKMT06] Shruti Garg, K Ushah Kiran, Ram Mohan, and US Tiwary. Multilevel medical image fusion using segmented image by level set evolution with region competition.

In *Proc. IEEE Engineering in Medicine and Biology 27th Annual Conference*, pages 7680–7683, Shanghai, China, 2006.

[GKT$^+$08] Ben Glocker, Nikos Komodakis, Georgios Tziritas, Nassir Navab, and Nikos Paragios. Dense image registration through MRFs and efficient linear programming. *Medical image analysis*, 12(6):731–741, 2008.

[GLP01] David G Gobbi, Belinda KH Lee, and Terence M Peters. Correlation of preoperative mri and intraoperative 3d ultrasound to measure brain tissue shift. In *Proc. Medical Imaging: Visualization, Display, and Image-Guided Procedures*, volume 4319, pages 264–271, 2001.

[GOM$^+$10] Soumya Ghose, Arnau Oliver, Robert Martí, Xavier Lladó, Jordi Freixenet, Joan Vilanova, and Fabrice Meriaudeau. Texture guided active appearance model propagation for prostate segmentation. In *Proc. Int. Workshop on Prostate Cancer Imaging*, pages 111–120, Berlin, Heidelberg, 2010.

[GP95] Hákon Gudbjartsson and Samuel Patz. The Rician distribution of noisy MRI data. *Magnetic resonance in medicine*, 34(6):910–914, 1995.

[GP02] Sébastien Granger and Xavier Pennec. Multi-scale EM-ICP: A fast and robust approach for surface registration. In *Proc. European Conference on Computer Vision*, pages 418–432, Berlin, Heidelberg, 2002.

[GP13] Ashwini Galande and Ratna Patil. The art of medical image fusion: A survey. In *Proc. Int. Conference on Advances in Computing, Communications and Informatics (ICACCI)*, pages 400–405, Mysore, 2013.

[GPOK02] Hayit Greenspan, Sharon Peled, Gal Oz, and Nahum Kiryati. MRI inter-slice reconstruction using super-resolution. *Magnetic resonance imaging*, 20(5):437–446, 2002.

[GPS89] Dorothy M Greig, Bruce T Porteous, and Allan H Seheult. Exact maximum a posteriori estimation for binary images. *Journal of the Royal Statistical Society: Series B (Methodological)*, 51(2):271–279, 1989.

[GSA16] Nidhi Gupta, AP Shukla, and Suneeta Agarwal. Despeckling of medical ultrasound images: a technical review. *International Journal of Information Engineering and Electronic Business*, 8(3):11, 2016.

[GSP05] Nikhil Gupta, M N S Swamy, and Eugene Plotkin. Despeckling of medical ultrasound images using data and rate adaptive lossy compression. *IEEE Trans. Med. Imag.*, 24(6):743–754, 2005.

[GTN03] Smadar Gefen, Oleh Tretiak, and Jonathan Nissanov. Elastic 3-D alignment of rat brain histological images. *IEEE Trans. Med. Imag.*, 22(11):1480–1489, 2003.

[Guo09] Sun-Wei Guo. Recurrence of endometriosis and its control. *Human reproduction update*, 15(4):441–461, 2009.

[GVM04] Joan Glaunès, Marc Vaillant, and Michael I Miller. Landmark matching via large deformation diffeomorphisms on the sphere. *Journal of mathematical imaging and vision*, 20(1-2):179–200, 2004.

[Gyn15] WA GynaeScope. Laparoscopic surgery for endometriosis. `https://www.wagynaescope.com.au/laparoscopic-surgery-for-endometriosis`, 2015.

[HAA17] Jude D Hemanth, J Anitha, and Bernadetta Kwintiana Ane. Fusion of artificial neural networks for learning capability enhancement: Application to medical image classification. *Expert Systems*, 34(6):e12225, 2017.

[HAY10] Md Foisal Hossain, Mohammad Reza Alsharif, and Katsumi Yamashita. Medical image enhancement based on nonlinear technique and logarithmic transform coefficient histogram matching. In *Proc. International Conference on Complex Medical Engineering*, pages 58–62, Gold Coast, Queensland, Australia, 2010.

[HCM⁺88] Milan R Henzl, Stephen L Corson, Kamran Moghissi, Veasy C Buttram, Christer Berqvist, and Jan Jacobson. Administration of nasal nafarelin as compared with oral danazol for endometriosis. *New England Journal of Medicine*, 318(8):485–489, 1988.

[HDC⁺86] Kenneth R Hoffmann, Kunio Doi, Heang-Ping Chan, Laura Fencil, Hiroshi Fujita, and Alan Muraki. Automated tracking of the vascular tree in DSA images using a double-square-box region-of-search algorithm. In *Application of Optical Instrumentation in Medicine XIV and Picture Archiving and Communication Systems*, volume 626, pages 326–333, Newport Beach, CA, United States, 1986.

[HET⁺11] Gernot Hudelist, James English, Alan Thomas, Andrea Tinelli, Christian Singer, and Joerg Keckstein. Diagnostic accuracy of transvaginal ultrasound for non-invasive diagnosis of bowel endometriosis: systematic review and meta-analysis. *Ultrasound in obstetrics & gynecology*, 37(3):257–263, 2011.

[HHR⁺05] Xishi Huang, Nicholas Hill, Jing Ren, Gerard Guiraudon, Derek Boughner, and Terry M Peters. Dynamic 3D ultrasound and MR image registration of the beating heart. In *Proc. International Conference on Medical Image Computing and Computer-Assisted Intervention*, pages 171–178, Berlin, Heidelberg, 2005.

[HJB⁺12] Mattias Heinrich, Mark Jenkinson, Manav Bhushan, Tahreema Matin, Fergus Gleeson, Michael Brady, and Julia A Schnabel. MIND: Modality independent neighbourhood descriptor for multi-modal deformable registration. *Medical image analysis*, 16(7):1423–1435, 2012.

[HJP⁺13] Mattias Paul Heinrich, Mark Jenkinson, Bartlomiej W Papież, Michael Brady, and Julia A Schnabel. Towards realtime multimodal fusion for image-guided interventions using self-similarities. In *Proc. International conference on medical image computing and computer-assisted intervention*, pages 187–194, Berlin, Heidelberg, 2013.

[HLLW10] Changtao He, Quanxi Liu, Hongliang Li, and Haixu Wang. Multimodal medical image fusion based on IHS and PCA. *Procedia Engineering*, 7:280–285, 2010.

[HLZ+17] Zhenghua Huang, Qian Li, Tianxu Zhang, Nong Sang, and Hanyu Hong. Iterative weighted sparse representation for x-ray cardiovascular angiogram image denoising over learned dictionary. *IET Image Processing*, 12(2):254–261, 2017.

[HM07] Eldad Haber and Jan Modersitzki. Image registration with guaranteed displacement regularity. *International journal of computer vision*, 71(3):361–372, 2007.

[HPM06] Xiaolei Huang, Nikos Paragios, and Dimitris N Metaxas. Shape registration in implicit spaces using information theory and free form deformations. *IEEE transactions on pattern analysis and machine intelligence*, 28(8):1303–1318, 2006.

[HS81] Berthold KP Horn and Brian G Schunck. Determining optical flow. In *Techniques and Applications of Image Understanding*, volume 281, pages 319–331. International Society for Optics and Photonics, 1981.

[HZ85] John D Head and Michael C Zerner. A Broyden—Fletcher—Goldfarb—Shanno optimization procedure for molecular geometries. *Chemical physics letters*, 122(3):264–270, 1985.

[HZ10] Alain Hore and Djemel Ziou. Image quality metrics: PSNR vs. SSIM. In *Proc. ICPR*, pages 2366–2369, Istanbul, Turkey, 2010.

[IDLL84] Masamitsu Ishida, Koichiro Doi, Lina Loo, and James Lehr. Digital image processing: effect on detectability of simulated low-contrast radiographic patterns. *Radiology*, 150(2):569–575, 1984.

[IFDL83] Masamitsu Ishida, Paul Frank, Kunio Doi, and James Lehr. High quality digital radiographic images: improved detection of low-contrast objects and preliminary clinical studies. *Radiographics*, 3(2):325–338, 1983.

[IKDF82] Masamitsu Ishida, Hisatoyo Kato, Kunio Doi, and Paul Frank. Development of a new digital radiographic image processing system. In *Proc. Application of Optical Instrumentation in Medicine X*, volume 347, pages 42–48, New Orleans, United States, 1982.

[IP11] N Indhumadhi and G Padmavathi. Enhanced image fusion algorithm using Laplacian pyramid and spatial frequency based wavelet algorithm. *Int. J. Comput. Sci. Eng*, 1(5):298–303, 2011.

[JB18] P Jidesh and Balaji Banothu. Image despeckling with non-local total bounded variation regularization. *Computers & Electrical Engineering*, 70:631–646, 2018.

[JD14a] Alex Pappachen James and Belur Dasarathy. Medical image fusion: A survey of the state of the art. *Information fusion*, 19:4–19, 2014.

[JD14b] Alex Pappachen James and Belur Dasarathy. Medical image fusion: A survey of the state of the art. *Information Fusion*, 19:4–19, 2014.

[JDB+10] Tal Jacobson, James Duffy, David Barlow, Cindy Farquhar, Philippe Koninckx, and David Olive. Laparoscopic surgery for subfertility associated with endometriosis. *Cochrane Database of Systematic Reviews*, (1), 2010.

[JLY] Wei Jin, Jin-xiang Li, and Rener Yang. Medical image fusion using HMT model in aliasing-free contourlet domain [j]. *Journal of image and graphics*, 2.

[JRH+13] EB Janssen, ACM Rijkers, Karel Hoppenbrouwers, Christel Meuleman, and TM d'Hooghe. Prevalence of endometriosis diagnosed by laparoscopy in adolescents with dysmenorrhea or chronic pelvic pain: a systematic review. *Human reproduction update*, 19(5):570–582, 2013.

[JS18] Taylor Joel and Raghupathy Sivakumar. An extensive review on despeckling of medical ultrasound images using various transformation techniques. *Applied Acoustics*, 138:18–27, 2018.

[JSTL07] Anand A Joshi, David W Shattuck, Paul M Thompson, and Richard M Leahy. Surface-constrained volumetric brain registration using harmonic mappings. *IEEE Trans. Med. Imag.*, 26(12):1657–1669, 2007.

[KD15] Jeff Kinley and Raymond Damadian. *Gifted Mind: The Dr. Raymond Damadian Story, Inventor of the MRI.* New Leaf Publishing Group, 2015.

[KDM+02] George C Kagadis, Konstantinos K Delibasis, George K Matsopoulos, Nikolaos A Mouravliansky, Pantelis A Asvestas, and George C Nikiforidis. A comparative study of surface-and volume-based techniques for the automatic registration between CT and SPECT brain images. *Medical Physics*, 29(2):201–213, 2002.

[KEBH13] Julia Krüger, Jan Ehrhardt, Arpad Bischof, and Heinz Handels. Breast compression simulation using ICP-based B-spline deformation for correspondence analysis in mammography and MRI datasets. In *Medical Imaging 2013: Image Processing*, volume 8669, page 86691D, Florida, United States, 2013.

[KFBC06] Karen Kinkel, Kathrin A Frei, Corinne Balleyguier, and Charles Chapron. Diagnosis of endometriosis with imaging: a review. *European radiology*, 16(2):285–298, 2006.

[KHC08] Srivatsan Kandadai, Joseph Hardin, and Charles Creusere. Audio quality assessment using the mean structural similarity measure. In *Proc. IEEE International Conference on Acoustics, Speech and Signal Processing*, pages 221–224, Las Vegas, NV, 2008.

[KHN96] Chi-Wah Kok, Yui Hui, and Thuc-Quyen Nguyen. Medical image pseudo coloring by wavelet fusion. In *Proc. International Conference of the IEEE Engineering in Medicine and Biology Society*, volume 2, pages 648–649, Amsterdam, Netherlands, 1996.

[KK16] Randeep Kaur and Sandeep Kaur. Comparison of contrast enhancement techniques for medical image. In *Proc. conference on emerging devices and smart systems (ICEDSS)*, pages 155–159, Namakkal, 2016.

[KKJ⁺10] Ashish Khare, Manish Khare, Yongyeon Jeong, Hongkook Kim, and Moongu Jeon. Despeckling of medical ultrasound images using Daubechies complex wavelet transform. *Signal Processing*, 90(2):428–439, 2010.

[KKM⁺09] Sven Kabus, Tobias Klinder, Keelin Murphy, Bram van Ginneken, Cristian Lorenz, and Josien PW Pluim. Evaluation of 4D-CT lung registration. In *Proc. International Conference on Medical Image Computing and Computer-Assisted Intervention*, pages 747–754, Berlin, Heidelberg, 2009.

[KOM⁺08] Cleophas Kyama, Lutgart Overbergh, Attila Mihalyi, Christel Meuleman, Jason Mwenda, Chantal Mathieu, and Thomas D'Hooghe. Endometrial and peritoneal expression of aromatase, cytokines, and adhesion factors in women with endometriosis. *Fertility and sterility*, 89(2):301–310, 2008.

[KR05] Debasis Kundu and Mohammad Raqab. Generalized Rayleigh distribution: different methods of estimations. *Computational statistics & data analysis*, 49(1):187–200, 2005.

[KS19] Manjit Kaur and Dilbag Singh. Fusion of medical images using deep belief networks. *Cluster Computing*, pages 1–15, 2019.

[KS20] Priyanka Kokil and S Sudharson. Despeckling of clinical ultrasound images using deep residual learning. *Computer Methods and Programs in Biomedicine*, page 105477, 2020.

[KSK96] Björn Krebs, Peter Sieverding, and Bernd Korn. A fuzzy ICP algorithm for 3D free-form object recognition. In *Proceedings of 13th International Conference on Pattern Recognition*, volume 1, pages 539–543, Vienna, Austria, 1996.

[KSP07] Stefan Klein, Marius Staring, and Josien PW Pluim. Evaluation of optimization methods for nonrigid medical image registration using mutual information and B-splines. *IEEE Trans. Image Process.*, 16(12):2879–2890, 2007.

[KY12] Jari Korhonen and Junyong You. Peak signal-to-noise ratio revisited: Is simple beautiful? In *Proc. International Workshop on Quality of Multimedia Experience*, pages 37–38, Yarra Valley, VIC, 2012.

[KZW+12] Samuel Kadoury, Lyubomir Zagorchev, Bradford J Wood, Aradhana Venkatesan, Jürgen Weese, J Jago, and Jochen Kruecker. A model-based registration approach of preoperative MRI with 3D ultrasound of the liver for interventional guidance procedures. In *Proc. IEEE Int. Symp. Biomed. Imaging (ISBI)*, pages 952–955, Barcelona, Spain, 2012.

[LBCA10] Artur Loza, David Bull, Nishan Canagarajah, and Alin Achim. Non-Gaussian model-based fusion of noisy images in the wavelet domain. *Computer Vision and Image Understanding*, 114(1):54–65, 2010.

[LC20] Mathew Leonardi and George Condous. Noninvasive ultrasound diagnosis of endometriosis. https://www.contemporaryobgyn.net/view/noninvasive-ultrasound-diagnosis-endometriosis, 2020.

[LDM85] Leh-Nien Loo, Kunio Doi, and Charles Metz. Investigation of basic imaging properties in digital radiography. 4. effect of unsharp masking on the detectability of simple patterns. *Medical physics*, 12(2):209–214, 1985.

[LDZL18] Weisheng Li, Jiao Du, Zhengmin Zhao, and Jinyi Long. Fusion of medical sensors using adaptive cloud model in local Laplacian pyramid domain. *IEEE Trans. Biomed. Engineering*, 66(4):1172–1183, 2018.

[LF98] Shang-Hong Lai and Ming Fang. Adaptive medical image visualization based on hierarchical neural networks and intelligent decision fusion. In *Neural Networks for Signal*

Processing VIII. Proceedings of the 1998 IEEE Signal Processing Society Workshop (Cat. No. 98TH8378), pages 438–447, Cambridge, 1998.

[LHS$^+$63] Gwilym Lodwick, Cosmo Haun, Walton Smith, Roy Keller, and Eddie Robertson. Computer diagnosis of primary bone tumors: A preliminary report. *Radiology*, 80(2):273–275, 1963.

[LLS$^+$13] Qiegen Liu, Dong Liang, Ying Song, Jianhua Luo, Yuemin Zhu, and Wenshu Li. Augmented lagrangian-based sparse representation method with dictionary updating for image deblurring. *SIAM Journal on Imaging Sciences*, 6(3):1689–1718, 2013.

[LLW15] Yu Liu, Shuping Liu, and Zengfu Wang. A general framework for image fusion based on multi-scale transform and sparse representation. *Information fusion*, 24:147–164, 2015.

[LMM95] Hui Li, Bangalore Manjunath, and Sanjit Mitra. Multisensor image fusion using the wavelet transform. *Graphical models and image processing*, 57(3):235–245, 1995.

[LMW$^+$07] Marc Levivier, Nicolas Massager, David Wikler, Daniel Devriendt, and Serge Goldman. Integration of functional imaging in radiosurgery: the example of PET scan. In *Radiosurgery and pathological fundamentals*, volume 20, pages 68–81. 2007.

[LSH$^+$18] Yuanyuan Li, Yanjing Sun, Xinhua Huang, Guanqiu Qi, Mingyao Zheng, and Zhiqin Zhu. An image fusion method based on sparse representation and sum modified-Laplacian in NSCT domain. *Entropy*, 20(7):522, 2018.

[LYF12] Shutao Li, Haitao Yin, and Leyuan Fang. Group-sparse representation with dictionary learning for medical image denoising and fusion. *IEEE Transactions on biomedical engineering*, 59(12):3450–3459, 2012.

[LZG07] Xiaoqi Lu, Baohua Zhang, and Yong Gu. Medical image fusion algorithm based on clustering neural network. In *Proc. International Conference on Bioinformatics and Biomedical Engineering*, pages 637–640, Wuhan, China, 2007.

[LZW$^+$11] Dror Lederman, Bin Zheng, Xingwei Wang, Xiao Hui Wang, and David Gur. Improving breast cancer risk stratification using resonance-frequency electrical impedance spectroscopy through fusion of multiple classifiers. *Annals of biomedical engineering*, 39(3):931–945, 2011.

[MA10] Raman Maini and Himanshu Aggarwal. A comprehensive review of image enhancement techniques. *arXiv:1003.4053*, 2010.

[MBBK15] Renaud Morin, Adrian Basarab, Stéphanie Bidon, and Denis Kouamé. Motion estimation-based image enhancement in ultrasound imaging. *Ultrasonics*, 60:19–26, 2015.

[MBV$^+$19] Oumaima El Mansouri, Adrian Basarab, Fabien Vidal, Denis Kouamé, and Jean-Yves Tourneret. Fusion of magnetic resonance and ultrasound images: A preliminary study on simulated data. In *Proc. IEEE Int. Symp. Biomed. Imaging (ISBI)*, pages 1733–1736, Venice, Italy, 2019.

[MCB$^+$10a] José Manjón, Pierrick Coupé, Antonio Buades, Louis Collins, and Montserrat Robles. MRI superresolution using self-similarity and image priors. *International journal of biomedical imaging*, 2010:11, 2010.

[MCB$^+$10b] José Manjón, Pierrick Coupé, Antonio Buades, Louis Collins, and Montserrat Robles. MRI superresolution using self-similarity and image priors. *Int. J. Biomed. Imaging*, 2010:11, 2010.

[MCS$^+$07] Antonio Moreno, Sylvie Chambon, Anand P Santhanam, Roberta Brocardo, Patrick Kupelian, Jannick P Rolland, Elsa Angelini, and Isabelle Bloch. Thoracic CT-PET registration using a 3D breathing model. In *Proc. International Conference on Medical Image Computing and Computer-Assisted Intervention*, pages 626–633, Berlin, Heidelberg, 2007.

[MCV$^+$97] Frederik Maes, Andre Collignon, Dirk Vandermeulen, Guy Marchal, and Paul

Suetens. Multimodality image registration by maximization of mutual information. *IEEE Trans. Med. Imag.*, 16(2):187–198, 1997.

[MJ20] Sarmad Maqsood and Umer Javed. Multi-modal medical image fusion based on two-scale image decomposition and sparse representation. *Biomedical Signal Processing and Control*, 57:101810, 2020.

[MJF$^+$12] Mehdi Moradi, Firdaus Janoos, Andriy Fedorov, Petter Risholm, Tina Kapur, Luciant Wolfsberger, Paul Nguyen, Clare Tempany, and William Wells. Two solutions for registration of ultrasound to MRI for image-guided prostate interventions. In *Proc. International Conference of the IEEE Engineering in Medicine and Biology Society*, pages 1129–1132, San Diego, CA, 2012.

[MK14] Amir Pasha Mahmoudzadeh and Nasser H Kashou. Interpolation-based super-resolution reconstruction: effects of slice thickness. *Journal of Medical Imaging*, 1(3):034007, 2014.

[MLM$^+$01] Matthew McAuliffe, Francois Lalonde, Delia McGarry, William Gandler, Karl Csaky, and Benes Trus. Medical image processing, analysis and visualization in clinical research. In *Proc. IEEE Symposium on Computer-Based Medical Systems. CBMS 2001*, pages 381–386, Bethesda, MD, USA, 2001.

[MM93] Mette Moen and Per Magnus. The familial risk of endometriosis. *Acta obstetricia et gynecologica Scandinavica*, 72(7):560–564, 1993.

[MM08] Tarek Mahmoud and Stephen Marshall. Medical image enhancement using threshold decomposition driven adaptive morphological filter. In *Proc. European Signal Processing Conference*, pages 1–5, Lausanne, 2008.

[MM09] Francesco Masulli and Sushmita Mitra. Natural computing methods in bioinformatics: A survey. *Information Fusion*, 10(3):211–216, 2009.

[MMO$^+$12] Jhimli Mitra, Robert Martí, Arnau Oliver, Xavier Lladó, Soumya Ghose, Joan Vilanova, and Fabrice Meriaudeau. Prostate multimodality image registration based on B-splines and quadrature local energy. *International journal of computer assisted radiology and surgery*, 7(3):445–454, 2012.

[MNJB$^+$64] Phillip Meyers, Charles Nice Jr, Hal Becker, Wilson Nettleton, James Sweeney, and George Meckstroth. Automated computer analysis of radiographic images. *Radiology*, 83(6):1029–1034, 1964.

[MOM$^+$10] Jhimli Mitra, Arnau Oliver, Robert Marti, Xavier Lladó, Joan Vilanova, and Fabrice Meriaudeau. Multimodal prostate registration using thin-plate splines from automatic correspondences. In *Proc. International Conference on Digital Image Computing: Techniques and Applications*, pages 587–592, Sydney, Australia, 2010.

[Mor13] Renaud Morin. *Amélioration de la résolution en imagerie ultrasonore*. PhD thesis, Université de Toulouse, Université Toulouse III-Paul Sabatier, 2013.

[MS00] John Mathews and Giovanni Sicuranza. *Polynomial signal processing*. John Wiley & Sons, Inc., 2000.

[MS18] Shaine Morris and Timothy Slesnick. Magnetic resonance imaging. *Visual Guide to Neonatal Cardiology*, pages 104–108, 2018.

[MT06] Oleg Michailovich and Allen Tannenbaum. Despeckling of medical ultrasound images. *IEEE transactions on ultrasonics, ferroelectrics, and frequency control*, 53(1):64–78, 2006.

[MVR$^+$10] Marc Modat, Tom Vercauteren, Gerard R Ridgway, David J Hawkes, Nick C Fox, and Sébastien Ourselin. Diffeomorphic demons using normalized mutual information, evaluation on multimodal brain MR images. In *Medical Imaging 2010: Image Processing*, volume 7623, page 76232K, California, United States, 2010.

[MZY15] Jiayi Ma, Ji Zhao, and Alan L Yuille. Non-rigid point set registration by preserving global and local structures. *IEEE Trans. imag. Process.*, 25(1):53–64, 2015.

[NBF$^+$16] Vicki Nisenblat, Patrick Bossuyt, Cindy Farquhar, Neil Johnson, and Louise Hull. Imaging modalities for the non-invasive diagnosis of endometriosis. *Cochrane Database of Systematic Reviews*, 7(2):CD009591, 2016.

[NBK14] Muhammad Nasir, Asim Baig, and Aasia Khanum. Brain tumor classification in MRI scans using sparse representation. In *Proc. International Conference on Image and Signal Processing*, pages 629–637, Normandy, France, 2014.

[NCG86] Camran Nezhat, Scott Crowgey, and Charles Garrison. Surgical treatment of endometriosis via laser laparoscopy. *Fertility and Sterility*, 45(6):778–783, 1986.

[NHG$^+$95] Anne Namnoum, Timothy Hickman, Sandra Goodman, Dan Gehlbach, and John Rock. Incidence of symptom recurrence after hysterectomy for endometriosis. *Fertility and sterility*, 64(5):898–902, 1995.

[NKS$^+$09] Ramkrishnan Narayanan, John Kurhanewicz, Katsuto Shinohara, E David Crawford, Anne Simoneau, and Jasjit S Suri. MRI-ultrasound registration for targeted prostate biopsy. In *Proc. IEEE Int. Symp. Biomed. Imaging (ISBI)*, pages 991–994, Boston, MA, USA, 2009.

[NTCO12] Binh P Nguyen, Wei-Liang Tay, Chee-Kong Chui, and Sim-Heng Ong. A clustering-based system to automate transfer function design for medical image visualization. *The Visual Computer*, 28(2):181–191, 2012.

[OT14a] Francisco PM Oliveira and Joao Manuel RS Tavares. Medical image registration: a review. *Computer methods in biomechanics and biomedical engineering*, 17(2):73–93, 2014.

[OT14b] Francisco PM Oliveira and Joao Manuel RS Tavares. Medical image registration: a review. *Computer methods in biomechanics and biomedical engineering*, 17(2):73–93, 2014.

[PAJ16] B Lakshmi Priya, S Joshi Adaikalamarie, and K Jayanthi. Multi-temporal fusion of abdominal CT images for effective liver cancer diagnosis. In *Proc. International Conference on Wireless Communications, Signal Processing and Networking (WiSP-NET)*, pages 1452–1457, Chennai, India, 2016.

[PD92] Michael Powell and James David. Tabulation of thin plate splines on a very fine two-dimensional grid. In *Numerical methods in approximation theory, Vol. 9*, pages 221–244. 1992.

[Pet07] Vladimir Petrović. Subjective tests for image fusion evaluation and objective metric validation. *Information Fusion*, 8(2):208–216, 2007.

[PFF+95] Fabio Parazzini, Monica Ferraroni, Luigi Fedele, Luca Bocciolone, Sabrina Rubessa, and Aldo Riccardi. Pelvic endometriosis: reproductive and menstrual risk factors at different stages in lombardy, northern italy. *Journal of Epidemiology & Community Health*, 49(1):61–64, 1995.

[PHF+14] Bartłomiej W Papież, Mattias P Heinrich, Jérome Fehrenbach, Laurent Risser, and Julia A Schnabel. An implicit sliding-motion preserving regularisation via bilateral filtering for deformable image registration. *Medical image analysis*, 18(8):1299–1311, 2014.

[PHS+96] Uwe Pietrzyk, Karl Herholz, Alexander Schuster, Hans-Martin v Stockhausen, Helmut Lucht, and Wolf-Dieter Heiss. Clinical applications of registration and fusion of multimodality brain images from PET, SPECT, CT, and MRI. *European journal of radiology*, 21(3):174–182, 1996.

[Pip95] James G Pipe. Spatial encoding and reconstruction in mri with quadratic phase profiles. *Magnetic resonance in medicine*, 33(1):24–33, 1995.

[PL06] Jerry Prince and Jonathan Links. *Medical imaging signals and systems.* 2006.

[PM11] Ujwala Patil and Uma Mudengudi. Image fusion using hierarchical pca. In *In International Conference on Image Information Processing*, pages 1–6, Shimla, India, 2011.

[PMV04] Josien Pluim, Antoine Maintz, and Max Viergever. F-information measures in medical image registration. *IEEE Trans. Med. Imag.*, 23(12):1508–1516, 2004.

[PSC$^+$16] Marcelo Pereyra, Philip Schniter, Emilie Chouzenoux, Jean-Christophe Pesquet, Jean-Yves Tourneret, Alfred O Hero, and Steve McLaughlin. A survey of stochastic simulation and optimization methods in signal processing. *IEEE J. Sel. Topics Signal Process.*, 10(2):224–241, 2016.

[PXP00] Dzung Pham, Chenyang Xu, and Jerry Prince. Current methods in medical image segmentation. *Annual review of biomedical engineering*, 2(1):315–337, 2000.

[PZF08] Gheorghe Postelnicu, Lilla Zollei, and Bruce Fischl. Combined volumetric and surface registration. *IEEE Trans. Med. Imag.*, 28(4):508–522, 2008.

[QLD$^+$90] Marc Quirynen, Yves Lamoral, Christel Dekeyser, Patrik Peene, Daniel van Steenberghe, Jan Bonte, and Albert L Baert. The CT scan standard reconstruction technique for reliable jaw bone volume determination. *International Journal of Oral & Maxillofacial Implants*, 5(4), 1990.

[QZY01] Guihong Qu, Dali Zhang, and Pingfan Yan. Medical image fusion by wavelet transform modulus maxima. *Optics Express*, 9(4):184–190, 2001.

[RA10] Daniel Rueckert and Paul Aljabar. Nonrigid registration of medical images: Theory, methods, and applications [applications corner]. *IEEE Signal Processing Magazine*, 27(4):113–119, 2010.

[RCLB$^+$18] Horace Roman, Isabella Chanavaz-Lacheray, Marcos Ballester, Sofiane Bendifallah, Salma Touleimat, Jean-Jacques Tuech, Marilena Farella, and Benjamin Merlot. High postoperative fertility rate following surgical management of colorectal endometriosis. *Human Reproduction*, 33(9):1669–1676, 2018.

[RGN$^+$11] Kashif Rajpoot, Vicente Grau, Alison Noble, Harald Becher, and Cezary Szmigielski. The evaluation of single-view and multi-view fusion 3D echocardiography using image-driven segmentation and tracking. *Medical image analysis*, 15(4):514–528, 2011.

[RKC14] Hassan Rivaz, Zahra Karimaghaloo, and Louis Collins. Self-similarity weighted mutual information: a new nonrigid image registration metric. *Medical image analysis*, 18(2):343–358, 2014.

[RMPA98] Alexis Roche, Grégoire Malandain, Xavier Pennec, and Nicholas Ayache. The correlation ratio as a new similarity measure for multimodal image registration. In *Proc. International Conference on Medical Image Computing and Computer-Assisted Intervention*, pages 1115–1124, Berlin, Heidelberg, 1998.

[Roc97] Oliver Rockinger. Image sequence fusion using a shift-invariant wavelet transform. In *Proc. international conference on image processing*, volume 3, pages 288–291, Santa Barbara, CA, 1997.

[Roh01] Karl Rohr. *Landmark-based image analysis: using geometric and intensity models*, volume 21. Springer Science & Business Media, 2001.

[RP04] Peter Alden Rothschild and Vijendra Guru Raaj Prasad. Medical image management system and method, Jan. 13 2004. US Patent 6,678,703.

[RPMA01] Alexis Roche, Xavier Pennec, Grégoire Malandain, and Nicholas Ayache. Rigid registration of 3D ultrasound with MR images: a new approach combining intensity and gradient information. *IEEE Trans. Med. Imaging*, 20(10):1038–1049, 2001.

[RSH$^+$99] Daniel Rueckert, Luke Sonoda, Carmel Hayes, Derek Hill, Martin Leach, and David

Hawkes. Nonrigid registration using free-form deformations: application to breast MR images. *IEEE Trans. Med. Imag.*, 18(8):712–721, 1999.

[RVW$^+$11] Laurent Risser, François-Xavier Vialard, Robin Wolz, Maria Murgasova, Darryl D Holm, and Daniel Rueckert. Simultaneous multi-scale registration using large deformation diffeomorphic metric mapping. *IEEE Trans. Med. Imag.*, 30(10):1746–1759, 2011.

[Sam09] Navid Samavati. *Deformable multi-modality image registration based on finite element modeling and moving least squares.* PhD thesis, McMaster university, 2009.

[SBHU91] Peter Smith, Oddvar Bakos, Gun Heimer, and Ulf Ulmsten. Transvaginal ultrasound for identifying endometrial abnormality. *Acta obstetricia et gynecologica Scandinavica*, 70(7-8):591–594, 1991.

[SBK$^+$14] Akanksha Sahu, Vikrant Bhateja, Abhinav Krishn, et al. Medical image fusion with Laplacian pyramids. In *Proc. International Conference on Medical Imaging, m-Health and Emerging Communication Systems (MedCom)*, pages 448–453, Greater Noida, 2014.

[Sch05] Orazio Schillaci. Hybrid SPECT/CT: a new era for SPECT imaging?, 2005.

[SCW$^+$15] Feng Shi, Jian Cheng, Li Wang, Pew-Thian Yap, and Dinggang Shen. LRTV: MR image super-resolution with low-rank and total variation regularizations. *IEEE Trans. Med. Imaging*, 34:2459–2466, 2015.

[SdA09] Rodrigo de P Sepulcri and Vivian F do Amaral. Depressive symptoms, anxiety, and quality of life in women with pelvic endometriosis. *European Journal of Obstetrics & Gynecology and Reproductive Biology*, 142(1):53–56, 2009.

[SDP13] Aristeidis Sotiras, Christos Davatzikos, and Nikos Paragios. Deformable medical image registration: A survey. *IEEE Trans. Med. Imag.*, 32(7):1153–1190, 2013.

[SGD04] Muhammad Shoaib Sehgal, Iqbal Gondal, and Laurence Dooley. Support vector machine and generalized regression neural network based classification fusion models for cancer diagnosis. In *Proc. International Conference on Hybrid Intelligent Systems (HIS'04)*, pages 49–54, Kitakyushu, Japan, 2004.

[SKH$^+$03] Harold Szu, Ivica Kopriva, Philip Hoekstra, Nicholas Diakides, Mary Diakides, James Buss, and Jasper Lupo. Early tumor detection by multiple infrared unsupervised neural nets fusion. In *Proc. International Conference of the IEEE Engineering in Medicine and Biology Society (IEEE Cat. No. 03CH37439)*, volume 2, pages 1133–1136, Cancun, Mexico, 2003.

[SKHB18] Martin Sinko, Patrik Kamencay, Robert Hudec, and Miroslav Benco. 3D registration of the point cloud data using ICP algorithm in medical image analysis. In *Proc. Elektro*, pages 1–6, Mikulov, 2018.

[SKS10] James Shackleford, Nagarajan Kandasamy, and GC Sharp. On developing B-spline registration algorithms for multi-core processors. *Physics in Medicine & Biology*, 55(21):6329, 2010.

[SKX$^+$08] Anurag Singh, Jochen Kruecker, Sheng Xu, Neil Glossop, Peter Guion, Karen Ullman, Peter Choyke, and Bradford J Wood. Initial clinical experience with real-time transrectal ultrasonography-magnetic resonance imaging fusion-guided prostate biopsy. *BJU international*, 101(7):841–845, 2008.

[SS10] Romen Singh and Manglem Singh. Image enhancement by adaptive power-law transformations. *Bahria University Journal of Information & Communication Technologies (BUJICT)*, 3(1), 2010.

[Sue17] Paul Suetens. *Fundamentals of medical imaging.* Cambridge university press, 2017.

[Sza04] Thomas L Szabo. *Diagnostic ultrasound imaging: inside out.* Academic Press, 2004.

[TGAH10] Peter Tay, Christopher Garson, Scott Acton, and John Hossack. Ultrasound despeckling for contrast enhancement. *IEEE Transactions on Image Processing*, 19(7):1847–1860, 2010.

[TH80] Roger Tsai and Thomas Huang. Moving image restoration and registration. In *Proc. International Conference on Acoustics, Speech, and Signal Processing*, volume 5, pages 418–421, Colorado, USA, 1980.

[TKO96] Manolis Tsiknakis, Dimitrios Katehakis, and Stelios Orphanoudakis. Intelligent image management in a distributed PACS and telemedicine environment. *IEEE Communications Magazine*, 34(7):36–45, 1996.

[TLPP07] Linda Tessens, Alessandro Ledda, Aleksandra Pizurica, and Wilfried Philips. Extending the depth of field in microscopy through curvelet-based frequency-adaptive image fusion. In *Proc. International Conference on Acoustics, Speech and Signal Processing*, volume 1, pages I–861, Honolulu, HI, 2007.

[Ton02] Giuseppe Tonini. Dysmenorrhea, endometriosis and premenstrual syndrome. *Minerva pediatrica*, 54(6):525, 2002.

[TSP88a] Theresa Tuthill, Robert Sperry, and Karen Parker. Deviations from Rayleigh statistics in ultrasonic speckle. *Ultrasonic imaging*, 10(2):81–89, 1988.

[TSP88b] Theresa Tuthill, Robert Sperry, and Karen Parker. Deviations from Rayleigh statistics in ultrasonic speckle. *Ultrason. imaging*, 10(2):81–89, 1988.

[TWZW10] Jionghua Teng, Suhuan Wang, Jingzhou Zhang, and Xue Wang. Neuro-fuzzy logic based fusion algorithm of medical images. In *Proc. International Congress on Image and Signal Processing*, volume 4, pages 1552–1556, Yantai, China, 2010.

[VdEMPV95] Petra Van den Elsen, Antoine Maintz, E-JD Pol, and Max Viergever. Automatic registration of CT and MR brain images using correlation of geometrical features. *IEEE Trans. Med. Imag.*, 14(2):384–396, 1995.

[VHS+98] Baba Vemuri, Shuangying Huang, Sartaj Sahni, Christiana Leonard, Cecile Mohr, Robin Gilmore, and Jeffrey Fitzsimmons. An efficient motion estimator with application to medical image registration. *Medical Image Analysis*, 2(1):79–98, 1998.

[VMKB19] Fabien Vidal, Oumaima El Mansouri, Denis Kouamé, and Adrian Basarab. On the design of a pelvic phantom for magentic resononance and utltrasound image fusion. In *Proc. International Ultrasonics Symposium (IUS)*, pages 2400–2403, Glasgow, Scotland, 2019.

[VOB+04] Wouter Vogel, Wim Oyen, Jelle Barentsz, Jham Kaanders, and Franz Corstens. PET/CT: panacea, redundancy, or something in between? *Journal of Nuclear Medicine*, 45(1):15S, 2004.

[VOCD01] Denis Vinatier, Géraldine Orazi, Michael Cosson, and Philippe Dufour. Theories of endometriosis. *European Journal of Obstetrics & Gynecology and Reproductive Biology*, 96(1):21–34, 2001.

[VPDG+05] Paolo Vercellini, Giuliana Pietropaolo, Olga De Giorgi, Roberta Pasin, Annalisa Chiodini, and Pier Giorgio Crosignani. Treatment of symptomatic rectovaginal endometriosis with an estrogen–progestogen combination versus low-dose norethindrone acetate. *Fertility and sterility*, 84(5):1375–1387, 2005.

[VPPA07] Tom Vercauteren, Xavier Pennec, Aymeric Perchant, and Nicholas Ayache. Non-parametric diffeomorphic image registration with the demons algorithm. In *Proc. International Conference on Medical Image Computing and Computer-Assisted Intervention*, pages 319–326, Brisbane, Australia, 2007.

[VRTTP12] Eric Van Reeth, Ivan Tham, Cher Heng Tan, and Chueh Loo Poh. Super-resolution in magnetic resonance imaging: a review. *Concepts in Magnetic Resonance Part A*, 40(6):306–325, 2012.

[VS03] Rafael F Valle and John Sciarra. Endometriosis: treatment strategies. *Annals of the New York Academy of Sciences*, 997(1):229–239, 2003.

[VSB+20] Paolo Vercellini, Greta Sergenti, Laura Buggio, Maria Pina Frattaruolo, Dhouha Dridi, and Nicola Berlanda. Advances in the medical management of bowel endometriosis. *Best Practice & Research Clinical Obstetrics & Gynaecology*, 2020.

[vWHB11] Jan Hein van Waesberghe, Marieke Hazewinkel, and Milou Busard. MRI detection of endometriosis. `http://rad.desk.nl/en/p4da490c32edcc/mri-detection-of-endometriosis.html`, 2011.

[VWI97] Paul Viola and William Wells III. Alignment by maximization of mutual information. *International journal of computer vision*, 24(2):137–154, 1997.

[Wag83] Robert Wagner. Statistics of speckle in ultrasound B-scans. *IEEE Trans. Sonics & Ultrason.*, 30(3):156–163, 1983.

[WB08] Alexander Wong and William Bishop. Efficient least squares fusion of MRI and CT images using a phase congruency model. *Pattern Recognition Letters*, 29(3):173–180, 2008.

[WBK+08] Wolfgang Wein, Shelby Brunke, Ali Khamene, Matthew Callstrom, and Nassir Navab. Automatic CT-ultrasound registration for diagnostic imaging and image-guided intervention. *Medical image analysis*, 12(5):577–585, 2008.

[WBSS04] Zhou Wang, Alan Bovik, Hamid Sheikh, and Eero Simoncelli. Image quality assessment: from error visibility to structural similarity. *IEEE Trans. Image Process.*, 13:600–612, 2004.

[WCH+17] Andrew Woerner, Mehee Choi, Matthew Harkenrider, John Roeske, and Murat Surucu. Evaluation of deformable image registration-based contour propagation from planning CT to cone-beam CT. *Technology in cancer research & treatment*, 16(6):801–810, 2017.

[WDLL07] Yang-Ping Wang, Jian-Wu Dang, Qiang Li, and Sha Li. Multimodal medical image fusion using fuzzy radial basis function neural networks. In *Proc. International Conference on Wavelet Analysis and Pattern Recognition*, volume 2, pages 778–782, Beijing, China, 2007.

[WGH$^+$98] Roger Woods, Scott Grafton, Colin Holmes, Simon Cherry, and John Mazziotta. Automated image registration: I. general methods and intrasubject, intramodality validation. *Journal of computer assisted tomography*, 22(1):139–152, 1998.

[WHMA04] Yunfeng Wu, Jingjing He, Yi Man, and Juan Ignacio Arribas. Neural network fusion strategies for identifying breast masses. In *Proc. International Joint Conference on Neural Networks (IEEE Cat. No. 04CH37541)*, volume 3, pages 2437–2442, Budapest, Hungaria, 2004.

[WJLS98] Robert Weinfeld, Sterling Johnson, Ce Lucas, and Faysal Saksouk. CT diagnosis of perihepatic endometriosis complicated by malignant transformation. *Abdominal imaging*, 23(2):183–184, 1998.

[WLT14] Lei Wang, Bin Li, and Lian-Fang Tian. Multi-modal medical image fusion using the inter-scale and intra-scale dependencies between image shift-invariant shearlet coefficients. *Information Fusion*, 19:20–28, 2014.

[WMB$^+$11] Caroline Wright, David M Morris, Philip N Baker, Ian P Crocker, Penny A Gowland, Geoff J Parker, and Colin P Sibley. Magnetic resonance imaging relaxation time measurements of the placenta at 1.5 T. *Placenta*, 32(12):1010–1015, 2011.

[WMG10] Zhaobin Wang, Yide Ma, and Jason Gu. Multi-focus image fusion using pcnn. *Pattern Recognition*, 43(6):2003–2016, 2010.

[WR13] Marijke Welvaert and Yves Rosseel. On the definition of signal-to-noise ratio and contrast-to-noise ratio for fMRI data. *PloS one*, 8(11):e77089, 2013.

[WRN$^+$99] Jürgen Weese, Peter Rösch, Thomas Netsch, Thomas Blaffert, and Marcel Quist. Gray-value based registration of CT and MR images by maximization of local correlation. In *Proc. International Conference on Medical Image Computing and Computer-Assisted Intervention*, pages 656–663, 1999.

[WS98] Yongmei Wang and Lawrence H Staib. Elastic model based non-rigid registration incorporating statistical shape information. In *Proc. International Conference on Medical Image Computing and Computer-Assisted Intervention*, pages 1162–1173, 1998.

[WWN$^+$06] Yunfeng Wu, Cong Wang, Sin Chun Ng, Anant Madabhushi, and Yixin Zhong. Breast cancer diagnosis using neural-based linear fusion strategies. In *Proc. International Conference on Neural Information Processing*, pages 165–175, Berlin, Heidelberg, 2006.

[WWZM16] Zhaobin Wang, Shuai Wang, Ying Zhu, and Yide Ma. Review of image fusion based on pulse-coupled neural network. *Archives of Computational Methods in Engineering*, 23(4):659–671, 2016.

[WX09] Hao-quan Wang and Hao Xing. Multi-mode medical image fusion algorithm based on principal component analysis. In *2009 International Symposium on Computer Network and Multimedia Technology*, pages 1–4, Wuhan, China, 2009.

[XCT$^+$08] Rui Xu, Yen-Wei Chen, Song-Yuan Tang, Shigehiro Morikawa, and Yoshimasa Kurumi. Parzen-window based normalized mutual information for medical image registration. *IEICE transactions on information and systems*, 91(1):132–144, 2008.

[XWCY15] Lele Xu, Xia Wu, Kewei Chen, and Li Yao. Multi-modality sparse representation-based classification for alzheimer's disease and mild cognitive impairment. *Computer methods and programs in biomedicine*, 122(2):182–190, 2015.

[Yin15] Haitao Yin. Sparse representation with learned multiscale dictionary for image fusion. *Neurocomputing*, 148:600–610, 2015.

[YLCJ15] Jiaolong Yang, Hongdong Li, Dylan Campbell, and Yunde Jia. Go-ICP: A globally optimal solution to 3D ICP point-set registration. *IEEE transactions on pattern analysis and machine intelligence*, 38(11):2241–2254, 2015.

[YLF13] Haitao Yin, Shutao Li, and Leyuan Fang. Simultaneous image fusion and super-resolution using sparse representation. *Information Fusion*, 14(3):229–240, 2013.

[YSB$^+$13] Amir Yavariabdi, Chafik Samir, Adrien Bartoli, David Da Ines, and Nicolas Bourdel. Contour-based TVUS-MR image registration for mapping small endometrial implants. In *Proc. International MICCAI Workshop on Computational and Clinical Challenges in Abdominal Imaging*, pages 145–154, 2013.

[YSS10] Yi Yang, Zhengwei Su, and L Sun. Medical image enhancement algorithm based on wavelet transform. *Electronics letters*, 46(2):120–121, 2010.

[YWA10] Qingxiong Yang, Liang Wang, and Narendra Ahuja. A constant-space belief propagation algorithm for stereo matching. In *Proc. Computer Society Conference on Computer Vision and Pattern Recognition*, pages 1458–1465, San Francisco, CA, 2010.

[ZDFZB03] Raffaella Zanardi, Chiara Del Frate, Chiara Zuiani, and Massimo Bazzocchi. Staging of pelvic endometriosis based on MRI findings versus laparoscopic classification according to the American Fertility Society. *Abdominal imaging*, 28(5):733–742, 2003.

[ZF03] Barbara Zitova and Jan Flusser. Image registration methods: a survey. *Image and vision computing*, 21(11):977–1000, 2003.

[ZFLZ13] Qiheng Zhang, Yuli Fu, Haifeng Li, and Jian Zou. Dictionary learning method for joint sparse representation-based image fusion. *Optical Engineering*, 52(5):057006, 2013.

[ZG09] Qiang Zhang and Bao-long Guo. Multifocus image fusion using the nonsubsampled contourlet transform. *Signal processing*, 89(7):1334–1346, 2009.

[Zha16] Ningning Zhao. *Inverse problems in medical ultrasound images-applications to image deconvolution, segmentation and super-resolution.* PhD thesis, University of Toulouse, France, 2016.

[ZQ17] Jing-jing Zong and Tian-shuang Qiu. Medical image fusion based on sparse representation of classified image patches. *Biomedical Signal Processing and Control*, 34:195–205, 2017.

[ZTL$^+$04] Qing-Ping Zhang, Wei-Jen Tang, Loi Lei Lai, Wai Ching Sun, and Kit Po Wong. Medical diagnostic image data fusion based on wavelet transformation and self-organising features mapping neural networks. In *Proc. International Conference on Machine Learning and Cybernetics*, volume 5, pages 2708–2712, Shanghai, China, 2004.

[ZWB$^+$16a] Ningning Zhao, Qi Wei, Adrian Basarab, Nicolas Dobigeon, Denis Kouamé, and Jean-Yves Tourneret. Fast single image super-resolution using a new analytical solution for $\ell_2 - \ell_2$ problems. *IEEE Trans. Med. Imag.*, 25(8):3683–3697, 2016.

[ZWB$^+$16b] Ningning Zhao, Qi Wei, Adrian Basarab, Nicolas Dobigeon, Denis Kouamé, and Jean-Yves Tourneret. Fast single image super-resolution using a new analytical solution for l_2-l_2 problems. *IEEE Trans. Image Process.*, 25:3683–3697, 2016.

[ZYKK07] Fan Zhang, Yang Mo Yoo, Liang Mong Koh, and Yongmin Kim. Nonlinear diffusion in Laplacian pyramid domain for ultrasonic speckle reduction. *IEEE trans. med. imag.*, 26(2):200–211, 2007.

[ZYL12] Fei Zhou, Wenming Yang, and Qingmin Liao. Interpolation-based image super-resolution using multisurface fitting. *IEEE Transactions on Image Processing*, 21(7):3312–3318, 2012.

[ZZMZ11] Lin Zhang, Lei Zhang, Xuanqin Mou, and David Zhang. FSIM: A feature similarity index for image quality assessment. *IEEE trans. Imag. Processing*, 20(8):2378–2386, 2011.
